SYNTHESIS OF GRAPHENE BASED MATERIALS AND THEIR APPLICATIONS AS ENERGY STORAGE MATERIALS AND NI (II) IONS ADSORBANT

JIABIN WANG

Dissertation submitted in fulfilment
of the requirements for the degree of
Doctor of Philosophy

School of Chemical Engineering and Advanced Materials
Faculty of Science, Agriculture and Engineering
Newcastle University

Apirl 2017

Abstract

Today, with the increasing global concern regarding energy savings, CO_2 emission and environmental protection, the development of low cost and environmentally friendly materials for electrodes in energy storage devices and adsorbent in wastewater treatment becomes important. Graphene, as a new materials, has attracted lots of attention due to its high current carrying capacity and high surface area. These properties give graphene the huge potential to be used as electrode materials for energy storage devices and adsorbant materials for heavy metal ions. However, the complicate synthesis methods and long reaction time limit its industrial scale up application. In this thesis, the research is focused on development of graphene based composite materials produced by fast, green and energy saving synthesis methods and study their usage as electrodes and for Ni (II) ions removal by analysing the electrochemical properties and Ni (II) ions absorb capacity.

Beside graphene, bismuth has also been considered as safe and non-toxic material. In addition, a large amount of bismuth is produced as a by-product of the copper and tin refining industry. The long Fermi wavelength and high Hall coefficient give bismuth the possibility to reach high electronic conductivity with controlled structure. Therefore, bismuth compounds were selected to decorate graphene for the electrode materials. In this study, reduced graphene oxide bismuth composite (rGO/Bi, Bi_2O_3-GO, rGO/$Bi_2O_2CO_3$) were synthesis at 60°C or room temperature with short reaction time of 3 hrs. These composite materials exhibit nano-structure and good electrochemical properties, such as high specific capacity and long cycling life. In the rGO/Bi composite materials, bismuth particles with size around 20 to 50 nm were wrapped and protected by graphene layers from oxidation. This composite materials achieves a specific capacity value of 773 C g^{-1}, which is in the range of its theoretical value. In the Bi_2O_3-GO composite material, Bi_2O_3 shows a flower-like shape and linked by graphene oxide layer. This material reaches a specific capacity value as high as 559 C g^{-1}. In the rGO/$Bi_2O_2CO_3$ composite materials, nanosized bismuth subcarbonate were attached on the graphene layers. This composite material shows stable cycling performance even af-

ter 4500 cycles. With the low cost of initial materials, simple synthesis methods, low reaction temperature, short reaction time, high specific capacity value and stable long cycling life, graphene bismuth compounds could be the promising candidates for the future electrodes used in electrochemical energy storage devices.

The ability of Ni (II) ions removal by graphene oxide (GO) with sodium dodecyl sulphate (SDS) was also studied. Previous studies have proved that Ni is an excellent catalyst for carbon dioxide reforming. A robust Ni (II) ions removal absorbant is needed in order for this technology to become widely acceptable. SDS has been widely used as the industrial surfactant in toothpaste and shampoo. By adding SDS to decorate GO, it helps prevent graphene oxide sheets from stacking back together and then further enlarge the GO's capacity of Ni (II) ions removal. In this work, SDS was added to modify graphene oxide surface by a one-step easy-to-handle method at room temperature. The effect of time on adsorption, initial concentration of Ni (II) ions and pH value of the Ni (II) ion solutions with GO and GO-SDS were analyzed. The driving force of the adsorption of Ni (II) ions on GO-SDS is proved to be by electrostatic attraction, Ni (II) ions are adsorbed on the GO surface chemically and by ion exchange. By using SDS modified GO, the Ni (II) ions adsorption capacity was increased dramatically from 20.19 mg g^{-1} to 55.16 mg g^{-1} in respect to pure GO.

Acknowledgements

I would like to express my sincere gratitude to my supervisor, Dr. Lidija Šiller for the continuous support during my PhD study. Her patience, motivation, enthusiasm, encouragement and guidance help me overcome many difficulties in my research study.

I own my deep gratitude to Dr. Jie Tang for offer me a collaboration work opportunity with her group in the National Institute for Materials Science, Tsukuba, Japan, where I have spent 4 months.

I would like to thank the School of Chemical Engineering and Advanced Materials, Newcastle University, UK for the award of a scholarship and the National Institute for Materials Science, Tsukuba, Japan for financial support.

I also want to show my gratitude to Dr. Han Zhang, Dr. Alasdair Charles, Dr. Elif C. Salihi, Dr. Michael R. C. Hunt, Dr. Oana Bretcanu, Dr. David Walker, Dr. Gaurav A. Bhaduri, Khalil T. Hasan and Yige Sun for their help and support of sample characterization, data analysis and critical reading.

Abbreviation

BET	Brunauer-Emmett-Teller
CE	Counter electrode
CHA	Concentric hemispherical analyser
CV	Cyclic voltammetry
DTA	Differential thermal analysis
EDLC	Electrochemical double layer capacitor
EDS	Energy dispersive X-ray spectroscopy
ELS	Electrophoretic light scattering
FTIR	Fourier transform infrared spectrometer
GO	Graphene oxide
HRTEM	High resolution transmission electron microscopy
IHP	Inner Helmholz plane
OHP	Outer Helmholz plane
RE	Reference electrode
rGO	Reduced graphene oxide
SAED	Selected area electron diffraction
SCE	Saturated calomel electrode
SEM	Scanning electron microscope
SHE	Standard hydrogen electrode
TEM	Transmission electron microscopy
TGA	Thermos-gravimetric analysis
WE	Working electrode
XPS	X-ray photoemission spectroscopy
XRD	X-ray diffraction

Contents

1 Introduction **1**

1.1 Energy storage devices 1

1.1.1 Electrochemical devices 2

1.1.2 Electrochemical supercapacitors 3

1.2 Wastewater treatment 5

1.2.1 Ni ions pollution 5

2 Literature Review **12**

2.1 Review of graphene 13

2.1.1 Structure of graphene 13

2.1.2 Methods of synthesis of graphene 13

2.1.3 Electrochemical properties of graphene 15

2.1.4 Adsorption abilities of heavy metal ions by graphene oxide 16

2.2 Review of bismuth and bismuth compounds 17

2.2.1 Structure of bismuth and bismuth compounds 17

2.2.2 Synthesis method of bismuth and bismuth compounds 18

2.2.3 Electrochemical properties of bismuth and bismuth compounds 20

2.3 Summary 21

3 Analytical instruments **30**

3.1 X-ray diffraction 30

3.1.1 Instrument 31

3.1.2 Data interpretation 32

3.1.3 XRD characterization of rGO and bismuth 33

3.2 Scanning electron microscope 34

3.2.1 Instrument 34

3.2.2 Principles of the operation . . . 35
3.3 Transmission electron microscope . . . 35
3.3.1 Instrument . . . 36
3.3.2 Imaging in TEM . . . 37
3.3.3 Analytical possibilities in TEM . . . 38
3.3.4 SEM and TEM characterization of rGO . . . 39
3.4 X-ray photoemission spectroscopy (XPS) . . . 40
3.4.1 Measurement principles . . . 40
3.4.2 Instrument . . . 41
3.5 Fourier transform infrared (FTIR) spectroscopy . . . 42
3.5.1 Measurement principles . . . 42
3.5.2 Instrument . . . 43
3.5.3 XPS spectra of rGO and bismuth . . . 44
3.6 Raman spectroscopy . . . 45
3.6.1 Raman Scattering . . . 45
3.6.2 Instrument . . . 46
3.6.3 Raman spectra of GO and rGO . . . 46
3.7 Electrochemical analyser . . . 47
3.7.1 Instrumentation . . . 48
3.7.2 Electrochemical cells . . . 48
3.7.3 Technique used in electrochemical test . . . 51
3.8 Electrophoretic light scattering (ELS) . . . 53
3.8.1 Zeta potential . . . 53
3.8.2 Measurement principles . . . 54
3.8.3 Instrument . . . 55
3.8.4 Zeta potential of graphene oxide . . . 55

4 Synthesis and characterisation of reduced graphene oxide/bismuth composite for electrodes in electrochemical energy storage devices 61

4.1 Introduction . . . 61
4.2 Experimental . . . 63
4.2.1 Chemicals . . . 63
4.2.2 Materials synthesis . . . 64
4.2.3 Sample characterization . . . 64

4.3 Results and discussion . . . 65
4.3.1 XRD restuls of rGO/Bi . . . 65
4.3.2 FTIR and Raman spectroscopy of GO and rGO/Bi . . . 66
4.3.3 SEM and TEM images of rGO/Bi . . . 68
4.3.4 BET of rGO/Bi and rGO . . . 70
4.3.5 XPS of rGO/Bi . . . 71
4.3.6 DTA and TGA of rGO/Bi and rGO . . . 73
4.3.7 Electrochemical properties of rGO/Bi and rGO . . . 74
4.4 Conclusion . . . 78

5 Low cost synthesis of Bi_2O_3-GO composite as electrodes used in electrochemical energy storage 86
5.1 Introduction . . . 86
5.2 Experimental . . . 87
5.2.1 Chemicals . . . 87
5.2.2 Materials synthesis . . . 88
5.2.3 Sample characterization . . . 88
5.3 Results and discussion . . . 89
5.3.1 XRD of Bi_2O_3-GO and GO . . . 89
5.3.2 Raman and FTIR of GO and Bi_2O_3-GO . . . 90
5.3.3 XPS study of GO and Bi_2O_3-GO . . . 91
5.3.4 SEM images of Bi_2O_3-GO . . . 93
5.3.5 TEM images of Bi_2O_3-GO . . . 93
5.3.6 Electrochemical behaviour of Bi_2O_3-GO composite . . . 94
5.4 Conclusion . . . 97

6 Nanosized $Bi_2O_2CO_3$ particles decorated on graphene for electrode used in the energy storage devices 102
6.1 Introduction . . . 102
6.2 Experimental . . . 103
6.2.1 Chemicals . . . 103
6.2.2 Material synthesis . . . 103
6.2.3 Sample characterization . . . 103
6.3 Results and discussion . . . 104

6.3.1 XRD of rGO/$Bi_2O_2CO_3$ composite material 104
6.3.2 FTIR and Raman spectroscopy of GO and rGO/$Bi_2O_2CO_3$ 105
6.3.3 SEM images of rGO/$Bi_2O_2CO_3$ 106
6.3.4 TEM images of rGO/$Bi_2O_2CO_3$ 107
6.3.5 Electrochemical properties of rGO/$Bi_2O_2CO_3$ composite 108
6.4 Conclusion 111

7 Enhanced removal of Nickel (II) ions from aqueous solutions by SDS-functionalized graphene oxide 116
7.1 Introduction 116
7.2 Experimental 118
7.3 Results and discussion 119
7.3.1 Adsorption kinetics 119
7.3.2 Equilibrium isotherm models 122
7.3.3 Study the effect of pH on Ni(II) ions removal 124
7.3.4 Study of the mechanism of Ni (II) ions adsorption 124
7.3.5 Morphology of the GO and GO-SDS 126
7.3.6 Comparison of Ni adsorption 128
7.4 Conclusion 130

8 Conclusion and future work 137
8.1 Conclusion 137
8.2 Future work 139

List of Figures

2.1 Hexagonal honeycomb lattice of graphene 14
2.2 Lerf-Klinowski model of grapehen oxide 14
2.3 Bulk structure of Bi (rhombohedral unit cell) 17
2.4 Bismuth prepared by electrodeposition, solvothermal and thermal plasma . . . 18
2.5 Images of rippled bismuth oxide 19
2.6 SEM images of flower-like structure bismuth subcarbonate 20
2.7 TEM images of flower-like structure bismuth subcarbonate 20
3.1 Ni ions adsorption by GO and GO-SDS fitted to the pseudo-second order model 31
3.2 A typical diffractometer 32
3.3 Schematic diagram of SEM 35
3.4 Transmission electron microscope 36
3.5 Imaging and diffraction in the TEM (schematic diagram) 37
3.6 Diffraction pattern in TEM 39
3.7 SEM and TEM images of GO and rGO 40
3.8 A XPS process with photoionization of an atom by the ejection of a 1s electron 41
3.9 A concentric hemispherical analyser used in XPS 42
3.10 An optical diagram of a Michelson interferometer 43
3.11 Schematic illustration of Rayleigh scattering and Stokes and anti-Stokes Raman scattering 45
3.12 A basic schematic of the Raman spectroscopic system 46
3.13 Raman spectra of carbon materials 47
3.14 Schematic diagram of a three electrode potentiostat 48
3.15 Electrochemical cell of a three electrodes system 49
3.16 Typical cyclic voltammogram of graphene and graphene/bismuth oxide composite materials 52
3.17 Typical charge/discharge curves of a graphene/bismuth oxide composite material 53

3.18 Schematic of the charges and potentials at a positively charged interface 54
3.19 Schematic arrangement of the Malvern Zetasizer 55
3.20 Zeta potential of graphene oxide 56
4.1 X-ray powder diffractogram of rGO/Bi 66
4.2 FTIR spectra and Raman spectra of GO, rGO/Bi and rGO 67
4.3 SEM images of the as prepared rGO/Bi composite 68
4.4 TEM images of the as prepared rGO/Bi composite 69
4.5 Nitrogen adsorption-desorption isotherms of rGO/Bi rGO 70
4.6 XP survey spectrum obtained from 27 month-old rGO/Bi composite 71
4.7 XP survey spectrum obtained from 27 month-old rGO/Bi composite of Bi and C 71
4.8 DTA and TGA curves of rGO/Bi and rGO 73
4.9 Typical CV results of rGO/Bi, rGO and Ni foam 74
4.10 Typical charge/discharge behaviours of rGO/Bi and rGO 76
4.11 Specific capacity of rGO/Bi and rGO calculated from charge/discharge curves . 77
4.12 Life-cycle test of rGO/Bi composite under 5 A g^{-1} current density 78
5.1 X-ray powder diffractogram of flower-like Bi_2O_3-GO and graphene oxide . . . 89
5.2 Raman spectroscopy and FTIR of Bi_2O_3-GO 91
5.3 C1s XPS spectra of GO and Bi_2O_3-GO 92
5.4 SEM figures of flower-like Bi_2O_3-GO 93
5.5 TEM image of Bi_2O_3-GO 93
5.6 Cyclic voltammetry results of Bi_2O_3-GO composite 94
5.7 Charge/discharge behaviour of Bi_2O_3-GO composite 95
5.8 The calculated specific capacity of Bi_2O_3-GO for different current densities . . 96
5.9 Cycling performances of Bi_2O_3-GO composite 97
6.1 X-ray powder diffractogram of rGO/$Bi_2O_2CO_3$ 104
6.2 FTIR and Raman spectroscopy of GO and rGO/$Bi_2O_2CO_3$ 105
6.3 SEM images of rGO/$Bi_2O_2CO_3$ 106
6.4 EDS spectra of rGO/$Bi_2O_2CO_3$ composite material 107
6.5 TEM images of rGO/$Bi_2O_2CO_3$ 107
6.6 HRTEM images of rGO/$Bi_2O_2CO_3$ 108
6.7 Cyclic voltammogram of rGO/$Bi_2O_2CO_3$ composite as electrode with different scanning rates 108
6.8 The charge/discharge behaviour of rGO/$Bi_2O_2CO_3$ composite under various current density 110

6.9 Specific capacity of rGO/$Bi_2O_2CO_3$ changes with current density increase . . . 111
6.10 The cycling performance of rGO/$Bi_2O_2CO_3$ 111
7.1 Effect of contact time of Ni (II) ions on GO and GO-SDS 119
7.2 Ni ions adsorption by GO and GO-SDS fitted to the pseudo-second order model 120
7.3 Intraparticle diffusion plots of GO and GO-SDS at different times 121
7.4 Giles isotherms of the adsorption of Ni (II) ions on GO and GO-SDS 122
7.5 The Langmuir model fitted of Ni (II) ions adsorption on GO and GO-SDS . . . 123
7.6 The adsorption capacities of GO and GO-SDS on Ni(II) ions changes with pH value of the solution 124
7.7 Zeta potential of GO and GO-SDS changes at different pH value 125
7.8 FTIR of GO and GO-SDS before and after Ni absorption 126
7.9 SEM images of GO and GO-SDS before and after Ni adsorption 127
7.10 TEM images of GO 128
7.11 Comparison of % Ni (II) ions removal with different amounts of GO and GO-SDS 129

List of Tables

3.1 Interplanar spacing 32

7.1 Kinetic parameters of the Ni (II) ions adsorption on GO and GO-SDS 122

7.2 Adsorption isotherm parameters for the adsorption of Ni (II) ions on GO and GO-SDS 123

7.3 Comparison of various adsorbents for the removal of Ni (II) ions 129

8.1 Summaries of graphene bismuth composite materials 138

Chapter 1

Introduction

Today, with the world population growing and the portable electronic devices getting popular, the energy consumption keeps growing steadily [1]. The worldwide energy consumption in 2008 was estimated to be 144, 000 TWh [1]. The energy supplies are mainly from fossil fuel and nuclear and also from renewable sources, such as solar, hydroelectric wind and geothermal [1]. The aim of this project is to synthesis a graphene based composite to reduce the impact on environment and reduce CO_2 emission. The development of efficient energy storage devices is essential to balance the supply and the demand of energy and reduce the CO_2 emission. In addition, Nickel has been proved as an excellent catalyst for CO_2 reforming and catalyst for hydration reaction of CO_2 [2, 3]. However, the toxic effects of Ni (II) ions on both the environmental and human health are of serious concern [4]. An effective Ni(II) ions absorbant is needed in order for this technology to become widely acceptable. In this chapter, the mechanism of currently used energy storage devices and the widely used methods of wastewater treatment were summarised and discussed.

1.1 Energy storage devices

Energy in different forms can be stored by different methods, such as hydroelectricity, pumped storage, compressed air, flywheel energy storage and electrochemical devices. Hydroelectricity captures energy from failing water, in which the kinetic energy is transformed into mechanical energy and then is converted into electrical energy. Pumped storage devices store electrical energy by moving water between an upper and a lower reservoir [5]. The rotational energy stored in flywheel is obtained by accelerating the rotor of flywheel to a high speed. Energy can

be extracted by reducing the rotational speed. Compressed air energy storage is a technology that stores energy as compressed air and supplies energy at a gas turbine [1]. Electrochemical devices generate electrical energy from chemical reactions or electrostatic forces. Among these different energy storage and conversion technologies, electrochemical one, such as batteries, fuel cells and electrochemical supercapacitors, have been considered as the sustainable and efficient devices [6].

1.1.1 Electrochemical devices

The electrochemical energy storage devices can be divided into batteries and electrochemical capacitors based on their energy storage mechanisms [7]. Lithium ions batteries are the devices that convert chemical energy into electrical energy and vice versa [8]. It contains an anode, a cathode and an electrolyte [8]. Graphite is commonly used as the commercial anode material [9]. Even graphite has low cost and good cycle life, lots of research have been done to investigate the substitute materials. This is because graphite only allows intercalation of one lithium ion within its six carbon atoms [10]. The electrochemical properties of some other materials, such as Mn_3O_4 [11], were also studied to further increase the capacity of anode electrode. Transition metal oxides or phosphates active materials, such as $LiCoO_2$ [12,13], $LiMn_2O_4$ [14, 15], $LiFePO_4$ [16, 17], are used as the cathode materials. Anode and cathode are separated by a membrane filled with electrolyte contains lithium salts in alkyl organic carbonates solution [9]. This separator prevents the contact between electrodes and allows the lithium ions to diffuse between them [9]. During the discharge process, lithium ions flow from the anode to the cathode allowing the conversion from chemical energy to electrical energy [9]. The reaction happens in anode and cathode can be expressed as following equations 1.1 and 1.2 (use graphite and $LiCoO_2$ as example for electrode materials) [9]:

$$C + xLi + xe^{-} \leftrightarrow Li_xC_6 \tag{1.1}$$

$$LiCoO_2 \leftrightarrow Li_{(1-x)}CoO_2 + xLi + xe^{-} \tag{1.2}$$

Lithium ions batteries are widely used as the energy storage devices for cellular phones, laptops and digital electronics [9]. However, the energy density required to employ lithium ions batteries in electric vehicles are two to five times more than the present technology can offer [9, 18].

Electrochemical supercapacitor is an energy storage device which has similar design as the traditional capacitors. It contains two electrodes, an electrolyte and a separator that electrically isolates the two electrodes [19]. Compared to the conventional capacitors, electrochemical supercapacitors have higher energy densities [6]. For the electrochemical supercapacitors, the electrodes are generally made by materials with high surface area and high porosity, such as active carbon and metal oxide nanoparticles [19].

1.1.2 Electrochemical supercapacitors

The electrochemical supercapacitors can be classified into two types, electrochemical double layer capacitors (EDLC) and pseudocapacitors, based on their charge storage mechanism.

Electrochemical double layer capacitors (EDLC)

In EDLC, the charge are stored by a non-faradaic method, which means the capacitance is obtained by the accumulation of electrostatic charge at the interface of electrode and electrolyte [19]. The charges generated at the electrode surface are contributed by both the surface dissociation and the ion adsorption from electrolyte and crystal lattice defects [19, 20]. The electrodes used in EDLC are generally made by high surface area carbon based materials [21]. In this type of supercapacitor, energy is stored in the electrode/electrolyte interfaces (double layer). There has no ion exchanges occurred between the electrode and electrolyte [19]. In addition, the good wettability and electrical conductivity of electrolyte help reduce the internal resistance of the electrodes and increase the mobility of ions into the pores of electrodes to further increase the capacitance [22].

Activated carbons, which are generally produced by physically or chemically activation of carbonaceous materials, such as wood [23, 24], coal [25, 26] and hemp [27], at high temperature from 400°C to 900°C [25–27], have been widely used as the electrode materials for EDLC [22]. This is because activated carbons have large surface area (from 500 $m^2\ g^{-1}$ to 2400 $m^2\ g^{-1}$ [28, 29]) and high pore volume (from 0.26 $cm^3\ g^{-1}$ to 1.16 $cm^3\ g^{-1}$ [28]). However, even with the high surface area and broad pore size distribution, activated carbon shave only achieved a specific capacitance value of 160 $F\ g^{-1}$ [22], which indicates that not all pores are effective in the charge accumulation [30]. Therefore, beside the surface area, pore structure, electrical conductivity and surface functional groups may also affect the electrochemical properties of the electrode materials [19]. To further improve the capacitance value, other carbon structures, such as ordered mesoporous carbon [31–33], carbon nanotubes [34–36] and

graphene [37, 38], have been studied their potential applications as electrode materials [6].

Pseudocapacitors

When a voltage applied to pseudocapacitors, fast and reversible Faradaic reactions take place on the electrode materials [19]. This procedure involves the passage of charge across the double layers which leads to the Faradaic current passing through the supercapacitor cells [19]. Unlike the chemical reactions happen in the electrode of rechargeable batteries, the reactions take place in pseudocapacitors are fast and reversible between the electrolyte and the electroactive materials on the electrode surface [22]. Therefore, metal oxides, which have more than one oxidation state, have been considered their applications as electrodes in pseudocapacitors [22].

The electrochemical properties of both amorphous [39, 40] and crystalline [41] forms ruthenium oxide (RuO_2) have been widely studied in the past few decades due to their intrinsic reversibility and good conductivity [22, 41, 42]. In addition, the theoretical value of the specific capacitance of RuO_2 has been estimated in the range from 1300 F g^{-1} to 2200 F g^{-1} [41, 43].

The reaction takes place in the RuO_2 electrode has been considered as following [41]

$$RuO_a(OH)_b + \delta H^+ + \delta e^- \leftrightarrow RuO_{(a-\delta)}(OH)_{(b+\delta)} \tag{1.3}$$

This redox reaction involves the proton and electron double injection/expulsion of the oxyruthenium groups [22, 41]. The Faradaic charge is stored and delivered through the redox reactions between oxyruthenium groups of different oxidation states (Ru(IV)/Ru(III) and Ru(III)/Ru(II)) [22]. RuO_2 can be synthesized through variety methods, such as chemical deposition, sol-gel synthesis [44, 45], and electrochemical deposition [41]. The synthesized RuO_2 exhibits great electrochemical properties with a specific capacitance value as high as 1300 F g^{-1} [41]. The rare metal nature and the high cost of ruthenium limit its scale up applications. Therefore, researchers have also studied the electrochemical properties of other metal oxides, such as NiO [46–48] and MnO_2 [49, 50], and sought the appropriate materials for electrodes used in future electrode devices.

In general, the advantages of electrochemical supercapacitors, such as fast charging time, stable cycle performance and broad application temperature ranges, give them the potential to be used in electric vehicles, electronics devices and aircrafts [6]. However the relatively low energy density and high manufacture price limit the scale up production of electrochemical supercapacitors [6].

1.2 Wastewater treatment

Heavy metal ions pollution is one of the serious worldwide environmental problems due to their toxic and bio-accumulative nature [51]. To solve this problem, a wide range of technologies, such as chemical precipitation [52], ion exchange [53], membrane technology [54], electrochemical treatment [55] and adsorption [56], have been developed to remove heavy metal ions from the waste water [51].

Chemical precipitation used in wastewater treatment, such as hydroxide precipitation, sulphide precipitation, cyanide precipitation and carbonate precipitation, involves the change of form of materials from dissolved in water into solid particles [57]. The ionic constituents will be continuously removed from the water by adding counter-ions to reduce the solubility [57]. Chemical precipitation is always followed by a solid separation or filtration procedure to remove the precipitates [57]. By using ion exchange method, the undesirable ions are replaced by similar charged ions which could not contaminate the environment [53]. Membrane technology is a physical process to remove particles, colloids and macromolecules in the waste water [54]. By using membrane with porous size smaller than 5 nm, small molecules and ions can be removed [54]. In electrochemical water treatment, metal ions formed a cathodic deposition due to the electric current applied [55]. Adsorption is a surface process, in which molecules or ions are removed from the aqueous solution by adsorption onto solid surface [58].

Among all these physical and chemical methods, adsorption is believed to be the promising one. This is due to its flexibility in operation, feasibility of producing high quality product, low initial cost and the possibility to treat pollutants at a low concentration [51]. Because adsorption is a surface based process, the ideal absorbent should have high surface area with chemically functionalised pores and good adsorption capacity.

1.2.1 Ni ions pollution

Nickel is the 24^{th} most abundant element in the Earth's crust and has a wide range of both industrial and commercial applications, including electroplating, battery manufacture, forging, metal finishing and mining. All these leads to Ni ions water pollution [56]. Nickel is also known as a human carcinogen element [59]. Expose to high nickel contained environment may cause serious lung and kidney problems, gastrointestinal distress, pulmonary fibrosis and skin dermatitis [56, 59, 60].

Recently, the catalytic activity of Ni in the form of Ni nanoparticles (NiNPs) for the reversible hydration of carbon dioxide at room temperature and atmospheric pressure has been reported [3]. NiNPs has been proved has the capability to accelerate the mineral carbonation processes [3]. In order to get this technology widely accepted, a robust Ni adsorber is required as the precaution against environmental accidents [56]. Therefore, a safe adsorber material synthesized through a simple method for Ni ions removal is urgently needed.

References

[1] N. Kularatna, *Energy storage devices for electronic systems, Rechargeable batteries and supercapacitors*. London: Elsevier, 2015.

[2] X. Han, F. Williamson, G. A. Bhaduri, A. Harvery, and L. Siller, "Synthesis and characterisation of ambient pressure dried composites of silica aerogel matrix and embedded nickel nanoparticles," *The Journal of Supercritical Fluids*, vol. 106, pp. 140–144, 2015.

[3] G. A. Bhaduri and L. Šiller, "Nickel nanoparticles catalyse reversible hydration of carbon dioxide for mineralization carbon capture and storage," *Catalysis Science & Technology*, vol. 3, pp. 1234–1239, 2013.

[4] M. Zhao, Y. Xu, C. Zhang, H. Rong, and G. Zeng, "New trends in removing heavy metals from wastewater," *Applied Microbiology Biotechnology*, vol. 100, pp. 6509–6518, 2016.

[5] G. Vojvodic, A. I. Jarrah, and D. P. Morton, "Forward thresholds for operation of pumped-storage stations in the real-time energy market," *European Journal of Operational Research*, vol. 254, pp. 253–268, 2016.

[6] A. Y. B. Kim, S. Sy and J. Zhang, *Handbook of clean energy systems, Electrochemical supercapacitors for energy storage and conversion*. John Wiley & Sons, 2015.

[7] B. E. Conway, *Electrochemical supercapacitors: Scientific fundamentals and technological applications*. New York: Kluwer Academic/Plenum Publisher, 1999.

[8] M. S. Whittingham, "Lithium batteries and cathode materials," *Chemical Reviews*, vol. 104, pp. 4271–4301, 2004.

[9] S. Goriparti, E. Miele, F. De Angelis, E. Di Fabrizio, R. Proietti Zaccaria, and C. Capiglia, "Review on recent progress of nanostructured anode materials for Li-ion bat-

teries," *Journal of Power Sources*, vol. 257, pp. 421–443, 2014.

[10] Z. Xiong, Y. S. Yun, and H-J. Jin, "Applications of carbon nanotubes for lithium ion battery anodes," *Materials*, vol. 6, pp. 1138–1158, 2013.

[11] M. Zhen, Z. Zhang, Q. Ren, and L. Liu, "Room-temperature synthesis of ultrathin Mn_3O_4 nanosheets as anode materials for lithium-ion batteries," *Materials Letters*, vol. 177, pp. 21–24, 2016.

[12] R. Tang, Q. Yun, W. Lv, Y. He, C. You, F. Su, L. Ke, B. Li, F. Kang, and Q. Yang, "How a very trace amount of graphene additive works for constructing an efficient conductive network in $LiCoO_2$-based lithium-ion batteries," *Carbon*, vol. 103, pp. 356–362, 2016.

[13] L. Zhang, X. Cheng, Y. Ma, T. Guan, S. Sun, Y. Cui, C. Du, P. Zuo, Y. Gao, and G. Yin, "Effect of short-time external short circuiting on the capacity fading mechanism during long-term cycling of $LiCoO_2$/mesocarbon microbeads battery," *Journal of Power Sources*, vol. 318, pp. 154–162, 2016.

[14] S-W. Jang, H-Y. Lee, K-C. Shin, S. Lee, J-K. Lee, S-J. Lee, B. H-K, and D-S. Rhee, "Synthesis and characterization of spinel $LiMn_2O_4$ for lithium secondary battery," *Journal of Power Sources*, vol. 88, pp. 274–277, 2000.

[15] X. Hao, X. Lin, W. Lu, and B. M. Bartlett, "Oxygen vacancies lead to loss of domain order, particle fracture, and rapid capacity fade in lithium manganospinel ($LiMn_2O_4$) batteries," *ACS Applied Materials & Interfaces*, vol. 6, pp. 10 849–10 857, 2014.

[16] B. Kang and G. Ceder, "Battery materials for ultrafast charging and discharging," *Nature*, vol. 458, pp. 190–193, 2009.

[17] C. Gong, Z. Xue, S. Wen, Y. Ye, and X. Xie, "Advanced carbon materials/olivine $LiFePO_4$ composites cathode for lithium ion batteries," *Journal of Power Sources*, vol. 318, pp. 93–112, 2016.

[18] M. M. Thackeray, C. Wolverton, and E. D. Isaacs, "Electrical energy storage for transportation—approaching the limits of, and going beyond, lithium-ion batteries," *Energy & Environmental Science*, vol. 5, pp. 7854–7863, 2012.

[19] G. Wang, L. Zhang, and J. Zhang, "A review of electrode materials for electrochemical supercapacitors," *Chemical Society Reviews*, vol. 41, pp. 797–828, 2012.

[20] P. Simon and Y. Gogotsi, "Materials for electrochemical capacitors," *Nature Materials*, vol. 7, pp. 845–845, 2008.

[21] S. Chen, R. Ramachandran, V. Mani, and R. Sarawathi, "Recent advancements in electrode materials for the high performance electrochemical supercapacitors A review," *International Journal of Electrochemical Science*, vol. 9, pp. 4072–4085, 2014.

[22] L. L. Zhang and X. S. Zhao, "Carbon-based materials as supercapacitor electrodes," *Chemical Society Reviews*, vol. 38, pp. 2520–2531, 2009.

[23] A. Ahmad, M. Loh, and J. Aziz, "Preparation and characterization of activated carbon from oil palm wood and its evaluation on Methylene blue adsorption," *Dyes and Pigments*, vol. 75, pp. 263–272, 2007.

[24] Y. Huang, E. Ma, and G. Zhao, "Preparation of liquefied wood-based activated carbon fibers by different activation methods for methylene blue adsorption," *RSC Advances*, vol. 5, pp. 70 287–70 296, 2015.

[25] H. Teng, T-S. Yeh, and L-T. Hsu, "Preparation of activated carbon from bituminous coal with phosphoric acid activation," *Carbon*, vol. 36, pp. 1387–1395, 1998.

[26] A. Ahmadpour and D. D. Do, "The preparation of activae carbons from coal by chemical and physical activation," *Carbon*, vol. 34, pp. 471–479, 1996.

[27] W. Sun, S. M. Lipka, C. Swartz, D. Williams, and F. Yang, "Hemp-derived activated carbons for supercapacitors," *Carbon*, vol. 103, pp. 181–192, 2016.

[28] G. Sethia and A. Sayari, "Activated carbon with optimum pore size distribution for hydrogen storage," *Carbon*, vol. 99, pp. 289–294, 2016.

[29] A. D. Roberts, S. Li, and H. Zhang, "Hierarchically porous sulfur-containing activated carbon monoliths via ice-templating and one-step pyrolysis," *Carbon*, vol. 95, pp. 268–278, 2015.

[30] K. Kierzek, E. Frackowiak, G. Lota, G. Gryglewicz, and J. Machnikowski, "Electrochemical capacitors based on highly porous carbons prepared by koh activation," *Electrochimica Acta*, vol. 49, pp. 515–523, 2004.

[31] H. Zhou, S. Zhu, M. Hibino, I. Honma, and M. Ichihara, "Lithium storage in ordered mesoporous carbon (CMK-3) with high reversible specific energy capacity and good cycling performance," *Advanced Materials*, vol. 15, pp. 2107–2111, 2003.

[32] M. Oschatz, E. Kockrick, M. Rose, L. Borchardt, N. Klein, I. Senkovska, T. Freudenberg, Y. Korenblit, G. Yushin, and S. Kaskel, "A cubic ordered, mesoporous carbide-derived carbon for gas and energy storage applications," *Carbon*, vol. 48, pp. 3987–3992,

2010.

[33] M. Enterría, M. F. R. Pereira, J. I. Martins, and J. L. Figueiredo, "Hydrothermal functionalization of ordered mesoporous carbons: The effect of boron on supercapacitor performance," *Carbon*, vol. 95, pp. 72–83, 2015.

[34] J. Cherusseri, R. Sharma, and K. K. Kar, "Helically coiled carbon nanotube electrodes for flexible supercapacitors," *Carbon*, vol. 105, pp. 113–125, 2016.

[35] D. N. Futaba, K. Hata, T. Yamada, T. Hiraoka, Y. Hayamizu, Y. Kakudate, O. Tanaike, H. Hatori, M. Yumura, and S. Iijima, "Shape-engineerable and highly densely packed single-walled carbon nanotubes and their application as super-capacitor electrodes," *Nature Materials*, vol. 5, pp. 987–994, 2006.

[36] Z. Wang, Z. Wu, G. Di Benedetto, J. L. Zunino, and S. Mitra, "Microwave synthesis of highly oxidized and defective carbon nanotubes for enhancing the performance of supercapacitors," *Carbon*, vol. 91, pp. 103–113, 2015.

[37] K. S. Kim, Y. Zhao, H. Jang, S. Y. Lee, J. M. Kim, K. S. Kim, J. H. Ahn, P. Kim, J. Y. Choi, and B. H. Hong, "Large-scale pattern growth of graphene films for stretchable transparent electrodes," *Nature*, vol. 457, pp. 706–710, 2009.

[38] R. Raccichini, A. Varzi, S. Passerini, and B. Scrosati, "The role of graphene for electrochemical energy storage," *Nature Materials*, vol. 14, pp. 271–279, 2015.

[39] K. Kuratani, H. Tanaka, T. Takeuchi, N. Takeichi, T. Kiyobayashi, and N. Kuriyama, "Binderless fabrication of amorphous RuO_2 electrode for electrochemical capacitor using spark plasma sintering technique," *Journal of Power Sources*, vol. 191, pp. 684–687, 2009.

[40] Z. Wu, D. Wang, W. Ren, J. Zhao, G. Zhou, F. Li, and H. Cheng, "Anchoring hydrous RuO_2 on graphene sheets for high-performance electrochemical capacitors," *Advanced Functional Materials*, vol. 20, pp. 3595–3902, 2010.

[41] C-C. Hu, K-H. Chang, M-C. Lin, and Y-T. Wu, "Design and tailoring of the nanotubular arrayed architecture of hydrous RuO_2 for next generation supercapacitors," *Nano Letters*, vol. 6, pp. 2690–2695, 2006.

[42] H. Xia, Y. S. Meng, G. Yuan, C. Cui, and L. Lu, "A symmetric RuO_2RuO_2 supercapacitor operating at 1.6 V by using a neutral aqueous electrolyte," *Electrochemical and Solid-State Letters*, vol. 15, pp. 60–63, 2012.

[43] W. Deng, X. Ji, Q. Chen, and C. E. Banks, "Electrochemical capacitors utilising transition metal oxides: an update of recent developments," *RSC Advances*, vol. 1, pp. 1171–1178, 2011.

[44] Z. Wu, D. Wang, W. Ren, J. Zhao, G. Zhou, F. Li, and H. Cheng, "Anchoring hydrous RuO_2 on graphene sheets for high-performance electrochemical capacitors," *Advanced Functional Materials*, vol. 20, pp. 3595–3602, 2010.

[45] K. Chang, C. Hu, and C. Chou, "Textural and pseudocapacitive characteristics of sol–gel derived $RuO_2 \cdot xH_2O$: Hydrothermal annealing vs. annealing in air," *Electrochimica Acta*, vol. 54, pp. 978–983, 2009.

[46] C. Wang, J. Xu, M. Yuen, J. Zhang, Y. Li, X. Chen, and W. Zhang, "Hierarchical composite electrodes of nickel oxide nanoflake 3D graphene for high-performance pseudocapacitors," *Advanced Functional Materials*, vol. 24, pp. 6372–6380, 2014.

[47] N. Duraisamy, A. Numan, S. O. Fatin, K. Ramesh, and S. Ramesh, "Facile sonochemical synthesis of nanostructured NiO with different particle sizes and its electrochemical properties for supercapacitor application," *Journal of Colloid Interface Science*, vol. 471, pp. 136–144, 2016.

[48] C. Xu, Z. Li, C. Yang, P. Zou, B. Xie, Z. Lin, Z. Zhang, B. Li, F. Kang, and C. P. Wong, "An ultralong, highly oriented nickel-nanowire-array electrode scaffold for high-performance compressible pseudocapacitors," *Advanced Materials*, vol. 28, pp. 4105–4110, 2016.

[49] Z. Yu, B. Duong, D. Abbitt, and J. Thomas, "Highly ordered MnO_2 nanopillars for enhanced supercapacitor performance," *Advanced Materials*, vol. 25, pp. 3302–3306, 2013.

[50] S. K. Nataraj, Q. Song, S. A. Al-Muhtaseb, S. E. Dutton, Q. Zhang, and E. Sivaniah , "Thin, flexible supercapacitors made from carbon nanofiber electrode decorated at room temperature with manganese oxide nanosheets," *Journal of Nanomaterials*, vol. 2013, p. 6, 2013.

[51] N. P. Raval, P. U. Shah, and N. K. Shah, "Adsorptive removal of nickel(II) ions from aqueous environment: A review," *Journal of Environmental Management*, vol. 179, pp. 1–20, 2016.

[52] M. M. Matlock, B. S. Howerton, and D. A. Atwood, "Chemical precipitation of heavy metals from acid mine drainage," *Water Reserach*, vol. 36, pp. 4757–4764, 2002.

[53] A. Dabrowski, Z. Hubicki, P. Podkoscielny, and E. Robens, "Selective removal of the heavy metal ions from waters and industrial wastewaters by ion-exchange method," *Chemosphere*, vol. 56, pp. 91–106, 2004.

[54] H. K. Shon, S. Phuntsho, D. S. Chaudhary, S. Vigneswaran, and J. Cho, "Nanofiltration for water and wastewater treatment – a mini review," *Drinking Water Engineering and Science*, vol. 6, pp. 47–53, 2013.

[55] G. Chen, "Electrochemical technologies in wastewater treatment," *Separation and Purification Technology*, vol. 38, pp. 11–41, 2004.

[56] E. C. Salihi, J. Wang, D. J. L. Coleman, and L. Šiller, "Enhanced removal of nickel(II) ions from aqueous solutions by SDS-functionalized graphene oxide," *Separation Science and Technology*, vol. 51, pp. 1317–1327, 2016.

[57] L. K. Wang, Y-T. Hung, and N. K. Shammas, *Handbook of environmental engineering Physicochemical treatment processes Vol 3*. Totowa, New Jersey: Humana Press, 2005.

[58] E. Worch, *Adsorption technology in water treatment Fundamentals, processes, and modeling*. Berlin Boston: Walter de Gruyter GmbH & Co. KG, 2012.

[59] F. Fu and Q. Wang, "Removal of heavy metal ions from wastewaters: a review," *Journal of Environmental Management*, vol. 92, pp. 407–418, 2011.

[60] N. Akhtar, J. Iqbal, and M. Iqbal, "Removal and recovery of nickel(II) from aqueous solution by loofa sponge-immobilized biomass of Chlorella sorokiniana: characterization studies," *Journal of Hazard Materials*, vol. 108, pp. 85–94, 2004.

Chapter 2

Literature Review

Previous chapter has described the importance of developing electrode materials with good electrochemical properties for efficient energy storage devices and absorbant for Ni (II) ions removal. To achieve good electrochemical properties, including high specific capacity and stable cycling life, materials should have both high surface area and good electronic conductivity. Graphene, as a single carbon atom layer, has a theoretical surface area as high as 2600 m^2 g-1 [1]. It has the potential to reach high specific capacity and stable cycling performance due to the electron adsorption and desorption on graphene surface. To further increase the specific capacity, transition metal and transition metal oxides are used to decorate graphene surface. The fast and reversible Faradaic reactions take place in metal and metal oxides can contribute to a higher specific capacity. Among all the metal materials, bismuth not only has excellent electronic properties but also is considered as environmentally friendly material [2]. In addition, as the by-product of copper and tin refining, the large amount of bismuth make the graphene/bismuth composite materials possible for scale up production. Graphene oxide, which is the intermediate product from graphite to graphene using Hummers' method, also has large surface area. This large surface area gives graphene oxide the potential to become an efficient adsorbant due to the physical adsorption. Compared to graphene, graphene oxide has higher absorption ability on heavy metal ions because the attached oxygen functional groups give graphene oxide a negative surface charge.

In this chapter, the structure of graphene, bismuth, bismuth oxide and bismuth subcarbonate were reviewed. The electrochemical properties of graphene and bismuth compound were summarised. The adsorption abilities of graphene oxide on heavy metal ions were also reviewed.

2.1 Review of graphene

Graphene has attracted tremendous attention since Geim and Novoselov have isolated single-layer graphene and proved its existence as a 2-D stable material [3, 4]. Generally, as the thickness of thin films decreases, the melting temperature of the materials decreases rapidly too [5]. Therefore materials will become unstable at the thickness of dozens of atoms layers [5]. However, graphene exists as a stable solid material at room temperature due to its physical properties such as a tuneable band gap, high mobility and high elasticity [6]. This single atom layer material exhibits superb electronic properties and has been considered as the material for future electronic devices [3].

2.1.1 Structure of graphene

Graphene is a two dimensional allotrope of carbon [7]. It is made of carbon atoms arranged in a hexagonal honeycomb structure [7]. Graphene is the fundamental structure of carbon's other allotropes, such as fullerenes and carbon nanotubes [7]. Fullerenes can be seen as the wrapped up graphene while carbon nanotubes can be seen as graphene rolling along a given direction with reconnected carbon bonds [7, 8]. The lattice structure of graphene leads to an unique band structure, which has been first calculated by Wallace [9]. In the hexagonal lattice of graphene, each carbon atom is about 1.42 Å from its three nearest neighbours and shares one σ bond with the neighbour carbon atoms (as in Figure 2.1) [10]. These σ bonds, formed by the sp^2 hybridization between one s orbital and two p orbitals, are responsible for the carbon lattice structure [7]. Based on the Pauli principle, these σ bonds have filled shell and form a deep valence band [7]. The unaffected third p orbital binds covalently with neighbour carbon atoms and forms π bond, leads to a half-filled conduction band [7, 11]. These π bonds are oriented out of the plane in a z-direction [10]. The electronic band structure of graphene leads to an unusual semi metallic behaviour [9]. The monolayer of graphene exists as a rippled form with no stacking arrangements while the few layers of graphene may contains several stacking arrangements, such as Bernal stacking and rhombohedral stacking [12, 13].

2.1.2 Methods of synthesis of graphene

Mechanical exfoliation of graphite

Graphene can be prepared by mechanical exfoliation of graphite. The ideal case is that graphene

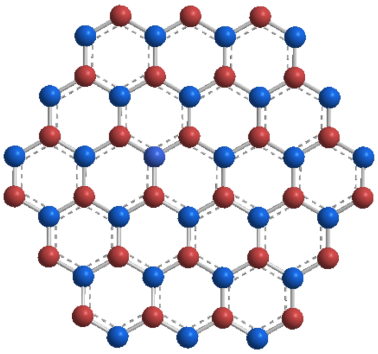

Figure 2.1: Hexagonal honeycomb lattice of graphene [10].

can be peeled from graphite, layer by layer, while overcoming van der Waals forces [14]. Previous studies have used AFM (atomic force microscope) tip to achieve highly oriented graphite by plasma etching [15]. The obtained graphite have a thickness around 200 nm which is approximately 600 layers [15]. Few layer graphene has been developed by K. R. Paton et.al. using a shear exfoliation method [16]. Graphene layers prepared through mechanical exfoliation method have large laterial size with no basal plane defects [16, 17]. However, mechanical exfoliation method has limited scalability and is only suitable for research purposes [17].

Chemical exfoliation of graphite

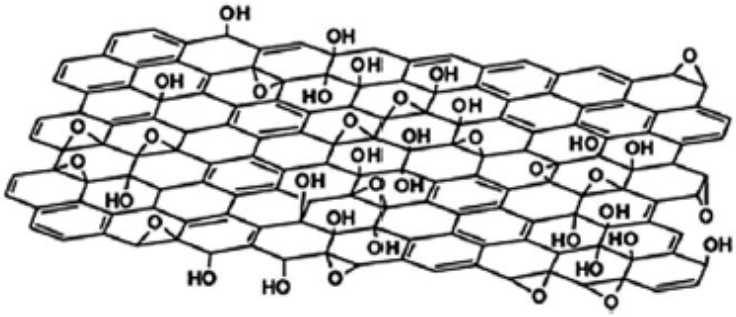

Figure 2.2: Lerf-Klinowski model of grapehen oxide [18].

Graphene can also be synthesised by chemical exfoliation of graphite. By chemically modifying graphite to produce an intermediate graphite oxide dispersion, the basal spacing between carbon layers increases due to the attached oxidation functional groups [19]. In addition, the hydrophilicity of graphite oxide leads water to intercalate between the carbon layers and separate them as individuals [11]. Graphene oxide has been described as a layer structured material with hydroxyl and epoxy groups on the surface and carboxylic and carbonyl groups at the edges, as in Figure 2.2 [18]. Reduced graphene oxide (rGO) can be obtained through thermal reduction or chemical reduction by removal of the attached functional groups [20]. During heat treatment, the rapid temperature increase causes the oxygen functional groups which at-

tached on carbon layers decomposed into gases, therefore creates pressure between carbon layers and prevents them from stacking back together [20]. Compared to thermal reduction, chemical reduction process is more cheapter due to the less requirement for equipment [20]. Hydrazine has been widely studied and accepted as an effective reducing agent for graphene oxide [21]. Chemical reduction method is able to prepare rGO on a large scale but cannot remove the functional groups fully [20].

Chemical vapour deposition (CVD)

Chemical vapour deposition is a method used to produce high quality solid material. By exposing the substrate in a gases compounds environment, these gases compounds decompose on the substrate surface and form a thin film [22]. Graphene layers can be prepared through CVD method approach by the deposition onto transition metal substrates [23]. Previous study successfully synthesised graphene layers with 300 nm thickness on SiO_2/Si substrates using a gas mixture of CH_4, H_2 and Ar under 1000°C [6]. Ni, Pd, Ru, Ir and Cu have all been studied as the metal substrates to prepare graphene [6, 24–27]. Graphene prepared by this method has high quality with less structure defects [23]. Since most of the transition metals can be etched by strong acids, the synthesized graphene can be easily transferred to other substrates [28].

2.1.3 Electrochemical properties of graphene

Graphene has been considered as the ideal material for supercapacitors [29, 30]. It has a high carrier mobility (up to 200,000 cm^2 V^{-1} s^{-1}) and current carrying capacity as high as 109 A cm^2 [31, 32]. Based on the capacitance generation mechanism of graphene, in which ions are adsorb and desorb on the material surface, graphene has been classified as the electrochemical double layer capacitor (EDLC) [33]. This type of supercapacitor has fast charge/ discharge speed and excellent cycle life performance [34]. Ultrathin graphene paper with 25 nm thickness shows a specific capacitance of 111 F g^{-1} [35]. Graphene paper prepared from graphene aerogel by mechanically pressing method has a specific capacitance value as high as 172 F g^{-1} at the charge/discharge rate of 1 A g^{-1} [36]. Graphene exfoliated under high vacuum at 200°C shows high capacitance value of 200 F g^{-1} [37]. However, the capacitance value of graphene reported in literature are much lower than its theoretical value, 550 F g^{-1} [17]. This is because graphene sheets are easily stacked back together which causes difficulty for ions in electrolytes to access [38]. Therefore, by decorating graphene with defects, impurities or electroactive materials, such as metals or metal oxides, more active sites are obtained and high

specific capacitance values can be achieved [17].

Chemically modified graphene with a specific capacitance of 135 F g^{-1} in aqueous electrolytes was measured [39]. Graphene decorated by carbon nanotubes (with a ratio of 5:1) achieved a specific capacitance of 177 F g^{-1} at the current density of 1 A g^{-1} [40]. This material has only 10% drop of its capacitance value after 1000 cycles [40]. By using KOH activation, graphene with nano pores structure has a specific capacitance of 200 F g^{-1} at the current density of 0.7 A g^{-1} [30]. Nitrogen doped rGO aerogel synthesized by hydrothermal method achieves a specific capacitance as high as 765 F g^{-1} at the current density of 1 A g^{-1} [41].

2.1.4 Adsorption abilities of heavy metal ions by graphene oxide

The presence of metal ions in the environment is a major concern due to their toxic effect on humans and the environment [42]. Metal ions, unlike other organic pollutants which can undergo biological degradation, do not degrade into harmless final products and are toxic to many life forms [43]. Some materials, such as activate carbon [44, 45], carbon nanotube [46, 47], polymeric materials [48, 49], zeolites [50], and metal oxides [51], have been used to remove heavy metal ions from water. Recently, graphene oxide has also been studied for their adsorption abilities of heavy metal ions from aqueous solutions. Graphene oxide is a layered structured material with hydrogen and epoxy groups attached on its surface [52]. These attached hydrophilic polar groups improve the dispersibility of graphene oxide in aqueous media and result in swelling, intercalating and ions exchanging properties of the dispersion [6, 52]. In addition, the large surface area of graphene oxide also provides the potential to reach high adsorption abilities through both electrostatic and coordinate approaches [52, 53].

Previous studies have shown that graphene oxide has good adsorption abilities for Cu^{2+} [52], Pb^{2+} [54], Hg^{2+} [55], Co^{2+} [56], and Ni^{2+} [57]. Some functional groups such as chitosan [58], amino [59], poly(N-vinylcarbazole) [60], 4-aminothiophenol and 3-aminopropyltriethoxysilane [61] were used to decorate graphene oxide to further enhance their adsorption ability.

Graphene oxide has a Ni^{2+} removal percentage as high as 89.90% with the initial concentration of 30 ppm of Ni^{2+} [42]. When the initial concentration increases to 200 ppm, the removal percentage is reduced to 78.00% [42]. Fe_3O_4 decorated graphite oxide has a Ni^{2+} adsorption capacity of 22.07 mg g^{-1} [62]. The adsorption equilibrium of Ni^{2+} was obtained after 240 min with a removal percentage higher than 85% [62].

2.2 Review of bismuth and bismuth compounds

As a transition metal, bismuth has a stable +3 oxidation state and can also exist at +5 oxidation state. It has the potential to offer high electrical capacity based on the Faradaic redox reaction between 0 and +3 oxidation state [63]. In addition, bismuth and most of its compounds have been considered as safe, non-toxic, and non-carciogenic materials in spite of their heavy metal nature [2].

2.2.1 Structure of bismuth and bismuth compounds

Bismuth is a metallic element in V group on the periodic table [64]. For bulk material, bismuth has a rhombohedral lattice structure as in Figure 2.3 [65]. In this rhombohedral structure, each bismuth atom has three equidistant neighbour atoms and three second neighbour atoms with slightly further distance [65].

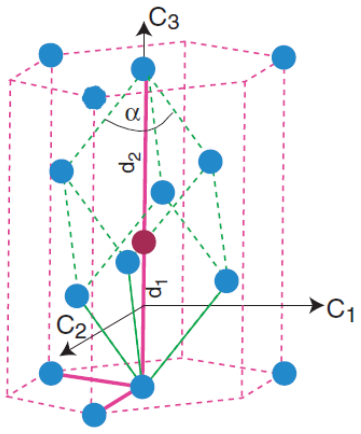

Figure 2.3: Bulk structure of Bi (rhombohedral unit cell) [65].

Bismuth, as a semimetal element, has many unique electronic properties based on its electronic structure [66]. It not only has a Fermi wavelength as long as 30 nm but also has the highest Hall coefficient among all metals [66]. With the thickness of bismuth reduced, a high density of states crossing the Fermi level is formed, which leads to the failure of band gap opening [66]. Therefore, with the thickness of bismuth further reduced to nanometres, the conducting properties of bismuth change from small gap semiconductor to metal as a function of its thickness [67]. Previous study indicates that the quantum size effects of bismuth has been already observed in structures smaller than a few hundred nanometres [68].

2.2.2 Synthesis method of bismuth and bismuth compounds

Bismuth

Bismuth nanowires can be synthesized within an alumina membranes through electrochemical deposition technique [69]. Prepared Bi nanowires have an average pore diameter of 73 nm (as in Figure 2.4 a)) [69]. Bismuth nanowires can also be prepared through a solvothermal pro-

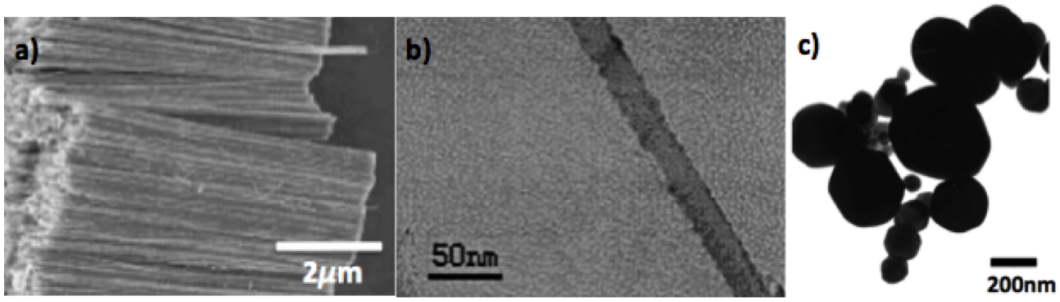

Figure 2.4: Bismuth prepared by a) electrodeposition b) solvothermal c) thermal plasma [69–71].

cess [70]. Ethylene diamine was added and used as the reducing agent [70]. The solvothermal reaction was kept at 160°C for 6 hours in a Teflon vessel [70]. Bi nanowires prepared through this solvothermal method have diameters of 20-30 nm and lengths of 0.2-2.5 μm (as in Figure 2.4 b)) [70]. Bismuth nanoparticles have been reported to be prepared through the thermal plasma method [71]. Bismuth powder was placed in Mo boat while the mixture of Ar/H_2 was used till the vacuum gauge reached 20 Pa [71]. Under high temperature condition, Bi nanoclusters quickly collided and formed nano particles (as in Figure 2.4 c)) [71]. Polyol process, in which ethylene glycol was used as the solvent, has been used to synthesise bismuth carbon nanotube composite (Bi-CNT) [72].

These synthesized bismuth matertials were only charaterized by either X-ray diffraction (XRD) or selected area electron diffraction (SEAD). No chemcial fingerprint such as X-ray photoemission spectroscopy (XPS) were used for the surface charaterization. Previous studies have reported that bismuth metal nanostructure, such as nanowires or nanoparticles, readily oxidized when exposed to air at atmospheric pressure [73–75]. Metallic Bi wires typically have an oxide layer of $\sim$1 nm thick after 4 h exposure to air [74]. After 48 h exposure, the thickness of the oxide layer is $\sim$4 nm [74]. High temperature hydrogen attack (HTHA) and ammonia environments were found to reduce the oxide without damaging the Bi metal after a sufficient amount of time, but the oxide was found to reform in less than 1 min when exposure to air [75]. Therefore, the surface of these synthesized bismuth materials may contain Bi_2O_3

as impurity.

Bismuth oxide

Bismuth oxide nanoparticles with size around 50 nm have been synthesized by sol-gel method and thermal decomposition method [76–78]. Bismuth oxide can also be synthesized through electrodeposition method. Thin layer of Bi_2O_3 is deposited on the copper substrate in galvanostatic mode using chronopotentiometry [63]. The obtained thin film of Bi_2O_3 has a thickness of 0.74 μm [63]. By using electron potential oscillation during electrodeposition, hierarchical rippled Bi_2O_3 is achieved (as shown in Figure 2.5) [79]. These rippled Bi_2O_3 nanobelts have width of 250-300 nm and thickness of 10-30 nm [79].

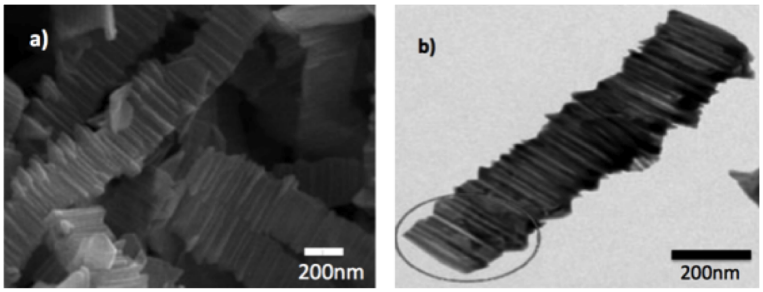

Figure 2.5: Images of rippled bismuth oxide a) SEM image b) TEM image [79]

Facile solvothermal method has been used to synthesis graphene/bismuth oxide composite [80]. Graphene nanosheet decorated by nano-sized bismuth oxide composite was synthesized through this method by using N, N-dimethyl formamide (DMF) as the solvent at 180°C for 12 hours [80].

Bismuth subcarbonate

Bismuth subcarbonate can be synthesised from bismuth nitrate by hydrothermal method with temperature around 180°C [81, 82]. This material generally has a structure assembled from $Bi_2O_2CO_3$ nanosheets. By adding surfactant polyvinylpyrrolidone (PVP), the prepared $Bi_2O_2CO_3$ shows a hierarchical flower-like structure as Figure 2.6 [82]. The flower-like $Bi_2O_2CO_3$ has a microsphere structure with diameter from 2-3 μm [82]. These as-prepared $Bi_2O_2CO_3$ microflowers can then be mixed with graphene oxide for a further hydrothermal reaction and form graphene- $Bi_2O_2CO_3$ composite, as in Figure 2.7 [82].

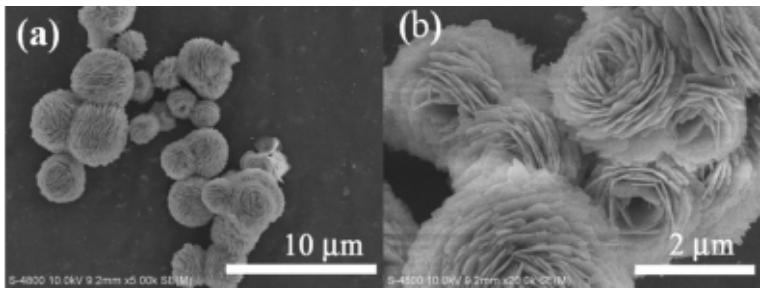

Figure 2.6: SEM images of flower-like structure bismuth subcarbonate [82]

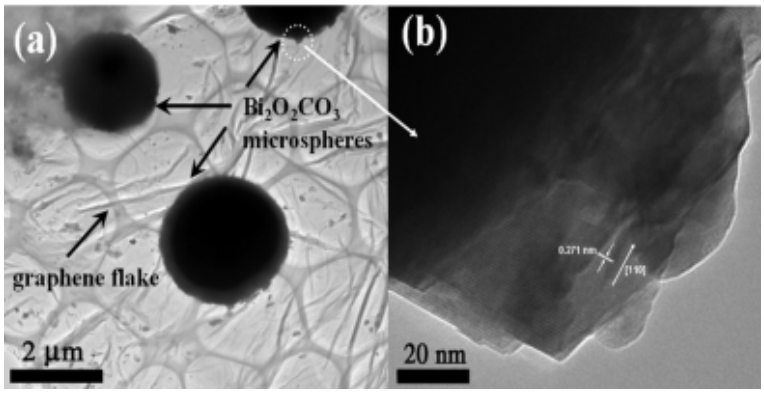

Figure 2.7: TEM images of flower-like structure bismuth subcarbonate [82]

2.2.3 Electrochemical properties of bismuth and bismuth compounds

Bismuth and bismuth compounds are considered as battery-type electrode [33]. This type of electrode exhibits high energy density and high specific capacity based on the fast and reversible redox reactions that happen on the electrode surface [33]. Compared to EDLC, battery type electrodes generally have higher specific capacity values but less stable cycling performance [33]. The electrochemical properties of bismuth and bismuth compounds have been studied. Bi_2O_3 with thin film structure synthesized through electrodeposition method achieves a specific capacitance of 68 F g^{-1} at a scanning rate of 100 mV^{-1} [63]. Bi_2O_3 with rippled film structure achieves higher specific capacitance of 250 F g^{-1} compared to the smooth surface one [82]. β-Bi_2O_3 synthesised through a sol-gel method achieves a specific capacitance of 527 F g^{-1} [83]. However, the capacitance retention has a nearly 40% drop after 1000 cycles [83]. Previous studies have also reported the electrochemical properties of Bi_2O_3/ carbon composite materials [84]. Bi_2O_3 with rGO composite synthesised through hydrothermal and thermal decomposition method has a specific capacitance of 94 F g^{-1} [84]. Bi_2O_3 with activated carbon composite synthesized through vacuum impregnation and roasting process achieved a specific capacitance of 333 F g^{-1} at the current density of 1 A g^{-1} [85]. Graphene nanosheet bismuth oxide composite prepared through facile solvothermal method has obtained

a specific capacitance of 255 F g^{-1} [80].

However, previous literature have pointed out that specific capacitance should only be used to describe pure capacitor behaviours, which show rectangular cyclic voltammetry curve and triangular charge discharge curve [86, 87]. For most of the bismuth compound materials, which have redox peaks in cyclic voltammetry curves and plateau in charge discharge curve, specific capacity is suggested to be used to describe their electrochemical properties [86–88].

2.3 Summary

In this chapter, the structure, synthesis methods and electrochemical properties of both graphene and bismuth compounds were reviewed. The synthesis methods of bismuth and its compounds generally involve high temperature, long reaction time, and special equipment which limits the potential for scale up production. When considering their application as electrodes in electrochemical energy storage devices, bismuth and its compounds have high capacity value based on the fast and reversible redox reaction while graphene, as an EDLC, shows good electronic conductivity and stable cycling performance. Therefore, in this work (chapters 4, 5 and 6) rGO/Bi, Bi_2O_3-rGO and rGO/$Bi_2O_2CO_3$ were synthesized under relatively low temperature and short reaction time. These composite materials have both high capacity value and good cycling performance. In addition, the abilities of adsorption of Ni(II) ions on graphene oxide and graphene oxide modified by sodium dodecyl sulfate (SDS) were studied in chapter 7.

References

[1] Y. Qian, I. M. Ismail and A. Stein, "Ultralight, high surface area, multifunctional graphene based aerogels from self assembly of graphene oxide and resol," *Carbon*, vol. 68, pp. 221–231, 2014.

[2] N. M. Leonard, L. C. Wieland, and R. S. Mohan, "Applications of bismuth(III) compounds in organic synthesis," *Tetrahedron*, vol. 58, pp. 8373–8397, 2002.

[3] K. S. Novoselov, A. K. Geim, S. V. Morozov, D. Jiang, Y. Zhang, S. V. Dubonos, I. V. Grigorieva, and A. A. Firsov, "Electric field effect in automically thin carbon films," *Science*, vol. 306, pp. 666–669, 2004.

[4] A. K. Geim and K. S. Novoselov, "The rise of graphene," *Nature Materials*, vol. 6, pp. 183–191, 2007.

[5] J. A. Venables, G. D. T. Spiller, and M. Hanbucken, "Nucleation and growth of thin films," *Reports on Progress in Physics*, vol. 47, pp. 399–459, 1984.

[6] K. S. Kim, Y. Zhao, H. Jang, S. Y. Lee, J. M. Kim, K. S. Kim, J. H. Ahn, P. Kim, J. Y. Choi, and B. H. Hong, "Large-scale pattern growth of graphene films for stretchable transparent electrodes," *Nature*, vol. 457, pp. 706–710, 2009.

[7] A. H. Castro Neto, F. Guinea, N. M. R. Peres, K. S. Novoselov, A. K. Geim, "The electronic properties of graphene," *Reviews of Modern Physics*, vol. 81, pp. 109–162, 2009.

[8] F. C. Graovac and O. Ori, *The mathematics and topology of fullerences*. Springer, 2011.

[9] P. R. Wallace, "The band theory of graphite," *Physical Review*, vol. 71, pp. 622–634, 1947.

[10] P. Avouris, "Graphene: electronic and photonic properties and devices," *Nano Letters*, vol. 10, pp. 4285–4295, 2010.

[11] M. J. Allen, V. C. Tung, and R. B. Kaner, "Honeycomb carbon: a review of graphene," *Chemcial Reviews*, vol. 110, pp. 132–145, 2010.

[12] K. F. Mak, J. Shan, and T. F. Heinz, "Electronic structure of few layer graphene: experimental demonstration of strong dependence on stacking sequence," *Physical Review Letters*, vol. 104, pp. 176 404(1–4), 2010.

[13] R.S.Edwards and K. S. Coleman, "Graphene synthesis: relationship to applications," *Nanoscale*, vol. 5, pp. 38–51, 2013.

[14] M. Yi and Z. Shen, "A review on mechanical exfoliation for the scalable production of graphene," *Journal of Materials Chemistry A*, vol. 3, pp. 11 700–11 715, 2015.

[15] X. Lu, M. Yu, H. Huang, and R. S. Ruoff, "Tailoring graphite with the goal of achieving single sheets," *Nanotechnology*, vol. 10, pp. 269–272, 1999.

[16] K. R. Paton, E. Varrla, C. Backes, R. J. Smith, U. Khan, A. O'Neill, C. Boland, M. Lotya, O. M. Istrate, P. King, T. Higgins, S. Barwich, P. May, P. Puczkarski, I. Ahmed, M. Moebius, H. Pettersson, E. Long, J. Coelho, S. E. O'Brien, E. K. McGuire, B. M. Sanchez, G. S. Duesberg, N. McEvoy, T. J. Pennycook, C. Downing, A. Crossley, V. Nicolosi, and J. J. N. Coleman, "Scalable production of large quantities of defect-free few-

layer graphene by shear exfoliation in liquids," *Nature Materials*, vol. 13, pp. 624–630, 2014.

[17] K. Chen, S. Song, F. Liu, and D. Xue, "Structural design of graphene for use in electrochemical energy storage devices," *Chemical Society Reviews*, vol. 44, pp. 6230–6257, 2015.

[18] D. R. Dreyer, S. Park, C. W. Bielawski, and R. S. Ruoff, "The chemistry of graphene oxide," *Chemistry Society Reviews*, vol. 39, pp. 228–240, 2010.

[19] W. S. Hummers and R. E. Offman, "Preparation of graphite oxide," *Journal of American Chemistry Society*, vol. 80, pp. 1339–1339, 1958.

[20] S. Pei and H. Cheng, "The reduction of graphene oxide," *Carbon*, vol. 50, pp. 3210–3228, 2010.

[21] S. Stankovich, D. A. Dikin, R. D. Piner, K. A. Kohlhaas, A. Kleinhammes, Y. Jia, Y. Wu, S. T. Nguyen, and R. S. Ruoff, "Synthesis of graphene-based nanosheets via chemical reduction of exfoliated graphite oxide," *Carbon*, vol. 45, pp. 1558–1565, 2007.

[22] A. C. Jones and M. L. Hitchman, *Chemical vapour deposition, precursors, processes and applictions*. Cambridge: Royal Society of Chemistry, 2009.

[23] C. Mattevi, H. Kim, and M. Chhowalla, "A review of chemical vapour deposition of graphene on copper," *Journal of Materials Chemistry*, vol. 21, pp. 3324–3334, 2011.

[24] S. Kwon, C. V. Ciobanu, V. Petrova, V. B. Shenoy, J. Bareno, V. Gambin, I. Petrov, and S. Kodambaka, "Growth of semiconducting graphene on palladium," *Nano Letters*, vol. 9, pp. 3985–3990, 2009.

[25] P. W. Sutter, J. I. Flege, and E. A. Sutter, "Epitaxial graphene on ruthenium," *Nature Materials*, vol. 7, pp. 406–411, 2008.

[26] J. Coraux, A. T. N'Diaye, C. Busse, and T. Michely, "Structural coherency of graphene on Ir(111)," *Nano Letters*, vol. 8, pp. 565–570, 2008.

[27] X. Li, W. Cai, J. An, S. Kim, J. Nah, D. Yang, R. Piner, A. Velamakanni, I. Jung, E. Tutuc, S. K. Banerjee, L. Colombo, and R. S. Ruoff, "Large-area synthesis of high-quality and uniform graphene films on copper foils," *Science*, vol. 324, pp. 1312–1314, 2008.

[28] Z. Juang, C. Wu, A. Lu, C. Su, K. Leou, F. Chen, and C. Tsai, "Graphene synthesis by chemical vapor deposition and transfer by a roll-to-roll process," *Carbon*, vol. 48, pp.

3169–3174, 2010.

[29] Y. Y. Sun, Q. Q. Wu, and G. G. Shi, "Graphene based new energy materials," *Energy & Environmental Science*, vol. 4, pp. 1113–1132, 2011.

[30] Y. Zhu, S. Murali, M. D. Stoller, K. J. Ganesh, W. Cai, P. J. Ferreira, A. Pirkle, R. M. Wallace, K. A. Cychosz, M. Thommes, D. Su, E. A. Stach, and R. S. Ruoff, "Carbon-based supercapacitors produced by activation of graphene," *Science*, vol. 332, pp. 1537–1541, 2011.

[31] K. I. Bolotin, K. J. Sikes, Z. Jiang, M. Klima, G. Fudenberg, J. Hone, P. Kim, and H. L. Stormer, "Ultrahigh electron mobility in suspended graphene," *Solid State Communications*, vol. 146, pp. 351–355, 2008.

[32] P. Avouris and C. Dimitrakopoulos, "Graphene: synthesis and applications," *Materials Today*, vol. 15, pp. 86–97, 2012.

[33] B. E. Conway, *Electrochemical supercapacitors: Scientific fundamentals and technological applications*. New York: Kluwer Academic/Plenum Publisher, 1999.

[34] Y. K. Y. K. Y. Hwang, S. Lee and K. Lee, "A new approach of structural and chemical modification on graphene electrodes for high-performance supercapacitors," *Carbon*, vol. 100, pp. 7–15, 2016.

[35] A. Yu, I. Roes, A. Davies, and Z. Chen, "Ultrathin, transparent, and flexible graphene films for supercapacitor application," *Applied Physics Letters*, vol. 96, pp. 253 105(1–3), 2010.

[36] F. Liu, S. Song, D. Xue, and H. Zhang, "Folded structured graphene paper for high performance electrode materials," *Advanced Materials*, vol. 24, pp. 1089–1094, 2012.

[37] W. Lv, D. Tang, Y. He, C. You, Z. Shi, X. Chen, C. Chen, P. Hou, C. Liu, and Q. Yang, "Low temperature exfoliatede graphenes vacuum promoted exfoliation and electrochemical energy storage," *ACS Nano*, vol. 3, pp. 3730–3736, 2009.

[38] N. Jung, S. Kwon, D. Lee, D. M. Yoon, Y. M. Park, A. Benayad, J. Y. Choi, and J. S. Park, "Synthesis of chemically bonded graphene/carbon nanotube composites and their application in large volumetric capacitance supercapacitors," *Advanced Materials*, vol. 25, pp. 6854–6858, 2013.

[39] M. D. Stoller, S. Park, Y. Zhu, J. An, and R. S. Ruoff, "Graphene based ultracapacitors," *Nano Letters*, vol. 8, pp. 3498–3502, 2008.

[40] Q. Yang, S. Pang, and K. Yung, "Electrochemically reduced graphene oxide/carbon nanotubes composites as binder-free supercapacitor electrodes," *Journal of Power Sources*, vol. 311, pp. 144–152, 2016.

[41] P. Iamprasertkun, A. Krittayavathananon, and M. Sawangphruk, "N-doped reduced graphene oxide aerogel coated on carboxyl-modified carbon fiber paper for high-performance ionic-liquid supercapacitors," *Carbon*, vol. 102, pp. 455–461, 2016.

[42] I. Sheet, A. Kabbani, and H. Holail, "Removal of heavy metals using nanostructured graphite oxide, silica nanoparticles and silica/ graphite oxide composite," *Energy Procedia*, vol. 50, pp. 130–138, 2014.

[43] V. K. Gupta, M. Gupta, and S. Sharma, "Process development for the removal of lead and chromium from aqueous solutions using red mud an aluminium industry waste," *Water Research*, vol. 35, pp. 1125–1134, 2001.

[44] H. Oda and Y. Nakagawa, "Removal of ionic substances from dilute solution using activated carbon electrodes," *Carbon*, vol. 41, pp. 1037–1047, 2003.

[45] Y. Kikuchi, Q. Qian, M. Machida, and H. Tatsumoto, "Effect of ZnO loading to activated carbon on Pb(II) adsorption from aqueous solution," *Carbon*, vol. 44, pp. 195–202, 2006.

[46] L. Maggini, J. M. Raquez, R. Marega, A. J. Jensen, F. Pineux, F. Meyer, P. Dubois, and D. Bonifazi, "Magnetic poly(vinylpyridine)-coated carbon nanotubes: an efficient supramolecular tool for wastewater purification," *ChemSusChem*, vol. 6, pp. 367–373, 2013.

[47] Y. Li, J. Ding, Z. Luan, Z. Di, Y. Zhu, C. Xu, D. Wu, and B. Wei, "Competitive adsorption of Pb^{2+}, Cu^{2+} and Cd^{2+} ions from aqueous solutions by multiwalled carbon nanotubes," *Carbon*, vol. 41, pp. 2787–2792, 2003.

[48] M. X. Tan, Y. N. Sum, J. Y. Ying, and Y. Zhang, "A mesoporous poly-melamine-formaldehyde polymer as a solid sorbent for toxic metal removal," *Energy & Environmental Science*, vol. 6, pp. 3254–3259, 2013.

[49] B. Li, Y. Zhang, D. Ma, Z. Shi, and S. Ma, "Mercury nano-trap for effective and efficient removal of mercury(ii) from aqueous solution," *Nature Communications*, vol. 5, pp. 5537(1–7), 2014.

[50] N. Arancibia-Miranda, S. E. Baltazar, A. Garcia, D. Munoz-Lira, P. Sepulveda, M. A. Rubio, and D. Altbir, "Nanoscale zero valent supported by zeolite and montmorillonite:

Template effect of the removal of lead ion from an aqueous solution," *Journal of Hazadrous Materials*, vol. 301, pp. 371–380, 2016.

[51] J. Hu, L. Zhong, W. Song, and L. Wan, "Synthesis of hierarchically structured metal oxides and their application in heavy metal ion removal," *Advanced Materials*, vol. 20, pp. 2977–2982, 2008.

[52] X. Mi, G. Huang, W. Xie, W. Wang, Y. Liu, and J. Gao, "Preparation of graphene oxide aerogel and its adsorption for Cu^{2+} ions," *Carbon*, vol. 50, pp. 4856–4864, 2012.

[53] S. Wang, H. Sun, H. M. Ang, and M. O. Tadé, "Adsorptive remediation of environmental pollutants using novel graphene-based nanomaterials," *Chemical Engineering Journal*, vol. 226, pp. 336–347, 2013.

[54] Z. Han, Z. Tang, S. Shen, B. Zhao, G. Zheng, and J. Yang, "Strengthening of graphene aerogels with tunable density and high adsorption capacity towards Pb^{2+}," *Scientific Reports*, vol. 4, pp. 5025(1–6), 2014.

[55] W. Gao, M. Majumder, L. B. Alemany, T. N. Narayanan, M. A. Ibarra, B. K. Pradhan, and P. M. Ajayan, "Engineered graphite oxide materials for application in water purification," *Applied Materials & Interfaces*, vol. 3, pp. 1821–1826, 2011.

[56] F. Fang, L. Kong, J. Huang, S. Wu, K. Zhang, X. Wang, B. Sun, Z. Jin, J. Wang, X. J. Huang, and J. Liu, "Removal of cobalt ions from aqueous solution by an amination graphene oxide nanocomposite," *Journal of Hazardous Materials*, vol. 270, pp. 1–10, 2014.

[57] Y. Lei, F. Chen, Y. Luo, and L. Zhang, "Synthesis of three-dimensional graphene oxide foam for the removal of heavy metal ions," *Chemical Physics Letters*, vol. 593, pp. 122–127, 2014.

[58] B. Yu, J. Xu, J. Liu, S. Yang, J. Luo, Q. Zhou, J. Wan, R. Liao, H. Wang, and Y. Liu, "Adsorption behavior of copper ions on graphene oxide–chitosan aerogel," *Journal of Environmental Chemical Engineering*, vol. 1, pp. 1044–1050, 2013.

[59] L. Chen, D. Zhao, X. Wang, and C. Chen, "One-step fabrication of amino functionalized magnetic graphene oxide composite for uranium(VI) removal," *Journal of Colloid and Interface Science*, vol. 472, pp. 99–107, 2016.

[60] Y. F. Musico, C. M. Santos, M. P. Dalida, and D. F. Rodrigues, "Improved removal of lead(II) from water using a polymer-based graphene oxide nanocomposite," *Journal of*

Materials Chemistry A, vol. 1, pp. 3789–3796, 2013.

[61] D. Chen, H. Zhang, K. Yang, and H. Wang, "Functionalization of 4-aminothiophenol and 3-aminopropyltriethoxysilane with graphene oxide for potential dye and copper removal," *Journal of Hazardous Materials*, vol. 310, pp. 179–187, 2016.

[62] X. Guo, B. Du, Q. Wei, J. Yang, L. Hu, L. Yan, and W. Xu, "Synthesis of amino functionalized magnetic graphenes composite material and its application to remove Cr(VI), Pb(II), Hg(II), Cd(II) and Ni(II) from contaminated water," *Journal of Hazardous Materials*, vol. 278, pp. 211–220, 2014.

[63] T. P. Gujar, V. R. Shinde, C. D. Lokhande, and S. H. Han, "Electrosynthesis of Bi_2O_3 thin films and their use in electrochemical supercapacitors," *Journal of Power Sources*, vol. 161, pp. 1479–1485, 2006.

[64] Y. Li, J. Wang, Z. Deng, Y. Wu, X. Sun, D. Yu, and P. Yang, "Bismuth nanotubes a rational low temperature synthetic route," *Journal of the American Chemcial Society*, vol. 123, pp. 9904–9905, 2001.

[65] P. Hofmann, "The surfaces of bismuth: Structural and electronic properties," *Progress in Surface Science*, vol. 81, pp. 191–245, 2006.

[66] J. T. Sun, H. Huang, S. L. Wong, H. J. Gao, Y. P. Feng, and A. T. Wee, "Energy-gap opening in a Bi(110) nanoribbon induced by edge reconstruction," *Physical Review Letters*, vol. 109, pp. 246 804(1–5), 2012.

[67] Y. M. Koroteev, G. Bihlmayer, E.V. Chulkov, and S. Blügel, " First-principles investigation of structural and electronic properties of ultrathin Bi films," *Physical Review B*, vol. 77, pp. 045 428(1–7), 2008.

[68] Y. F. Komnik and E. I. Bukhshtab, "Observation of the quantum and classical size effects in polycrystalline thin bismuth films," *Soviet Physics Jetp*, vol. 27, pp. 34–37, 1968.

[69] L. Li, Y. Zhang, G. Li, X. Wang, and L. Zhang, "Synthetic control of large-area, ordered bismuth nanowire arrays," *Materials Letters*, vol. 59, pp. 1223–1226, 2005.

[70] Y. Gao, H. Niu, C. Zeng, and Q. Chen, "Preparation and characterization of single crystalline bismuth nanowires by a low temperature solvothermal process," *Chemical Physics Letters*, vol. 367, pp. 141–144, 2003.

[71] L. Wang, Z. Cui, and Z. Zhang, "Bi nanoparticles and Bi_2O_3 nanorods formed by thermal plasma and heat treatment," *Surface and Coatings Technology*, vol. 201, pp. 5330–

5332, 2007.

[72] N. Pikroh and P. Vanalabhpatana, "Bismuth-carbon nanotube composite modified carbon paste electrode for the determination of heavy metal ions," *ECS Transactions*, vol. 45, pp. 39–46, 2013.

[73] M. G. Hale, R. Little, M. A. Salem, J. H. Hedley, B. R. Horrocks, and L. Šiller, "Formation of bismuth oxide nanowires by simultaneous templating and electrochemical adhesion of DNA on Si/SiO_2," *Thin Solid Films*, vol. 520, pp. 7044–7048, 2012.

[74] Z. Zhang, D. Gekhtman, M. S. Dresselhaus, and J. Y. Ying, "Processing and characterization of single-crystalline ultrafine bismuth nanowires," *Chemistry of Materials*, vol. 11, pp. 1659–1665, 1999.

[75] S. B. Cronin, Y. Lin, P. L. Gai, O. Rabin, M. R. Black, G. Dresselhau, and M. S. Dresselhaus, "4-point resistance measurements of individual Bi nanowires," *Materials Research Society Symposium C*, vol. 635, pp. 5–7, 2000.

[76] M. Mallahi, A. Shokuhfar, M. R. Vaezi, A. Esmaeilirad, and V. Mazinani, "Synthesis and characterization of bismuth oxide nanoparticles via solgel method," *American Journal of Engineering Research*, vol. 3, pp. 162–165, 2014.

[77] R. K. Jha, R. Pasricha, and V. Ravi, "Synthesis of bismuth oxide nanoparticles using bismuth nitrate and urea," *Ceramics International*, vol. 31, pp. 495–497, 2005.

[78] M. M. Patil, V. V. Deshpande, S. R. Dhage, and V. Ravi, "Synthesis of bismuth oxide nanoparticles at 100°C," *Materials Letters*, vol. 59, pp. 2523–2525, 2005.

[79] F. Zheng, G. Li, Y. Ou, Z. Wang, C. Su, and Y. Tong, "Synthesis of hierarchical rippled Bi_2O_3 nanobelts for supercapacitor applications," *Chemical Communications*, vol. 46, pp. 5021–5023, 2010.

[80] H. Wang, Z. Hu, Y. Chang, Y. Chen, Z. Lei, Z. Zhang, and Y. Yang, "Facile solvothermal synthesis of a graphene nanosheet–bismuth oxide composite and its electrochemical characteristics," *Electrochimica Acta*, vol. 55, pp. 8971–8980, 2010.

[81] H. Huang, N. Tian, S. Jin, Y. Zhang, and S. Wang, "Syntheses, characterization and nonlinear optical properties of a bismuth subcarbonate $Bi_2O_2CO_3$," *Solid State Sciences*, vol. 30, pp. 1–5, 2014.

[82] P. Madhusudan, J. Yu, W. Wang, B. Cheng, and G. Liu, "Facile synthesis of novel hierarchical graphene-$Bi_2O_2CO_3$ composites with enhanced photocatalytic performance under

visible light," *Dalton Transactions*, vol. 41, pp. 14 345–14 353, 2012.

[83] X. Huang, W. Zhang, Y. Tan, J. Wu, Y. Gao, and B. Tang, "Facile synthesis of rod-like Bi_2O_3 nanoparticles as an electrode material for pseudocapacitors," *Ceramics International*, vol. 42, pp. 2099–2105, 2016.

[84] M. Ciszewski, A. Mianowski, P. Szatkowski, G. Nawrat, and J. Adamek, "Reduced graphene oxide–bismuth oxide composite as electrode material for supercapacitors," *Ionics*, vol. 557-563, p. 21, 2015.

[85] S. Wang, C. Jin, and W. Qian, "Bi_2O_3 with activated carbon composite as a supercapacitor electrode," *Journal of Alloys and Compounds*, vol. 615, pp. 12–17, 2014.

[86] T. Brousse, D. Belanger, and J. W. Long, "To be or not to be pseudocapacitive?" *Journal of Electrochemistry Society*, vol. 162, pp. 5185–5189, 2015.

[87] V. Augustyn, P. Simon, and B. Dunn, "Pseudocapacitive oxide materials for high-rate electrochemical energy storage," *Energy & Environmental Science*, vol. 7, pp. 1597–1614, 2014.

[88] N. Padmanathan, H. Shao, D. McNulty, C. O'Dwyer, and K. M. Razeeb, "Hierarchical NiO–In_2O_3microflower (3D)/ nanorod (1D) hetero-architecture as a supercapattery electrode with excellent cyclic stability," *Journal of Materials Chemistry A*, vol. 4, pp. 4820–4830, 2016.

Chapter 3

Analytical instruments

The current chapter describes the analytical instruments and methods used in this thesis. X-ray diffraction (XRD) was used to analyse the crystal structure of prepared rGO/Bi, Bi_2O_3-GO and rGO/$Bi_2O_2CO_3$ composite materials. Scanning electron microscope (SEM) and transmission electron microscopy (TEM) were used to study the morphology of these samples. Energy dispersive X-ray spectroscopy (EDXS) and selected area electron diffraction (SAED) were performed to confirm the chemical elemental components and crystal structures of prepared samples. Fourier transform infrared (FTIR) spectroscopy and Raman spectroscopy were used to further confirm the chemical composition and molecular structure of these samples. X-ray photoemission spectroscopy (XPS) was used to analysis elemental and chemical states of rGO/Bi and Bi_2O_3-GO. A potentiostat was used to analyse the electrochemical properties, such as cyclic voltammetry, charge/discharge behaviour and cycling performance, of the synthesized compounds. Electrophoretic light scattering (ELS) was used to determine the zeta potential of GO and sodium dodecyl sulfate (SDS) modified GO.

3.1 X-ray diffraction

X-ray diffraction (XRD) can be used to identify the unknown crystal structure of a sample [1]. The positions and intensities of peaks shown in XRD pattern have a one-to-one correspondence to that indexed peaks in the candidate diffraction pattern [1]. Therefore, the XRD results are considered as the ”fingerprint” for crystals in materials [1]. In this work, XRD was used to characterize the crystal structures of GO, rGO/Bi, Bi_2O_3-GO and rGO/$Bi_2O_2CO_3$.

Diffraction occurs when waves, which are defined as the distance between peaks by the wave-

length, scatter from an object constructively interfere with each other [2]. Bragg first described the diffraction of X-rays generated by constructive interference from the planes in a crystal by the following equation 3.1 [3]:

$$2dsin\theta = n\lambda \tag{3.1}$$

where d is the interplaner spacing, θ is the incident angle of X-rays, λ is the wavelength of X-rays and n is an integer.

When parallel X-ray beams incident on the lattice planes of a crystal material with an angle of θ, diffraction happens with the same angle (as in Figure 3.1) [2]. Constructive interference occurs only when the two waves are in phase [2]. Therefore the extra distance (AB+BC) should be an integer number of the wavelength λ [2].

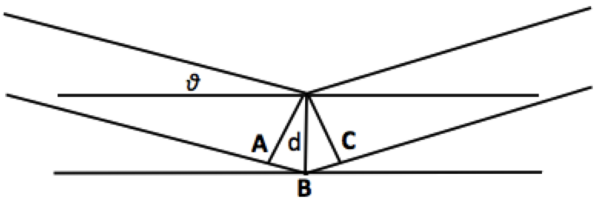

Figure 3.1: Diffraction of X-rays from the planes in a crystal [2].

3.1.1 Instrument

A typical diffractometer, which is used to record the powder patterns electronically, is shown in Figure 3.2 [2]. The diffractometer contains an X-ray tube, a sample table, and a detector. To meet the condition of the Bragg's law, the sample is moved through an angle of θ while the detector is scanned through an angle of 2θ [2].

The XRD measurements in this project were carried out at room temperature with an Altima III, Rint 2000 from Rigaku Company in NIMS, Japan. In this XRD instrument, Cu-K_α with a wavelength of 1.5418 Å was used as the radiation source. During the X-ray diffraction test, an incident X-ray wave is directed to the material while a detector is moved to record the direction and intensity of the outgoing diffractive wave [1]. The data were collected with a range from 0° to 90° 2θ at a step size of 0.02°.

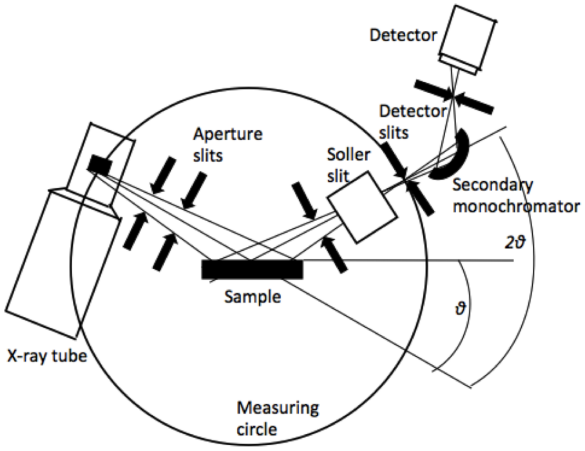

Figure 3.2: A typical diffractometer [2].

3.1.2 Data interpretation

A typical XRD pattern is described in terms of the following components: (1) peak position, (2) peak intensity, (3) peak width and (4) peak shape [4].

(1) Peak position

Peak position (2θ) and the Miller indices (h, k, l) in XRD patterns are used to determine the interplanar distance (d) of a crystal system [5]. Peak position may be shifted due to the instrumental factors, like temperature [4]. The interplanar distance of materials with different crystal lattice systems can be calculated following the Table 3.1, in which a, b, c are the crystallographic axes and α, β, γ are the angles between them [5].

Table 3.1: Interplanar spacing [2, 5].

lattice system	lattice parameters	interplanar distance $\frac{1}{d^2}$
cubic	a=b=c, α=β=γ=90°	$\frac{h^2+k^2+l^2}{a^2}$
tetragonal	a=b≠c, α=β=γ=90°	$\frac{h^2+k^2}{a^2}+\frac{l^2}{c^2}$
hexagonal	a=b≠c, α=β=90°, γ=120°	$\frac{3}{4}\frac{h^2+hk+k^2}{a^2}+\frac{l^2}{c^2}$
orthorhombic	a≠b≠c, α=β=γ=90°	$\frac{h^2}{a^2}+\frac{k^2}{b^2}+\frac{l^2}{c^2}$
monoclinic	a≠b≠c, α=γ=90°, β ≠90°	$\frac{h^2}{a^2sin^2\beta}+\frac{k^2}{b^2}+\frac{l^2}{c^2sin^2\beta}+\frac{2hlcos\beta}{acsin^2\beta}$
triclinic	a≠b≠c, $\alpha\neq\beta\neq\gamma\neq$90°	$[\frac{h^2}{a^2sin^2\alpha}+\frac{2kl(cos\beta cos\gamma-cos\alpha)}{bc}+\frac{l^2}{c^2sin^2\gamma}+\frac{2hl(cos\alpha cos\gamma-cos\beta)}{ac}+\frac{k^2}{b^2sin^2\beta}+\frac{2hk(cos\alpha cos\beta-cos\gamma)}{ab}]\frac{1}{(1-cos^2\alpha-cos^2\beta-cos^2\gamma+2cos\alpha cos\beta cos\gamma)}$

(2) Peak intensity

The intensity of a diffraction peak is controlled by both the diffractometer and the sample itself [1]. For example, with the temperature increased, the thermal vibration effect of atoms become obvious and therefore a reduction in the intensity of diffracted X-rays from a crystal sample can be detected [3]. In addition, if the material exhibits a "preferred orientation", the relative intensity of that peak in XRD pattern will deviate from the intrinsic intensity [4].

(3) Peak width

Crystallite size can be estimated from the peak width by the Scherrer equation (3.2) as following [6]:

$$B(2\theta) = \frac{K\lambda}{L\,cos\theta} \tag{3.2}$$

where $B(2\theta)$ is the mean size of the crystallites, K is a dimensionless shape factor, 0.9, λ is the X-ray wavelength, L is the width at FWHM (full width at half its maximum intensity) and θ is the Bragg angle.

(4) Peak shape

The diffraction pattern gives information of the real space periodicities in a material [1]. Materials with long repeat atomic periodicities have small diffraction angle while materials with short repeat atomic periodicities have large diffraction angles [1]. Therefore, crystals with precise periodicities over a long distance have sharp and clear diffraction peaks in XRD patterns while crystals with defects, which have short repeat periodicities, show broadened and weakened peaks [1].

3.1.3 XRD characterization of rGO and bismuth

In the XRD pattern of graphite, a sharp peak is expected at 26.7°, which corresponds to the (002) crystal plane of carbon. After treated by mixed strong acid and potassium permanganate, oxygen groups attach to the graphite layer and form graphene oxide. The peak in XRD pattern of graphene oxide is shifted to around 12° [7]. The peak has a broadened and weakended shape compared to the graphite peak because the attached oxygen groups destroy the long range atomic periodicity. The internal distance of carbon layers in graphene oxide can be determined from the peak position based on the Bragg's equation. Reduced graphene oxide (rGO) can be obtained after treating graphene oxide with reducing agents, such as hydrazine, in order to remove the oxygen functional groups. Ideally rGO will not show any peak in its

XRD pattern because it is a single carbon layer. However, in practical, rGO normally shows a small hump at around 25° [8]. This broad and weak peak is formed by the disordered stacking of rGO layers.

In the XRD pattern of metallic bismuth, the strongest three peaks appear at 27.60°, 37.80° and 39.46°, which correspond to the (012), (104) and (110) crystal planes of bismuth, respectively (Natl. Bur. Stand. (U.S.)). Bismuth oxide normally has a monoclinic phase at low temperature. In the XRD pattern of monoclinic α-Bi_2O_3, the strongest three peaks appear at 27.27°, 32.92° and 33.12°, which correspond to the (120), (121) and (200) crystal planes of bismuth oxide, respectively (Natl. Bur. Stand. (U.S.). In the XRD pattern of bismuth subcarbonate, strong peaks appear at 23.90°, 26.03°, 30.24° and 32.69°, which correspond to the (101), (004), (103) and (110) crystal planes, respectively (Natl. Bur. Stand. (U.S.).

3.2 Scanning electron microscope

In a scanning electron microscope (SEM), an incoming (primary) electron beam supplies energy to electrons in a solid material and then releases secondary electrons with lower kinetic energies [9]. These secondary electrons are collected and provide a secondary-electron image of that solid material [9]. In this work, a SEM was used to study the morphology of prepared GO, rGO/Bi, Bi_2O_3-GO, rGO/$Bi_2O_2CO_3$ and GO-SDS materials (in chapters 4, 5, 6 and 7).

3.2.1 Instrument

A SEM can be divided into three components: an electron optical system, a sample stage, and detectors as in Figure 3.3 [9].

The electron optical system contains an electron gun, two condenser lenses, and an objective lens. Electron source is located at the top of column. Electrons are generated by field emission from a filament and accelerated toward an anode. Condenser lenses are used to focus the beam by reducing the magnification of the electron beam crossover diameter [9]. By adjusting the size of apertures, an electron beam with desired spot size is obtained. Objective lens is used for a further focusing of the electron beam [9]. Stigmator or astigmator corrector located in the objective lens is used to reduce the aberrations of the electron beam. A sample stage is located at the lower portion of the column. This sample stage is used to support the sample and help it moves smoothly. The SEM instrument used in this project is a type JSM-7001F

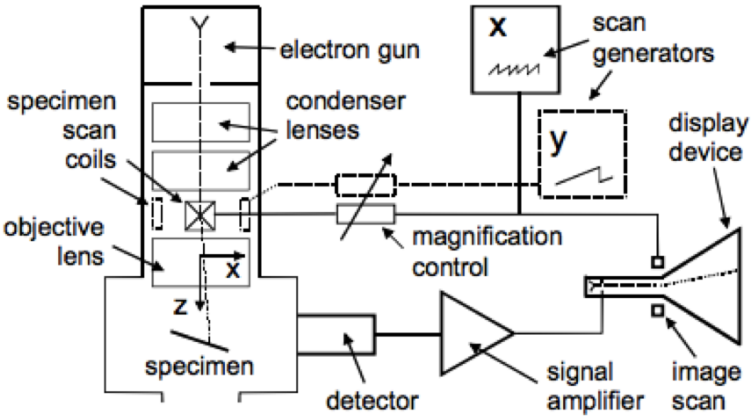

Figure 3.3: Schematic diagram of SEM [9].

from JEOL Company at NIMS, Japan. A field emission gun (tungsten) is used as the electron source. This instrument provides a magnification up to 1,000,000x and a resolution of 1.2 nm.

3.2.2 Principles of the operation

A focused beam of high energy electrons (15 keV) incidents to the sample and generates a various signal due to the electron-specimen interactions [10]. These signals include secondary electrons, backscattered electrons, diffraction backscattered electrons, high energy photons and visible light [11]. All these provide detailed information including morphology, chemical composition, crystalline structure, and orientation of the sample [11]. Secondary electrons are resulted from the inelastic collisions and scattering of incident electrons (primary electrons) by the crystal lattice of atoms. These secondary electrons are collected and amplified by a detector to reveal the surface structure of the tested sample [9]. In addition, there are small fraction of the primary electrons which are elastically backscattered with a diffraction angle larger than 90° [9]. These backscattered electrons contain high kinetic energy which can be collected after re-entering the surrounding vacuum and are used to determine the atomic number mapping [9].

3.3 Transmission electron microscope

In a transmission electron microscope (TEM), high energy electrons, generally between 60-300 keV, with short wavelength are generated by raising the accelerating potential [9]. This electron beam can penetrate a distance of up to several microns (μm) into a solid material and

can be imaged by electrostatic lenses [9]. In this work, TEM was used to characterize the morphology of GO, rGO/ Bi, Bi_2O_3-GO and rGO/$Bi_2O_2CO_3$ (see chapters 4, 5, 6 and 7).

3.3.1 Instrument

Generally, a TEM can be divided into three components: an illumination system, an objective lens/stage and an imaging system, as shown in Figure 3.4 [12].

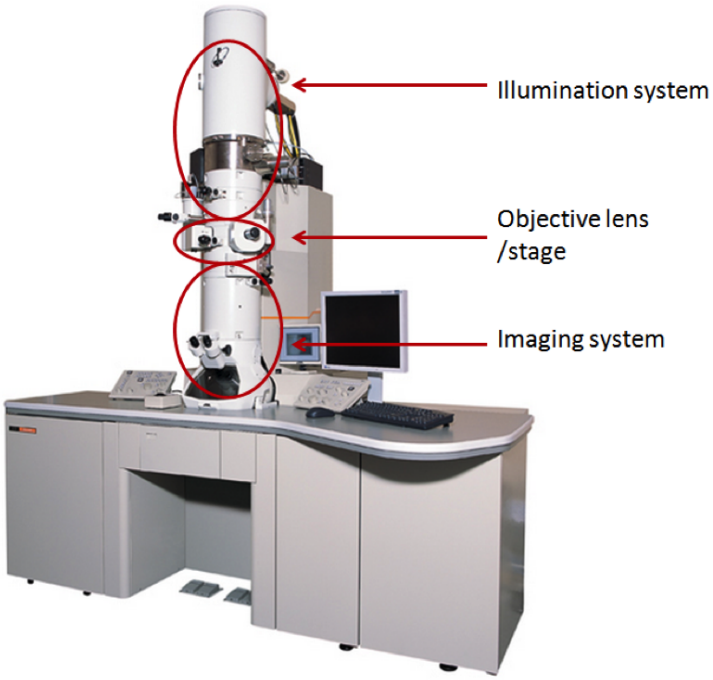

Figure 3.4: Transmission electron microscope [12].

The illumination system contains an electron gun and a condenser lens [12]. By adjusting the current of condenser lens, electrons from the electron gun will be transferred onto the specimen as a parallel beam [12]. The specimen stage is used to move the sample holder to a desired position and orientation [12]. The electrons that are emerged from the surface of the sample are collected by an objective lens to create a diffraction pattern on the back focal plane and produce an image on the image plane [12]. The imaging system contains an intermediate lens, a projector lens and a viewing screen [12]. By change of the strength of the intermediate lens, diffraction pattern or image will be magnified by the projector lens and displayed on the viewing screen [12].

The JEM-2100F Electron Microscope from JEOL Company (Figure 3.4) at NIMS, Japan was used in this project. ZrO/W field emission gun was used under an accelerating voltage of 200 keV. This instrument has a point resolution of 0.19 nm.

3.3.2 Imaging in TEM

In TEM, three types of imaging contrast can be obtained based on the different formation mechanisms of contrast: mass thickness contrast, diffraction contrast and phase contrast [1, 12, 13].

Mass thickness contrast

Mass-thickness contrast results from the elastically scattered electrons [12]. When the electrons pass through samples, they are scattered off axis with small angles due to the elastic interaction with nucleus [12]. Samples with a high mass-thickness have more incident electrons elastically scattered off axis, and therefore less electrons are focused on the image plane thus show a darker brightness [12]. Either decreasing the accelerating voltage or using an objective aperture on the back focal plane can enhance this mass-thickness contrast [13].

Diffraction contrast

Diffraction contrast can be used to identify the crystallites in samples [13]. If the angle between incident electrons and crystal lattices of grains fulfill the Braggs law, high intensity of the elastically scattered electrons is achieved [13]. These elastically scattered electrons will be removed by the objective aperture on the back focal plane (Figure 3.5) [13]. Therefore as less electrons fall on the image plane, these crystallite parts show a darker brightness [13].

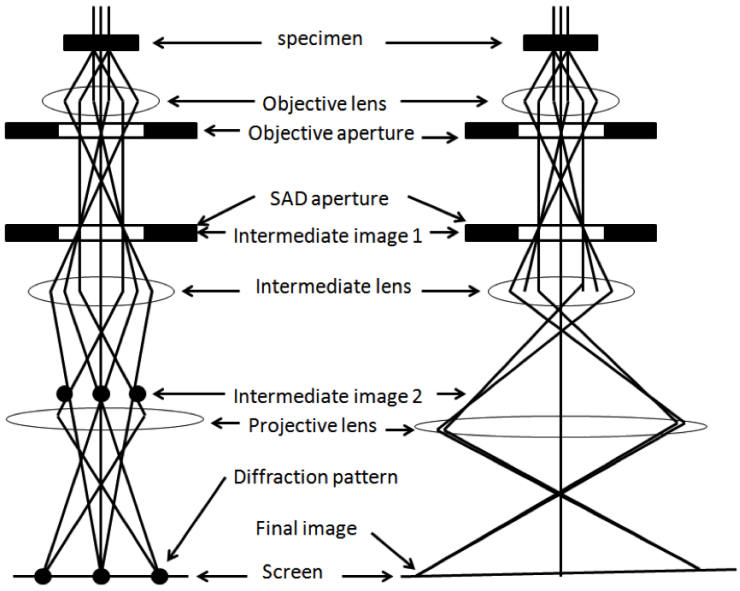

Figure 3.5: Imaging and diffraction in the TEM (schematic diagram) [13].

Phase contrast

Instrument which is designed for phase contrast is usually called HRTEM (high resolution

transmission electron microscopy) [14]. A large objective aperture or no aperture, which allows diffracted wave as well as transmitted beam to pass through the sample, is used to achieve the phase contrast [13]. Spherical aberration corrector is used to reduce the lens aberration to get a clear image. The incident wave is assumed as a plane wave [13]. The wavelength remains the same as electrons pass through the crystal and only results in a phase shift at the sample's exit surface [13]. The transmitted and diffracted electrons with various phase changes, interfere with each other and produce a phase contrast image with atomic resolution [13]. In another word, the phase shift reflects the periodicity of the crystal [13].

3.3.3 Analytical possibilities in TEM

Electron diffraction

Diffraction pattern formed on the back focal plane could help to determine the distance between crystal lattice phase [13]. SAED (selected area electron diffraction) can be used to determine both the single crystal structures and the polycrystalline structures [13]. Crystalline samples have the point diagrams while polycrystalline samples have scattering curves as the pattern of diffraction [13]. Equation 3.3 and Figure 3.6 explain the electron diffraction in TEM [1, 13]:

$$tan\theta = \frac{r}{L} \tag{3.3}$$

where θ is the diffraction angle, r is the distance from central reflection measured on the screen and L is the camera length, the product of the objective focal length and the magnification by projective lenses.

Diffraction can also be explained by the Bragg's law as equation 3.1 [13]

$$2dsin\theta = n\lambda$$

where λ is the wavelength of incident electrons, which can be calculated from the accelerating voltage, d is the distance between lattice planes.

In TEM testing, small diffraction angle ($\theta \ll 1$) is used. Therefore the above two equations 3.3

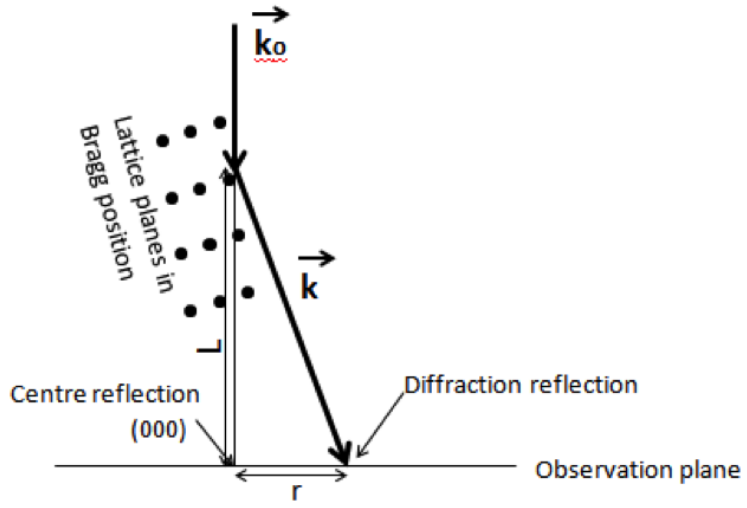

Figure 3.6: Diffraction pattern in TEM [13].

and 3.1 can be combined and written as [13]:

$$\lambda L = dr \tag{3.4}$$

where λL is the apparatus constant.

Energy dispersive spectroscopy of characteristic X-rays (EDXS)

TEM can also be used to determine the chemical elements in the sample. During the inelastic scattering, energetic state of atomic electron shell changes and emits a X-radiation with an energy depending on the atomic number [13]. This X-radiation can be collected and used to detect the element components [13]. Lithium doped silicon crystal is used as the detector [2]. When the X-ray photon enters this crystal, the photon is absorbed and creates a photoelectron whose energy is equals to that of incident X-ray photon minus the binding energy of the electron [2]. Then this energetic photoelectron loses its energy of 3.8 eV and creates an electron [2]. The number of the electrons generated in such way is then counted by the detector [2]. This detector unit is embedded in a polymer window and cooled, including the preamplifier [13]. During the X-ray analysis, this detector is inserted into the pole piece gap of the objective lens [13]. This detector can also be used in a SEM for elemental determination.

3.3.4 SEM and TEM characterization of rGO

Typical SEM and TEM images of graphene oxide and reduced graphene oxide were shown in the figure 3.7 [15]. As in these figures, graphite shows a platelet-like crystalline structure [15].

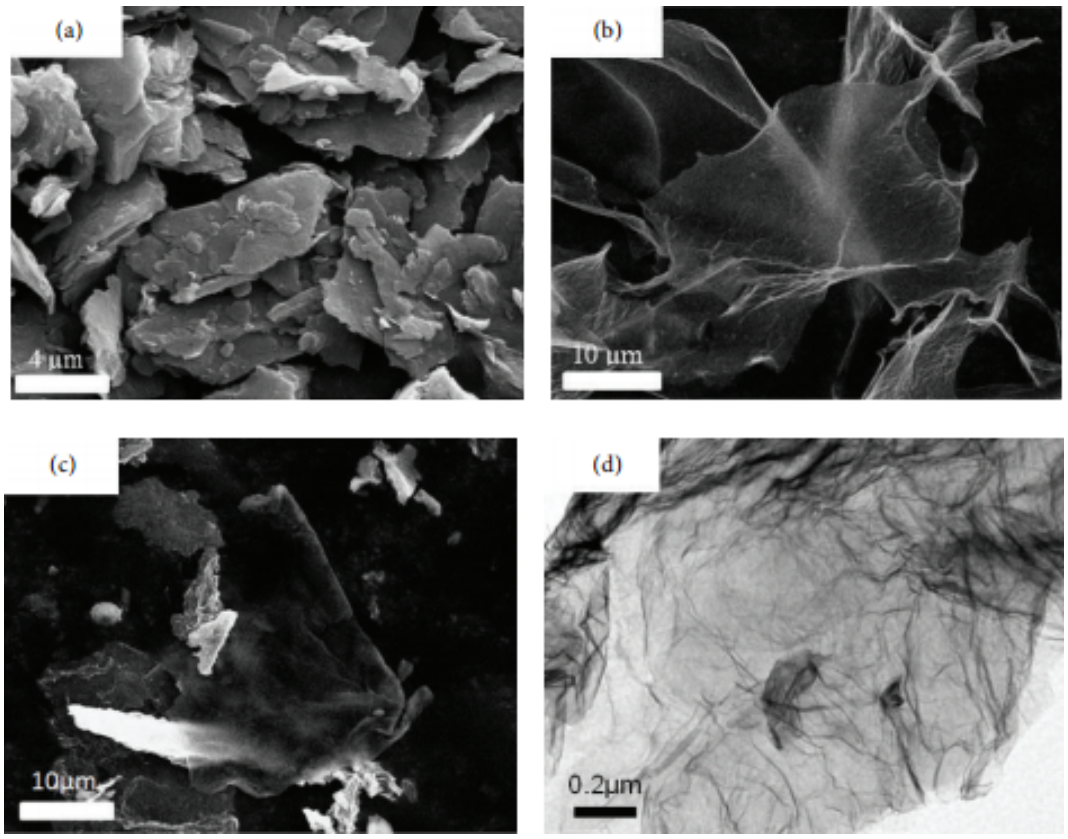

Figure 3.7: SEM and TEM images of GO and rGO. a)SEM image of graphite, b)SEM image of GO, c)SEM image of rGO and d)TEM image of rGO [15].

The graphene oxide sheets are smaller and transparent compared to graphite [15]. Reduced graphene oxide exhibits wrinkled structure which is caused by the sheet folding [15].

3.4 X-ray photoemission spectroscopy (XPS)

XPS is a surface analysis instrument for elemental and chemical state identification. In this work, XPS was used for analysis of the chemical states of bismuth in rGO/Bi sample and the chemical state of carbon in GO, rGO/Bi and Bi_2O_3-GO, as in chapters 4 and 5.

3.4.1 Measurement principles

XPS is a powerful technique which is used to identify and quantify the elemental composition of the outer 10 nm of any solid surface [16]. All elements from Li to U are detectable [16]. A photoelectron process is shown in Figure 3.8 [17]. For example, in the XPS measurement, an X-ray photon of energy *hv* is directed to the sample. A 1s electron in K shell is ejected from the sample and emited as a photoelectrons [17]. The kinetic energy of this emitted photoelec-

tron is measured and used to calculate the binding energy and then determine the elemental and chemical states of the material [17].

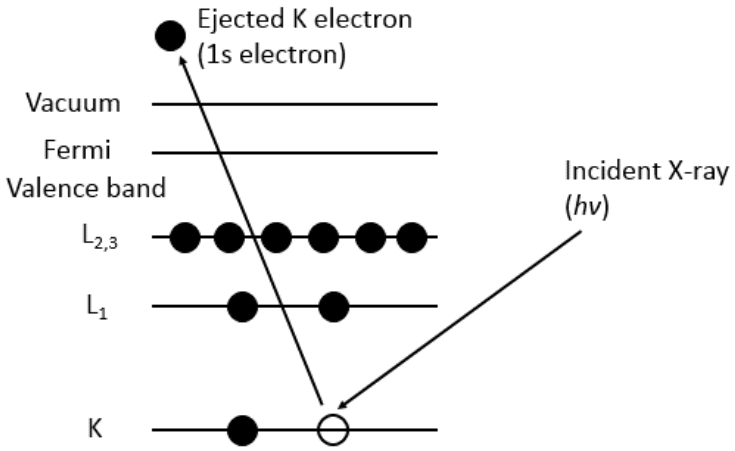

Figure 3.8: A XPS process with photoionization of an atom by the ejection of a 1s electron [17].

The electron binding energy, which is elemental and environment specific, can be determined by the following equation 3.5 [17]:

$$E_B = hv - E_K - W \tag{3.5}$$

Where E_B is the electron binding energy, hv is the photon energy, E_K is the kinetic energy of the electron and W is the spectrometer work function.

3.4.2 Instrument

High vacuum is the pre-requirement for XPS measurement. With an improved vacuum, detection probabilities in XPS can be increased [16]. A XPS instrument consists of three components, a X-rays source, an energy analyser and a detector [16]. X-rays is selected as the incident beam because the source used in XPS must be able to produce photons of sufficient energy to access core electron levels [16]. Photons of this energy lie in the X-ray region of the electromagnetic spectrum [16]. A concentric hemispherical analyser (CHA), as in Figure 3.9, is used to measure the kinetic energy of the ejected electrons [16]. It consists of two concentric hemispheres, one insider the other, with the radius of R_1 and R_2 [17]. After applied a potential difference across these two hemispheres, only the electrons with the following energy (as in equation 3.6) can reach the detector [17].

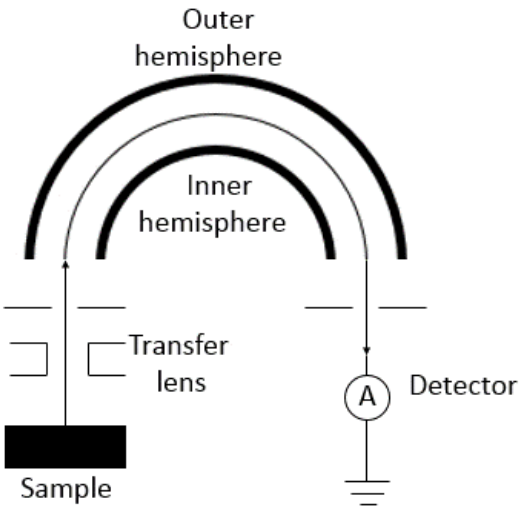

Figure 3.9: A concentric hemispherical analyser used in XPS [16].

$$E = e\Delta V \frac{R_1 R_2}{R_2^2 - R_1^2} \tag{3.6}$$

Where E is the kinetic energy of the electrons, e is the charge on the electron, ΔV is the potential difference between the two hemispheres, R_1 and R_2 are the radius of the inner and outer hemispheres. By change of the potential difference, electrons with different kinetic energies can be selected and detected.

In this work, the XPS spectra were measured with a Kratos Axis Ultra spectrometer, using monochromated Al K_α X-rays (hv=1486.6 eV). Samples were grind into powder for measurement. High resolution XPS data were fitted using UNIFIT2007 and Winspec with a Shirley-type background for secondary electrons.

3.5 Fourier transform infrared (FTIR) spectroscopy

FTIR spectrometer is a powerful technique which provides the information of chemical composition of the sample. The FTIR spectra of rGO/Bi, Bi_2O_3-GO, rGO/$Bi_2O_2CO_3$ and GO-SDS were presented in the chapters 4, 5, 6 and 7, respectively.

3.5.1 Measurement principles

When an infrared radiation (IR) light passes through a sample, the molecules in that sample absorb the infrared radiation and result in their vibration [18]. Functional groups within

molecules absorb the infrared radiation in the same wavenumber range according to the structure of that molecule [18]. Every molecule has a slightly different vibrational modes from all the other molecules and gives an unique infrared spectrum [19]. Therefore the infrared spectrum can be used to identify that molecule. Compared to the traditional infrared spectroscopy, which called dispersive instrument, FTIR spectroscopy allows all the infrared radiation pass through the sample and measure the infrared frequencies at the same time by a detector [18]. This is because Fourier transformation is used in FTIR spectroscopy to transform the measured signal into a final infrared spectrum. The Fourier transform that is used can be expressed as [19]:

$$F(\omega) = \int_{-\infty}^{+\infty} f(x) e^{iwx} dx \tag{3.7}$$

Where $F(\omega)$ is the spectrum, $f(x)$ is the interferogram, ω is the angular frequency and x is the optical path difference.

3.5.2 Instrument

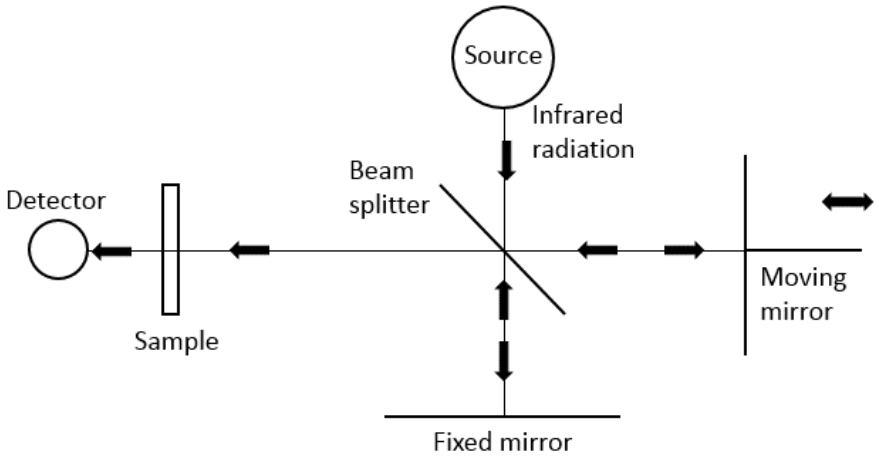

Figure 3.10: An optical diagram of a Michelson interferometer [18].

A typical interferometer used in FTIR is shown in Figure 3.10 [18]. The IR light beam is directed to a beam splitter, from where half of the light is transmitted and the other half is reflected [18]. These two beams of light reach a fixed mirror and a moving mirror and then both reflect back toward the beam splitter [18]. Therefore, the detector catches two beams, one from the fixed mirror and the other one from the moving mirror. These two beams come from the same IR source but have an optical path difference which is determined by the position of the two mirrors [18]. By change the position of the moving mirror for a particular frequency,

the two beams interfere constructively or destructively [18]. After this beam passes through the sample, the transmitted beam with a sinusoidal signal, also called interferogram, is collected by the detector [18]. The IR source contains a wide range of frequencies, therefore the detector output is a sum of all the interferograms. The Fourier transform is then used to transform the interferograms into a spectrum [18].

A Varian 600 IR type FTIR spectrometers in Newcastle University, UK was used in this work. All samples were grind into powder and tested under N_2 environment with a wavenumber range from 4000 cm^{-1} to 400 cm^{-1}. This instrument has a resolution of 2 cm^{-1}. Background spectra were first collected. The spectra of samples are the ratio of the spectrum containing sample against that of the background. 100 scans were collected for each sample.

3.5.3 XPS spectra of rGO and bismuth

In the XPS spectrum, C 1s lines appeared in the binding energy range from 280 eV to 295 eV. The binding energy of graphite (C-C) is located at 284.4 eV binding energy. [20] The binding energy of C 1s components, such as hydrocarbons (C-H), alcohol (C-OH), carbonyl (C=O), ester (COOR) and satellite (π-$\pi^\star$), are located at 285.0 eV, 286.1-286.3 eV, 287.6-287.7 eV, 288.6-289.1 eV and 290.5-290.8 eV, respectively. [20] Graphite has an asymmetric C 1s peak centred at 284.4 eV in the XPS spectrum. In addition, a small peak at 290.5-290.8 eV correspond to the π-$\pi^\star$ transition. In the XPS spectrum of graphene oxide, beside the graphite C 1s peak, more peaks that are in the binding energy range of 285.5-290.8 eV are due to the attached oxygen functional groups. In the XPS spectrum of reduced graphene oxide, the peaks appeared in the C 1s components region should become less dominant compared to these peaks in graphene oxide sample. This is because majority of the oxygen functional groups attached on graphene oxide sheets can be removed by the reducing agents.

Bi 4f peaks appear in the XPS spectrum within the binding energy region, 150-170 eV. Bi 4f has well separated spin-orbit components, of 5.3 eV. Binding energies of Bi 4f peaks for Bi are located at 162.3 eV (4f5/2) and 156.6 eV (4f7/2) [21]. Binding energy of Bi 4f peaks for Bi_2O_3 are located at 161.5 eV (4f5/2) and 158.7 eV (4f7/2). [22]

3.6 Raman spectroscopy

Raman spectroscopy and IR spectroscopy are complementary techniques to study the vibration modes of molecules [23]. Similar to FTIR spectroscopy, Raman spectroscopy is also based on the interaction of the radiation with samples. Different from FTIR spectroscopy, Raman spectroscopy identifies the molecule structure of the sample by measure the frequency shift after radiation scattering. In general, Raman spectroscopy is good at measuring the symmetric vibrations of non-polar groups while IR spectroscopy is good at measuring the asymmetric vibration of polar groups [23]. Raman spectroscopy was used in this work to analyse the reduction from GO to rGO in chapters 4, 5 and 6.

3.6.1 Raman Scattering

A laser with monochromatic radiation is used to irradiate the sample in Raman spectroscopy [23]. The scattering that happened can be divided into three types, Rayleigh scattering, Stoke Raman scattering and anti-Stokes Raman scattering, based on the frequency shift of the incident radiation scattering, as in Figure 3.11 [23, 24].

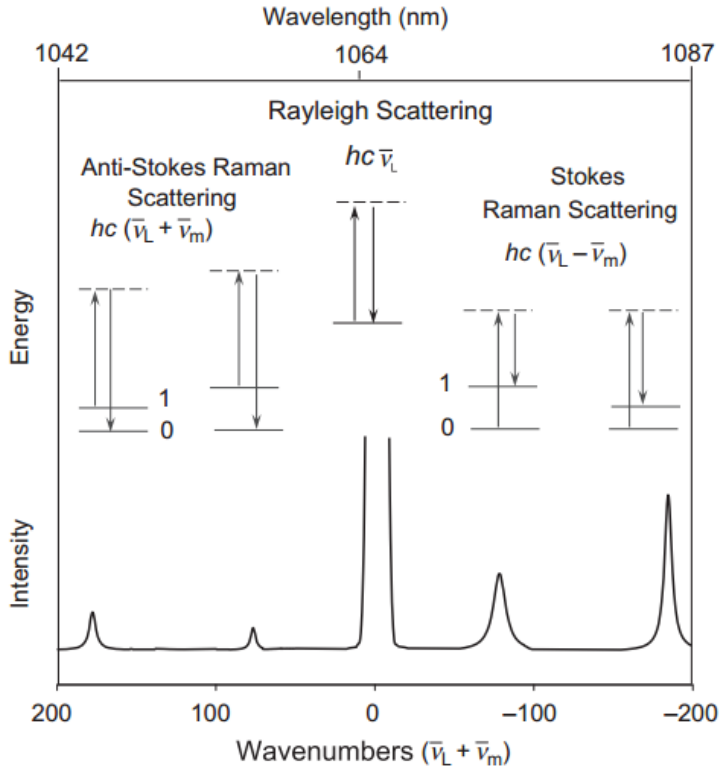

Figure 3.11: Schematic illustration of Rayleigh scattering and Stokes and anti-Stokes Raman scattering [23].

In the Rayleigh scattering, even there is no energy change in the system, this system still par-

ticipates in a scattering process [24]. An incident photon is absorbed momentarily by the transition from the ground state to the virtual state. A photon is then generated by this transition from the virtual state to the ground state resulting in no frequency shift and energy change [23]. The molecules initially in the ground vibrational state give rise to the Stokes Raman scattering while the molecules initially in the excited vibrational state give rise to the anti-Stokes Raman scattering [23].

3.6.2 Instrument

A basic Raman spectroscopic system is shown in the Figure 3.12 [25]. It consists of three components, a light source, a sample light delivery and collection part and a detector [25]. The excitation source is used to provide laser beam. This beam is focused by the objective lens and directed to the sample. Raman scattered light is then collected by the detector and transformed into electrical signals. The Raman spectrum is plotted as the Raman scattered light intensity as the function of frequency shift.

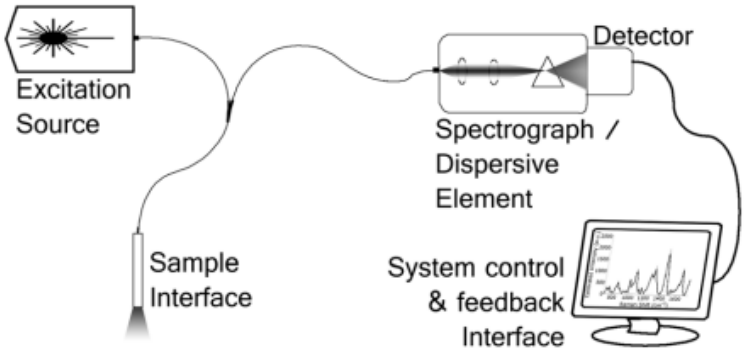

Figure 3.12: A basic schematic of the Raman spectroscopic system [25].

A type HR800UV Raman spectrometer from HORIBA Jobin Yvon company was used in this project. An argon ion laser of strong emission line at 514.5 nm with 10% filter was used as the radiation source. Samples were first grind into powder and then pressed on a silica glass slide for Raman study. An energy range from 1000 cm^{-1} to 1900 cm^{-1} was selected.

3.6.3 Raman spectra of GO and rGO

Previous studies show that graphite, graphene oxide and reduced graphene oxide have peaks in the wavenumber range from 1000 to 1900 cm^{-1} [26]. The two main peaks in the Raman spectra of carbon materials are located at 1560 cm^{-1} (G band) and 1360 cm^{-1} (D band) [26].

The G band is caused by the in-phase vibration of the sp^2 graphite lattice [27]. The D band is caused by the structural defects and disorder in graphite lattice [27]. A typical Raman spectra of carbon materials, including graphite, graphene oxide and graphene, are shown in the figure 3.13 [28]. Graphite shows a strong peak at 1575 cm^{-1} due to the in-phase vibration of graphite

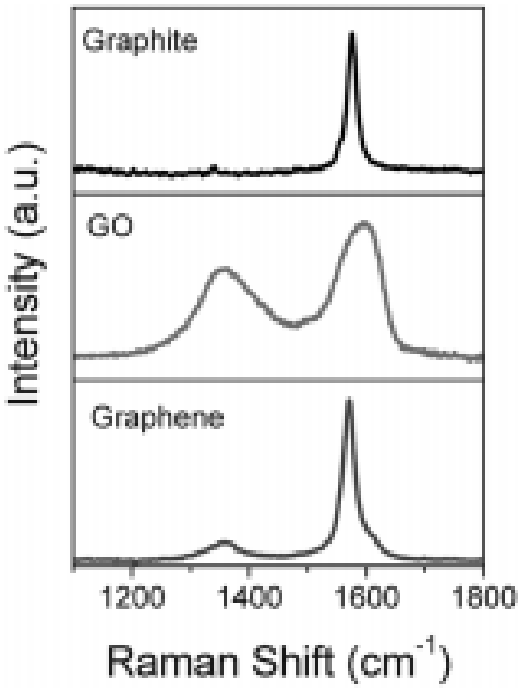

Figure 3.13: Raman spectra of carbon materials, including graphite, graphene oxide and graphene [28].

lattice [28]. In the spectrum of graphene oxide, the G band becomes broaden and exhibits a blue shift to 1594 cm^{-1} [28]. A D band peak appears at 1354 cm^{-1} [28]. Graphene shows a strong G band in Raman spectrum, which has the similar position as G band of graphite. Graphene also has a low intensity D band because of the remained oxygen functional groups.

3.7 Electrochemical analyser

A potentiostat is an electronic instrument which can be used to measure the current flow between the working electrode and the counter electrode while controlling the voltage difference between the working electrode and the reference electrode. The electrochemical properties, such as cyclic voltammetry, charge/discharge behaviours and cycling performance, of rGO/Bi, Bi_2O_3-GO and rGO/$Bi_2O_2CO_3$ were tested and analysed by potentiostat in chapters 4, 5 and 6.

3.7.1 Instrumentation

Potentiostat is used to perform analytical studies in electrochemistry field [14]. Figure 3.14 is a typical schematic diagram of a three electrode potentiostat [29]. This potentiostat contains a three electrodes system, operational amplifiers and feedback loops [29]. To reduce the effect of the ohmic potential drop, the reference electrode (RE) and the working electrode (WE) should be placed as near as possible [29, 30]. Since no current flows through the reference electrode and its position is close to the working electrode, the potential drop caused by the cell resistance is minimized [29]. In addition, to minimize the current generated by the instrument, an operational amplifier is used [14].

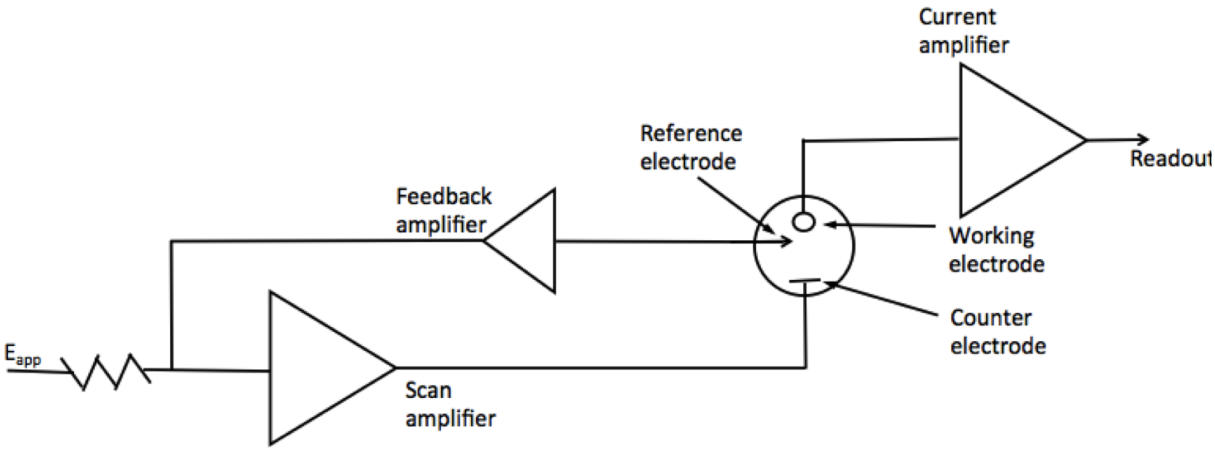

Figure 3.14: Schematic diagram of a three electrode potentiostat [29].

In this work, a VSP-300 multichannel potentiostat from the BioLogic Science Instruments was used. This potentiostat has a potential resolution of 1 μV and a current resolution of 760 fA.

3.7.2 Electrochemical cells

An electrochemical cell is used for the electrochemical properties test. It consists of three electrodes, an electrolyte and a container (Figure 3.15) [31]. Three electrodes that are used are: a working electrode (WE) which defines the interface under study, a reference electrode (RE) which maintains a constant reference potential, and a counter electrode (CE) which supplies the current [31].

Reference electrode

Reference electrode is used to determine the electrode potential in a half cell measurement because it is difficult to compare an unknown system (working electrode) with a known, standard

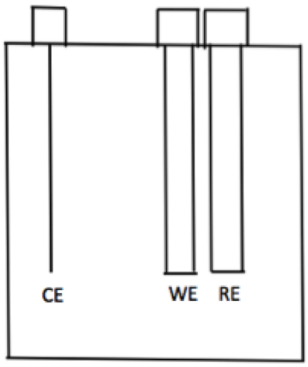

Figure 3.15: Electrochemical cell of a three electrodes system, CE (counter electrode), WE (working electrode), and RE (reference electrode) [31].

system directly [32]. However, no standard electrode can be set up experimentally because the standard state of an electrode is a hypothetical concept [32]. Therefore, all reference electrode used practically should be converted into a standard hydrogen electrode (SHE), in which the potential is taken as zero at all temperatures [32]. The standard hydrogen electrode requires an ideal hydrogen gas at 1 atm pressure and the reaction can be written as equation 3.8 [32]:

$$H_{2(aq.soln.)} \Leftrightarrow 2H_{(adsorbedonmetal)} \Leftrightarrow 2H^{+}_{aq.soln.} + 2e^{-} \tag{3.8}$$

However, the requirement of the continuously control of the H_2 pressure is difficult to achieve.

Saturated calomel electrode (SCE) and mercury-mercury oxide electrode (HgO|Hg), which have stable potential values, were used as the reference electrodes in electrochemical tests in this work.

SCE vs. SHE

SCE is a half-cells electrode based on the charge transfer reactions between mercury-mercury chlorides in a saturated potassium chloride solution [33]. Because saturated KCl was used, the electrode reaction only involves species at the unit activity (Hg_2Cl_2 and Hg) while the amount of Cl^{-} ions remain constant [34]. The reaction happens in SCE can be described as in equation 3.9 [34]:

$$Hg_2Cl_{(2s)} + e^{-} \Leftrightarrow Hg_{(l)} + Cl^{-}_{(aq)} \tag{3.9}$$

The standard potential of a half-cell SCE at 25°C has been accurately measured as [33]:

$$E_{SCE} = E_{SHE} + 0.241V \tag{3.10}$$

HgO|Hg vs. SHE

The HgO|Hg reference electrode involves the reaction between HgO and Hg as:

$$HgO_{(s)} + H_2O + 2e\text{-} \Leftrightarrow Hg_{(l)} + 2OH\text{-} \tag{3.11}$$

When HgO|Hg is used as the reference electrode in an alkaline electrolyte, the potential of a standard half-cell at 25°C is 0.098V vs. SHE [35, 36]. When the concentration of the electrolyte solution is considered, the potential of the HgO|Hg electrode can be expressed by the Nernst equation as following [37]:

$$E = 0.0984 - \frac{RT}{zF} ln\alpha_{(OH)\text{-}} \tag{3.12}$$

where E is the potential value of HgO|Hg electrode at a certain concentration of alkaline solution, R is the gas constant, 8.314 JK^{-1} mol^{-1}, T is the absolute temperature, 298.15 K, F is the Faraday constant, 9.648×10^4 C mol^{-1}, z is the number of moles of electrodes transferred in the half-cell reaction, and $\alpha_{(OH)\text{-}}$ is the activity of hydroxide ions in solution, which can be estimated by:

$$\alpha_{(OH)\text{-}} = \gamma m \tag{3.13}$$

where γ is the mean activity coefficient of the hydroxide ion and m is the solution concentration in molarity. When the molarity (m) of electrolyte solution is 6 mol L^{-1}, the mean activity coefficient, γ, of KOH is 2.18 [36, 38]. Therefore the potential value of HgO|Hg electrode can be calculated as

$$E = 0.0984 - 0.059 \times lg(6 \times 2.18) = 0.0325V \tag{3.14}$$

The potential different between HgO|Hg and SHE can then be written as:

$$E_{HgO|Hg} = E_{SHE} + 0.0325V \tag{3.15}$$

Counter electrode

A counter electrode is made of conducting and usually inert materials [30]. The surface area of the counter electrode should be larger than the surface area of the working electrode [30]. In this work, a Pt wire was selected and used as the counter electrode.

Working electrode

For rGO/bismuth compound composite materials, a mixture which contains 90 wt% of the prepared samples and 10 wt% of the PTFE was used as the working electrode. The added PTFE was used as the bonding agent. Nickel foam was used as the electron collector. Two pieces of nickel foam (1cm×3cm and 1cm×1cm) were first cut and washed by ethanol in a sonication bath. These nickel foams were dried in the vacuum at 60°C overnight (more than 12 hours). The weight of these nickel foam was measured. After dropping the prepared slurry onto one side of the nickel foam, this nickel foam was dried again in the vacuum at 60°C overnight. The weight change of this nickel foam is the weight of the attached active material with PTFE.

3.7.3 Technique used in electrochemical test

Cyclic voltammetry (CV)

Cyclic voltammetry is the widely used technique to study the electrochemical properties of a material in solution [29]. Its results give considerable information on the thermodynamics of the redox process of a chemical reaction or an adsorption process [29]. During the CV test, the electrode potential is changed linearly with the time within a settled voltage range, which can be expressed by the scan rate ($V\ s^{-1}$). During the potential changes, the potentiostat measures current changes resulting from the applied voltage [29]. In the cyclic voltammogram, results are plotted as the applied potential (V) vs. the current (I) [39]. The potential is measured between the working electrode and the reference electrode while the current is measured between the working electrode and the counter electrode. Figure 3.16 shows a typical cyclic voltammogram of the graphene and the graphene/bismuth oxide composite material [40].

Graphene exhibits a rectangular cyclic voltammogram shape while graphene/bismuth oxide composite shows obvious peaks in its cyclic voltammetry results. The capacitance obtained by graphene is due to the adsorption and desorption of the electrons solely. In the cyclic voltammogram of graphene/Bi_2O_3 composite material, the peak that appeared at around the -0.68 V is result from the reduction reaction from Bi^{3+} to $Bi^{(0)}$ [40]. The two oxidation peaks at -0.5 V and -0.3 V are attributed to the formation of Bi^{3+} from $Bi^{(0)}$ during the oxidation reaction [40].

Chronopotentiometry

Chronopotentiometry is used to study the charge/discharge behaviours of materials. During

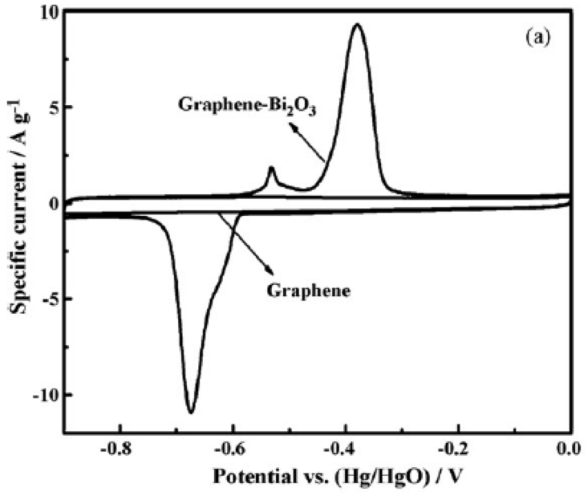

Figure 3.16: Typical cyclic voltammogram of graphene and graphene/bismuth oxide composite materials [40].

the chronopotentiometry test, the working electrode is tested between an applied potential at a constant current density. This charge/ discharge test can also be repeated and used to analyse the stability of the working electrode.

The typical curves of charge/discharge behaviours of rGO and Bi_2O_3 are shown in Figure 3.17 [40, 41]. In the chronopotentiometry curves of rGO/Bi_2O_3, a plateau that appeared at around -0.4V in the charging process is due to the oxidation reaction of bismuth, which correspond to the cyclic voltammetry results [40, 41]. The discharge process contains a slope and a plateau. The slope is contributed by the electric double layer capacitance while the plateau is due to the reduction reaction of bismuth from +3 oxidation state to $Bi^{(0)}$ [40]. For graphene electrode, the discharge duration is attributed solely to the electric double layer capacitance [40]. Compared to graphene, graphene/Bi_2O_3 has longer discharge duration time due to the contribution of both the electric double layer capacitance and Faradaic reactions [40].

The specific capacitance of active materials deposited on the working electrode can be evaluated from the following equation 3.16 [39], which is used to describe the pure capacitor behaviour with rectangular CV curve and triangular charge discharge curve:

$$C = \frac{i \times \Delta t}{\Delta V \times m} \tag{3.16}$$

where, C is the specific capacitance (F g^{-1}), i is the current (mA), Δt is the discharging time (s), ΔV is the potential (V) and m is the mass of active materials (mg).

Specific capacity, as in following equation 3.17, is suggested to be used to describe the electrochemical properties from Faradaic reactions, which have redox peaks in a cyclic voltamme-

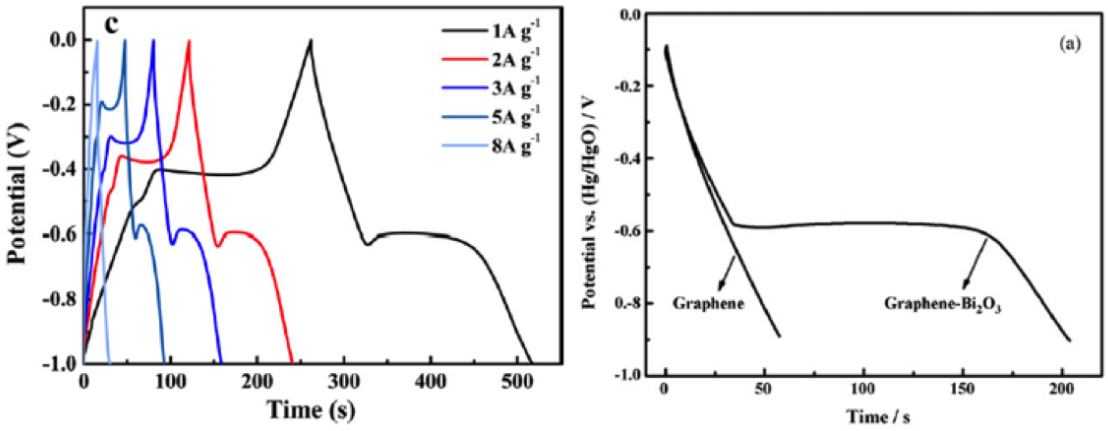

Figure 3.17: a) Typical charge/discharge curves of a graphene/bismuth oxide composite material [40] b) Typical discharge curves of graphene and graphene /bismuth oxide composite materials [41].

try curve and the plateau in a charge discharge curve [42, 43]:

$$C_s = \frac{i \times \Delta t}{m} \tag{3.17}$$

where, C_s is the specific capacity (C g^{-1}), i is the current (mA), Δt is the discharging time (s) and m is the mass of active materials (mg).

3.8 Electrophoretic light scattering (ELS)

During the electrophoretic light scattering, the particle motion caused by an applied oscillating electric filed resulted in a frequency shift of the incident laser beam. The electrophoretic mobility determined by the frequency shift is then used to calculate the zeta potential of materials. The zeta potential of GO and sodium dodecyl sulphate (SDS) decorated GO were estimated by ELS in chapter 7.

3.8.1 Zeta potential

Zeta potential is a parameter which is used to describe the surface charge of a material placed in a liquid. It is generally used to predict the stability of the dispersion. Zeta potential cannot be measured directly, but it can be determined by the electrokinetic effects, such as electrophoresis and electro-osmosis [44]. Electrophoresis, which has been used to determine the zeta potential by ELS, is the movement of a charged particles in a liquid under an external

electric field [45]. The electro-osmosis is the movement of a liquid through immobilized set of particles under an external electric field [45].

Zeta potential is defined as the potential at the slip plane of a particle in electrolyte as in Figure 3.18 [45]. The region between the particle surface and the inner Helmholz plane (IHP)

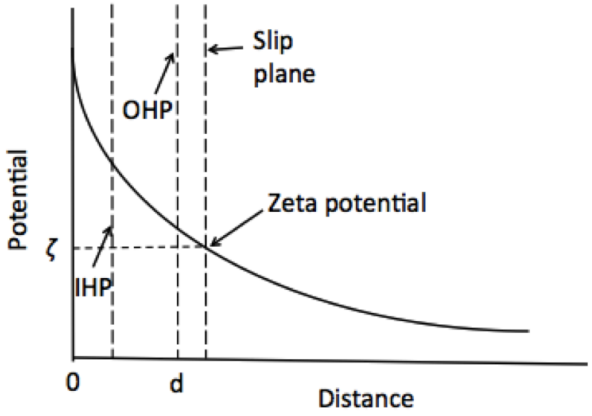

Figure 3.18: Schematic of the charges and potentials at a positively charged interface. IHP (inner Helmholtz plane), OHP (outer Helmholtz plane) and slip plane from a charged particle [45].

is called inner Helmholz layer [45]. This layer of the solvent is assumed to be fixed with the particles and free of charge [44, 45]. The layer located between IHP and OHP is called outer Helmholtz layer [45]. In this layer, unlike ions adsorbed on the particle surface in inner Helmholz layer, ions interact with the surface charge through electrostatic forces [45]. Ions beyond the outer Helmholtz plane to slip plane form the diffuse layer [45]. The slip plane marks the region from where liquid first begin to move with respect to the particles [44]. The electrostatic potential in this slip plane relative to the potential in solution is defined as zeta potential [44].

3.8.2 Measurement principles

Electrophoretic light scattering (ELS), based on an electrophoresis principle, was used in this work to estimate the zeta potential of GO samples [45]. Graphene oxide flakes were larger than 1 μm, which is much larger than the double layer thickness. Therefore the Smoluchowski equation is the suitable equation to be used to estimate the zeta potential of GO [46, 47]:

$$u_E = \frac{\varepsilon \zeta}{\eta} \tag{3.18}$$

where u_E is the particle mobility, ε is the dielectric constant of the dispersion medium, ζ is the zeta potential and η is the dynamic viscosity of the dispersion medium (Pa s).

3.8.3 Instrument

In this work, a Zetasizer Nano ZS from Malvern was used to estimate the zeta potential of GO and GO-SDS samples within the pH range from 3 to 9. This instrument is able to measure samples of size from 3.8 nm to 100 μm with a sensitivity as high as 10 mg mL^{-1}.

The characterization method used by Malvern Instrument Zetasizer is illustrated in Figure 3.19 [44]. Two coherent beams from the laser, are split by a beam splitter and crossed at the

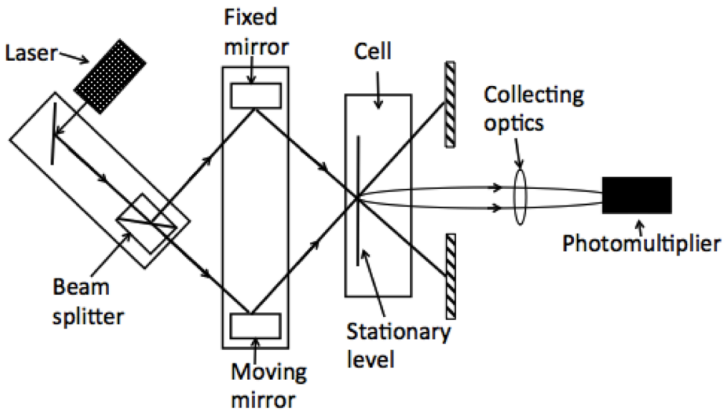

Figure 3.19: Schematic arrangement of the Malvern Zetasizer [44].

stationary level in capillary cell which contains the particle suspension [44]. At this intersection, a pattern of interference fringes is formed [44]. When the particles moves across this pattern under the applied electric field, the scattered light shows similar fluctuations [44]. The frequency of this fluctuation depends on the speed of particles movements [44]. These scattered light is collected by a photomultiplier and analysed and extracted into the zeta potential value [44]. Compared to other techniques, ELS can get measurement with a small amount of sample in few seconds and the results are reproducible [45].

3.8.4 Zeta potential of graphene oxide

During the oxidation process from graphite to graphene oxide, functional groups are introduced to graphene oxide sheets. Graphene oxide sheets have epoxy group on the basal plane and carboxylic groups at the edges [48]. These functional groups weakly develop negative charges in the solution and show a hydrophilic nature [48]. The negatively charged graphene oxide sheets have been proved by zeta potential measurement, as in figure 3.20 [48]. In this figure, zeta potential of graphene oxide synthesised at three different temperatures, 20°C, 27°C and 35°C, were measured in a pH range from 2.5 to 10. [48]. All samples exhibit neg-

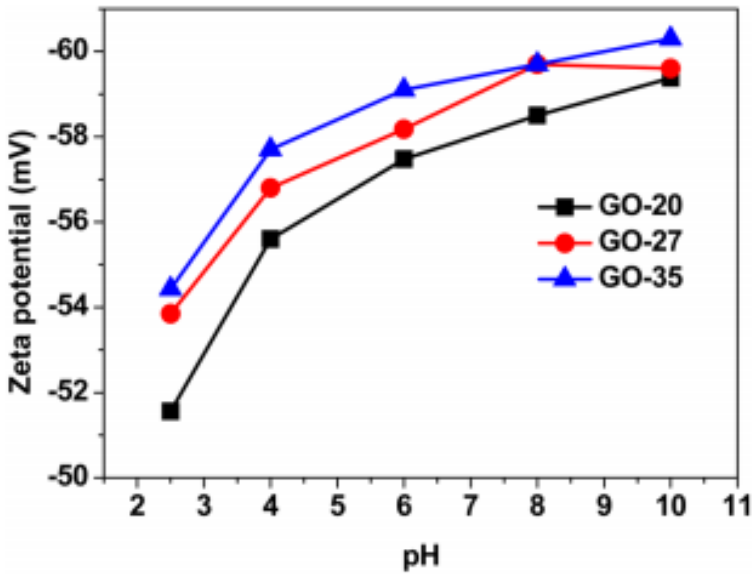

Figure 3.20: Zeta potential of graphene oxide [48].

ative values of zeta potential. With the pH value increased, graphene oxide exhibits a more negative value of Zeta potential.

References

[1] B. Fultz and J. M. Howe, *Transmission electron microscopy and diffractometry of materials 4th ed*. Heidelberg: Springer, 2013.

[2] E. Lifshin, *X-ray characterization of materials*. Weinheim: Wiley VCH, 1999.

[3] Y. Waseda, E. Matsubara, and K. Shinoda, *X-ray diffraction crystallography*. Heidelberg: Springer, 2011.

[4] K. Rissanen, *Advanced X-ray crystallography*. Heidelberg: Springer, 2012.

[5] V. K. Pecharsky and P. Y. Zavalij, *Fundamentals of powder diffraction and structural characterization of materials 2nd ed*. New York: Springer, 2009.

[6] P. Scherrer, "Bestimmung der grosse und der inneren struktur von kolloidteilchen mittels rontgenstrahlen," *Nachrichten von der Gesellschaft der Wissenschaften zu Göttingen, Mathematisch-Physikalische Klasse*, vol. 26, pp. 98–100, 1918.

[7] K. Zhang, Y. Zhang, and S. Wang, "Enhancing thermoelectric properties of organic composites through hierarchical nanostructures," *Scientific Reports*, vol. 3, pp. 3448(1–7), 2013.

[8] K. Zhu, H. Qiu, Y. Zhang, D. Zhang, G. Chen, and Y. Wei, "Synergetic effects of Al^{3+} doping and graphene modification on the electrochemical performance of V_2O_5 cathode materials," *ChemSusChem*, vol. 8, pp. 1017–1025, 2015.

[9] R. F. Egerton, *Physical principles of electron microscopy an introduction to TEM, SEM, and AEM*. New York: Springer, 2005.

[10] W. C. Nixon, "The general principles of scanning electron microscopy," *Philosophical Transactions of the Royal Society of London*, vol. 261, pp. 45–50, 1971.

[11] O. C. Wells, *Scanning electron microscopy*. New York: McGraw-Hill, 1974.

[12] D. B. Williams and C. B. Carter, *Transmission Electron Microscopy, A textbook for materials science*. New York and London: Plenum Press, 1996.

[13] J. Thomas and T. Gemming, *Analytical transmission electron microscopy An introduction for operators*. Dordrecht: Springer, 2014.

[14] C. Lefrou, P. Fabry, and J. Poignet, *Electrochemistry, the basics with examples*. Heidelberg: Springer, 2012.

[15] V. Loryuenyong, K. Totepvimarn, P. Eimburanapravat, W. Boonchompoo and A. Buasri, "Preparation and characterization of reduced graphene oxide sheets via water-based exfoliation and reduction method," *Advances in Materials Science and Engineering*, vol. 2013, pp. 1–5, 2013.

[16] P. van der Heide, *X-ray photoelectron spectroscopy An introduction to principles and practices*. New Jersey: John Wiley & Sons Inc, 2012.

[17] J. F. Watts and J. Wolstenholme, *An introduction to surface analysis by XPS and AES*. New York: John Wiley & Sons Ltd, 2003.

[18] B. C. Smith, *Fundamentals of Fourier transform infrared spectroscopy*. Florida: CRC Press LLC, 1996.

[19] P. R. Griffiths and J. A. D. Haseth, *Fourier transform infrared spectrometry*. New Jersey: A John Wiley & Sons, Inc, 2007.

[20] R. I. R. Blyth, H. Buqa, F. P. Netzer, M. G. Ramsey, J. O. Besenhard, P. Golob and M. Winter, "XPS studies of graphite electrode materials for lithium ion batteries," *Applied Surface Science*, vol. 167, pp. 99–106, 2000.

[21] J. F. McGilp, P. Weightman and E. J. McGuire, "The N6,7O4,5O4,5 auger spectra of

thallium, lead and bismuth," *Journal of Physics C: Solid State Physics*, vol. 10, pp. 3445–3460, 1977.

[22] K. Uchida and A. Ayame, "Dynamic xps measurements on bismuth molybdate surfaces," *Surface Science*, vol. 357, pp. 170–175, 1996.

[23] P. Larkin, *Infrared and Raman spectroscopy Principles and spectral interpretation*. Amsterdam: Elsevier, 2011.

[24] D. A. Long, *Raman spectroscopy*. New York: McGraw-Hill, 1977.

[25] I. Pence and A. Mahadevan-Jansen, "Clinical instrumentation and applications of raman spectroscopy," *Chemical Society Reviews*, vol. 45, pp. 1958–1979, 2016.

[26] A. C. Ferrari, "Raman spectroscopy of graphene and graphite disorder, electron-phonon coupling, doping and nonadiabatic effects," *Solid State Communications*, vol. 143, pp. 47–57, 2007.

[27] K. N. Kudin, B. Ozbas, H. C. Schniepp, and R. K. Prud'homme, "Raman spectra of graphite oxide and functionalized graphene sheets," *Nano Letters*, vol. 8, pp. 36–41, 2008.

[28] H. M. A. Hassan, V. Abdelsayed, A. E. R. S. Khder, K. M. AbouZeid, J. Terner, M. S. Ei-Shall, S. I. Al-Resayes and A. A. Ei-Azhary, "Microwave synthesis of graphene sheets supporting metal nanocrystals in aqueous and orgainc media," *Journal of Materials Chemistry*, vol. 19, pp. 3832–3837, 2009.

[29] J. Wang, *Analytical electrochemistry 3rd ed*. USA: Wiley VCH, 2006.

[30] A. J. Bard, G. Inzelt, and F. S. Cholz, *Electrochemical Dictionary 2nd ed*. Heidelberg: Springer, 2012.

[31] D. Pletcher, R. Greff, R. Peat, L. M. Peter, and J. Robinson, *Instrumental Methods in Electrochemcistry*. Oxford: Woodhead Publishing, 2002.

[32] D. J. G. Ives and G. J. Janz, *Reference Electrode, theory and practice*. New York and London: Academic press, 1961.

[33] J. A. V. Fraunhofer and C. H. Banks, *Potentiostat and its Applications*. London: Butterworths, 1972.

[34] H. B. Oldham and J. C. Myland, *Fundamentals of Electrochemcial Science*. San Diego: Academic Press, 1994.

[35] R. A. Nickell, W. H. Zhu, R. U. Payne, D. R. Cahela, and B. J. Tatarchuk, "Hg|HgO electrode and hydrogen evolution potentials in aqueous sodium hydroxide," *Journal of Power Sources*, vol. 161, pp. 1217–1224, 2006.

[36] B. E. Conway, *Electrochemcial Data*. Amsterdam: Elsevier, 1952.

[37] T. T. Kam, "Some electrochemical studies of mercury mercuric oxide electrode with an inner electrolyte of 33 wt-vol% sodium hydroxide," *Electrochemics Acta*, vol. 27, pp. 553–555, 1992.

[38] W. J. Hamer and Y. C. Wu, "Osmotic coefficients and mean activity coefficients of uni univalent electrolytes in water at 25°C," *Journal of Physical and Chemical Reference Data*, vol. 1, pp. 1047–1100, 1972.

[39] B. E. Conway, *Electrochemical supercapacitors: Scientific fundamentals and technological applications*. New York: Kluwer Academic/Plenum Publisher, 1999.

[40] H. Wang, Z. Hu, Y. Chang, Y. Chen, Z. Lei, Z. Zhang, and Y. Yang, "Facile solvothermal synthesis of a graphene nanosheet–bismuth oxide composite and its electrochemical characteristics," *Electrochimica Acta*, vol. 55, pp. 8971–8980, 2010.

[41] S. Wang, C. Jin, and W. Qian, "Bi_2O_3 with activated carbon composite as a supercapacitor electrode," *Journal of Alloys and Compounds*, vol. 615, pp. 12–17, 2014.

[42] T. Brousse, D. Belanger, and J. W. Long, "To be or not to be pseudocapacitive?" *Journal of Electrochemistry Society*, vol. 162, pp. 5185–5189, 2015.

[43] N. Padmanathan, H. Shao, D. McNulty, C. O'Dwyer, and K. M. Razeeb, "Hierarchical NiO–In_2O_3microflower (3D)/ nanorod (1D) hetero-architecture as a supercapattery electrode with excellent cyclic stability," *Journal of Materials Chemistry A*, vol. 4, pp. 4820–4830, 2016.

[44] R. J. Hunter, *Introduction to Modern Colloid Science*. Oxford: Oxford University Press, 1993.

[45] A. V. Delgado, F. Gonzalez-Caballero, R. J. Hunter, L. K. Koopal, and J. Lyklema, "Measurement and interpretation of electrokinetic phenomena," *Journal of Colloid and Interface Science*, vol. 309, pp. 194–224, 2007.

[46] D. J. Shaw, *Introduction to Colloid and Surface Chemistry 3rd ed.* London: Butterworths, 1980.

[47] R. J. Hunter, *Zeta potential in Colloid Science Principles and Applications*. London: Academic Press, 1981.

[48] D. Kang and H. Shin, “Control of size and physical properties of graphene oxide by changing the oxidation temperature,” *Carbon Letters*, vol. 13, pp. 39–43, 2012.

Chapter 4

Synthesis and characterisation of reduced graphene oxide/bismuth composite for electrodes in electrochemical energy storage devices

4.1 Introduction

The efficient storage of energy is a key challenge in the adoption of renewable energy sources and the deployment of clean power technologies. In recent years supercapacitors have been considered as promising candidates for the next generation of energy storage devices [1, 2]. Compared with batteries, supercapacitors have higher power density and better cycle life [2–5]. However, their low energy density and small potential window limit their applications [6]. It has been suggested that this problem may be addressed by hybrid systems which merge the advantages of supercapacitors and batteries [6], often termed 'supercapatteries'. Such hybrid systems may involve an asymmetric cell structure of a capacitive and a battery electrode [7] or, as reported here, composite electrodes which display elements of both supercapacitive and battery behaviours [8].

There have been a number of previous studies in which composites of carbon and metal oxide have been synthesized and their electrochemical properties analysed [9, 10]. However, few studies have been reported on metal and metal composite materials [11–14]. Ag/C electrodes prepared through a facile hydrothermal method followed by a calcination step achieved a ca-

pacity value of 211 mAh g^{-1} [15], while Ru/mesoporous carbon composites synthesized by a microwave assisted method reached a specific capacitance value of 287 F g^{-1} [12]. Ru/carbon nanocomposites prepared by a polyol process at 170°C have Ru particles attached to the carbon surface [13] and with 60% Ru loading, this composite achieved a specific capacitance of 549 F g^{-1} [13]. Some other metal nanoparticles, such as Au and Ag, have also been considered in electrodes and achieved a capacitance of 70 F g^{-1} [14]. However, the relatively low abundance and high cost of these noble metals limits their commercial applications. With increasing global concern regarding energy saving, environmental protection and CO_2 emissions, the search for a low cost and environmentally friendly material for electrodes in energy storage devices is important.

Bismuth, as one of the post-transition metals, has a stable +3 oxidation state and can also exist at a +5 oxidation state. Its good electrochemical properties and environmentally friendly nature make bismuth an excellent candidate for use in electrode materials [6, 16–19]. Recently, bismuth has been reviewed as one of the most extensively studied elements in solid state physics due to its electronic properties, such as a long Fermi wavelength (around 30 nm [20, 21]) and high Hall coefficient [20]. A particularly attractive feature of bismuth is that, in spite of its heavy metal status, it is considered as a safe and non-toxic material [22]. Moreover, a large amount of bismuth is produced as a by-product of the copper and tin refining industry [22]. All these attributes make bismuth a promising candidate for electrochemical energy storage materials.

In this work, we report on a novel material, a reduced graphene oxide/bismuth composite (rGO/Bi). This composite material was prepared by a modified low temperature polyol process, in which hydrazine was used as the reducing agent [23] while ethylene glycol (EG) was used as both solvent and reducing agent. An intermediate complex is formed by EG and the metal ions absorbed on the rGO surface producing nano-sized particles and preventing aggregation [24, 25]. Bi particles, which are oxidised and reduced during electrochemical cycling, are formed with an approximate lateral size of 20 to 50 nm and attach to the reduced graphene oxide sheets. Assembly of graphene into three-dimensional structures has the potential of creating electrodes with extremely large (and accessible) specific surface areas coupled with good electrical conductivity which enables fast electron transfer [26]. The decoration of such structures with faradaic charge storage materials can create composite electrodes which maximize electrode capacity beyond that offered by the theoretical upper limit of 550 F g^{-1} (550 C g^{-1} at 1 V) in carbon-based materials [26].

Two composite materials, similar to that presented in this work, have been the subject of previous investigation. Wang et al. [27] investigated the electrochemical charge storage behaviour of amorphous carbon-bismuth oxide composites with Bi_2O_3 contents of between $\sim$14% and 33%, which they incorrectly characterize as pseudocapacitive. It is important to differentiate between the specific capacitance and the specific capacity of an electrode [28, 29]. The former refers to the capacitance per unit mass and is only applicable to charge storage that is (pseudo)capacitive in nature – i.e., demonstrates an almost rectangular cyclic voltammagram and linear galvanostatic charge/discharge (GCD) characteristics. Materials displaying non-capacitive faradaic charge storage (battery materials), which possess peaks in cyclic voltammagrams and plateau regions in charge/discharge curves should be characterized in terms of the second quantity, the total charge stored per unit mass. From the GCD data presented by Wang et al. [27] it is possible to derive a specific capacity for their amorphous carbon/Bi_2O_3 composite of $\sim$333 C g^{-1} at 1 A g^{-1}.

The electrochemical behaviour of a reduced graphene oxide bismuth oxide composite containing 23.85 wt% Bi_2O_3 has also been studied [19]. Once more this material was wrongly described as pseudocapacitive, the GCD data showing battery-like behaviour. From the GCD curve presented in that work it is possible to derive a specific capacity for the rGO-Bi_2O_3 composite of 204 C g^{-1} at 1 A g^{-1}. Here we report the structure, composition and electrochemical performance of a rGO-Bi composite with a specific capacity of 460 C g^{-1} at 1.2 A g^{-1}, which is substantially larger than that of the previously reported materials, and reaches 773 C g^{-1} at 0.2 A g^{-1}. We suggest that the improved specific capacity of the composite detailed in this work arises from the excellent electrical conductivity afforded by the rGO backbone, the good electrical contact with the bismuth particles, which are initially deposited in metallic form and a high utilization of bismuth during charge/discharge which is related to the microstructure of the composite.

4.2 Experimental

4.2.1 Chemicals

Natural graphite flake (99.8%) and sulphuric acid (98%) were purchased from VWR. Analytical reagent grade phosphoric acid (85%), potassium permanganate (99.0%), dihydrogen dioxide (50%), bismuth (III) nitrate pentahydrate (>98%), and nitric acid (69%), hydrazine

solution (35 wt%) were purchased from Sigma-Aldrich, as was the anhydrous EG (99.8%). All chemicals were used without further purification.

4.2.2 Materials synthesis

Graphene oxide was prepared by a modified Hummers method [30]. 3 g of graphite and 8 g of $KMnO_4$ were weighed and added into a mixture of 100 mL H_2SO_4 and 20 mL H_3PO_3. This suspension was kept at room temperature for three days with continuous stirring. H_2O_2 was added into this mixture until it turned a bright yellow colour. This mixture was washed and filtered using 5% HCl and followed by DI water (18 MΩ cm^{-1} resistivity) for several times until a pH of 7 was achieved. Graphene oxide was obtained after drying the deposit in an oven at 60°C overnight. 0.3 mmol bismuth nitrate ($Bi(NO_3)_3 \cdot 5H_2O$) and 0.03 g graphene oxide (GO) were dispersed into a mixture of 23 mL ethylene glycol (EG) and 2 mL nitric acid (HNO_3). The suspension was sonicated to reach a homogeneous dispersion. This suspension was transferred into a round bottom flask. 5 mL hydrazine was added into this suspension under vigorous stirring. This reaction was held at 60°C for 3 hours. The synthesized material was collected in a small sample vial after being washed with DI water several times and dried in air overnight. rGO was synthesized by the same approach to act as a control.

4.2.3 Sample characterization

The samples were characterized by X-ray diffraction (XRD, RINT Rigaku), Fourier transform infrared spectroscopy (FTIR, Varian 670-IR), Raman spectroscopy (HR800UV, Horiba, Jobin Yvon), scanning electron microscopy (SEM, XL30 ESEM-FEG, Philips), transmission electron microscopy (TEM, JEM-2100, JEOL), X-ray photoelectron (XPS, Kratos Axis Ultra spectrometer), differential thermal analysis and thermo-gravimetric analysis (DTA and TGA, Setaram Labsys Evo). A potentiostat (Bio-logic Science instruments) was used to analyse the electrochemical behaviour of the composites, via cyclic voltammetry and measurement of the charge/discharge behaviours. Cyclic voltammetry results were used to study the mechanism of the reaction taking place during the Faradaic redox reaction of bismuth. A small amount (9 mg) of sample was dispersed in DI water. PTFE (10 mg mL^{-1}) was added as a binding agent with a sample to PTFE weight ratio of 9:1. After obtaining a homogeneous suspension by sonication, some drops were applied to a nickel foam substrate used as the current collector, working electrode. A three-electrode system was used for the electrochemical properties test.

2.48 mg mixture of rGO/Bi and PTFE pressed on Ni foam was used as working electrode. A HgO|Hg (mercury-mercury oxide) electrode was used as the reference electrode. A Pt wire was used as the counter electrode and a 6M KOH solution was used as the electrolyte. Current densities are quoted in A g^{-1} in this paper as the true surface area of the electrodes is difficult to determine.

Samples for SEM imaging were prepared so that a small amount of a sample was dispersed in absolute ethanol. This mixture was sonicated until a homogeneous suspension was achieved. One drop of the suspension was cast on an SEM sample holder and dried in air

The surface area of the samples was determined from N_2 adsorption isotherms using a Surfer system (Thermo Scientific). The samples were pre-degassed for 4 hours at 10^{-2} Torr before analysis. The surface area was calculated by measuring the amount of adsorbed nitrogen gas in a relative vapour pressure of 0.05 $\sim$0.3 at 77 K by Brunauer–Emmett–Teller analysis.

X-ray photoelectron spectra were measured with a Kratos Axis Ultra spectrometer, using monochromated Al K_α x-rays ($h\nu$ = 1486.6 eV) in normal emission geometry. High resolution XPS data were fitted using UNIFIT2007 [31] employing a Shirley-type background and peaks defined by a convolution between Gaussian-Lorentzian lineshapes, with the exception of the main C1s line, which is fitted with the asymmetric Doniach-*Šunjić* lineshape characteristic of graphitic materials [32]. It was not possible to determine a unique value for asymmetry parameter of the Doniach-*Šunjić* line and hence a value of 0.14, consistent with other nanostructured graphitic carbons, was chosen [33, 34]. However, similar results were obtained using asymmetries characteristic of bulk graphite [32]. The accuracy of resulting fits was attested to by reduced χ^2 values close to 1 and minimal systematic variation in the fit residuals.

DTA and TGA measurements were carried out in air with a heating rate of 10°C min^{-1} from 100°C to 800°C. Pure alumina was used as the reference material. The accuracy of these analyses is about 1-2%.

4.3 Results and discussion

4.3.1 XRD restuls of rGO/Bi

An X-ray powder diffractogram of the as-prepared rGO/Bi with a 2θ range from 10° to 90° is shown in Figure 4.1. The strongest three peaks appear at 27.06°, 37.80°, and 39.46°, which

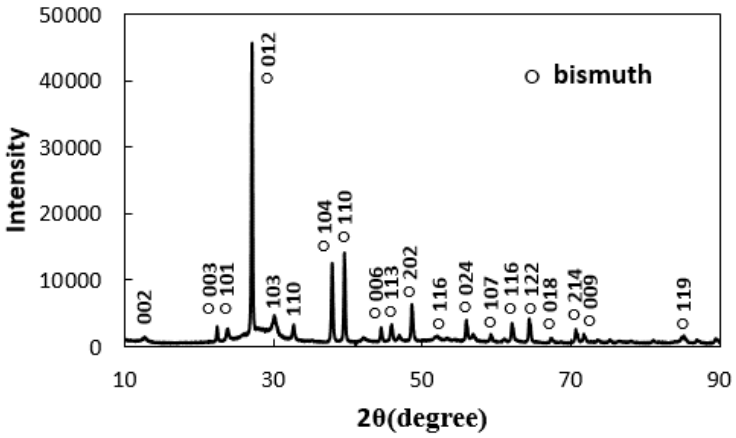

Figure 4.1: X-ray powder diffractogram of rGO/Bi.

correspond to the (012), (104), and (110) reflections of bismuth, respectively (Natl. Bur. Stand. (U.S.)), and therefore confirm the dominant presence of bismuth metal on the graphene surface. The weak peak which appears at 12.64° indicates an interlayer spacing of 0.7 nm, which could be related to graphene oxide [35]. The small hump around 25° is caused by the disordered stacking of layers of rGO [36]. Peaks with positions at 30.02° and 32.66° cannot be indexed with the crystal structure of Bi, but agree with the (103) and (110) crystal planes of bismuth subcarbonate (Natl. Bur. Stand. (U.S.)). Both graphene oxide and EG, which were used as starting materials, could be the carbon source for the $Bi_2O_2CO_3$ observed. The absence of peaks related to bismuth oxides in the diffractogram of the as-prepared composite indicates that the starting material primarily consists of rGO and bismuth metal. It has previously been observed that bismuth metal nanostructures, such as nanowires or nanoparticles are readily oxidized when exposed to air at atmospheric pressure [37–39]. Metallic Bi wires typically have an oxide layer $\sim$1 nm thick after 4 h exposure to air [38]. After 48 h exposure, the thickness of the oxide layer is $\sim$4 nm [38]. High temperature hydrogen and ammonia environments were found to reduce the oxide without damaging the Bi metal after a sufficient amount of time, but the oxide was found to reform in less than 1 min of exposure to air [39]. We note that graphene sheets act as impermeable atomic membranes to many gases [40] and therefore it is likely that the absence of significant bismuth oxidation observed in the as-prepared materials is related to a retardation of this process though protection of bismuth by rGO.

4.3.2 FTIR and Raman spectroscopy of GO and rGO/Bi

FTIR spectra of GO and rGO/Bi are presented in Figure 4.2. The transmittance is recorded within a wavenumber range from 400 cm^{-1} to 4000 cm^{-1}. In the FTIR spectroscopy data of

GO, a broad peak is present between 800 to 1400 cm^{-1} which is assigned to in phase C-C-O stretching (800-1000 cm^{-1}), out of phase C-C-O stretching (1000-1260 cm^{-1}) and C-O-H bending (1200-1430 cm^{-1}) modes [41]. The peaks observed at around 1600 cm^{-1} and 1720

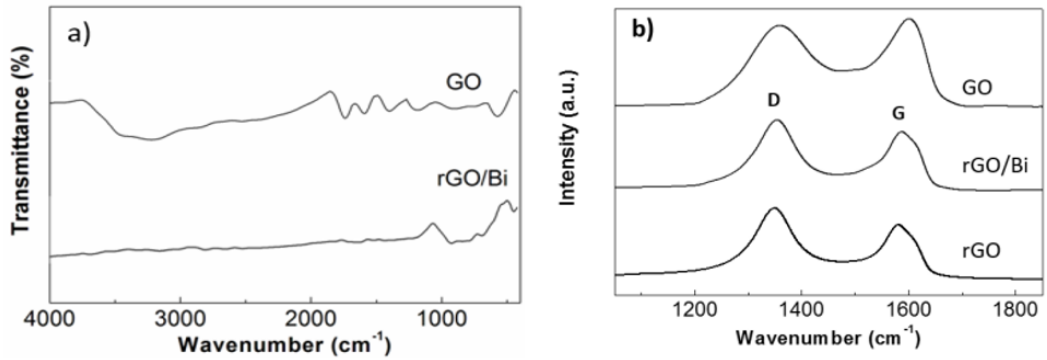

Figure 4.2: a) FTIR spectra of GO and rGO/Bi b) Raman spectra of GO, rGO/Bi and rGO.

cm^{-1} are attributed to the skeletal vibration from unoxidized graphitic domains and the C=O stretching of unsaturated carbonyl groups, respectively [41, 42]. The broad peak appearing at 3200-3600 cm^{-1} originates from the hydrogen bonded OH stretching vibration [41, 43]. In the FTIR spectrum from rGO/Bi, the peak at 424 cm^{-1} mainly arises from the displacement of oxygen atoms with respect to Bi causing Bi O bond elongation [44]. The peak which appears at 675 cm^{-1} results from Bi-O bonds of different lengths in distorted BiO_6 units [45]. The broad peak at around 845 cm^{-1} can be attributed to the antisymmetric stretching of CO3 groups [46]. Compared with the FTIR result from GO, rGO/Bi has fewer peaks in the range from 1200 to 2000 cm^{-1} and from 3200 to 3600 cm^{-1}, which indicates the successful removal of oxygen functional groups from the surface of GO.

Raman spectroscopy was used to compare the density of defects in GO, rGO/Bi and rGO, Figure 4.2 b). A wavenumber range from 1100 cm^{-1} to 1900 cm^{-1} is used. Two obvious peaks, which appear at around 1580 cm^{-1} (G band) and 1350 cm^{-1} (D band), were observed in all three materials. The peak at 1580 cm^{-1} is caused by the in-phase vibration of the sp^2 graphite lattice while the peak at 1350 cm^{-1} results from structural defects and disorder [47, 48]. The intensity ratio of the D and G band peaks (I_D/I_G) changes from 0.90 in GO to 1.17 in rGO/Bi and 1.29 in rGO, indicating a decrease in the average size of the sp^2 domains. Similar results have been reported in the literature [23] and explained in terms of the creation of new graphitic domains which are smaller in size but larger in quantity compared with those in GO.

4.3.3 SEM and TEM images of rGO/Bi

The layered substance shown in the Scanning Electron Microscopy (SEM) images in Figure 4.3, with dimensions larger than 1 μm, can be identified as rGO [49]. Therefore, the particles

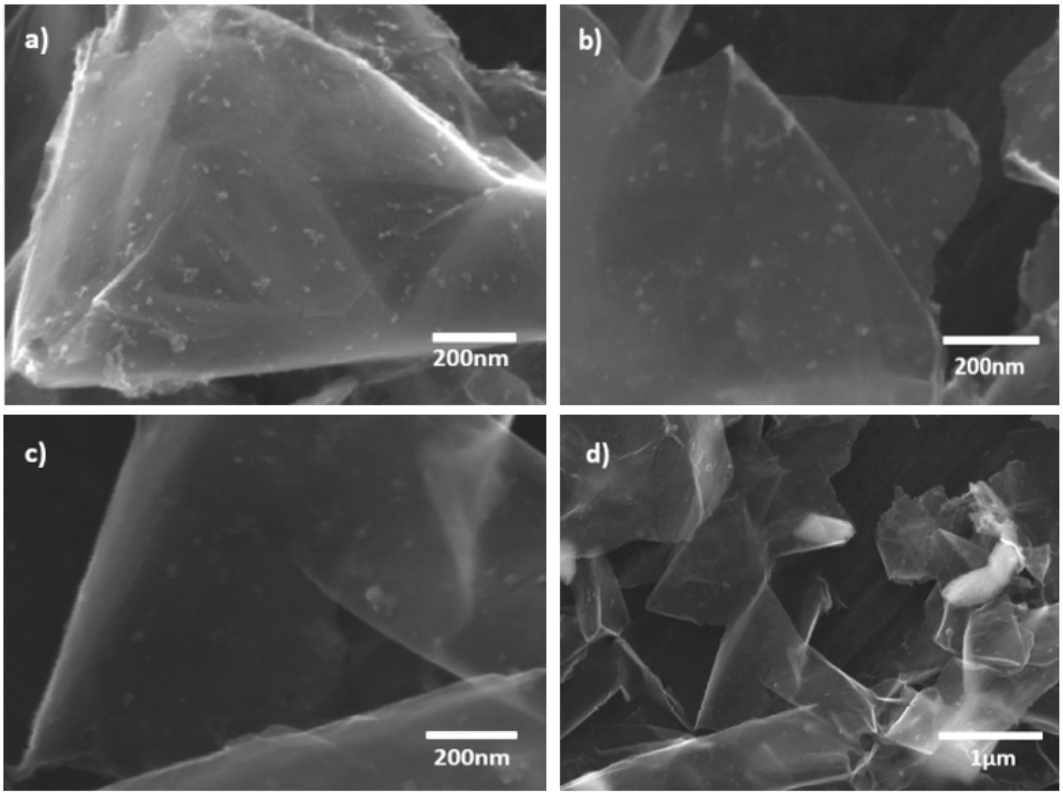

Figure 4.3: SEM images of the as prepared rGO/Bi composite at a) 80,000x, b) 100,000x, c) 100, 000x and d) 25, 000x magnification.

with lateral sizes in the range of 20 to 50 nm attached to the rGO layers are considered to be bismuth (see also discussion below). In some parts of the rGO/Bi samples bismuth particles are seen to have agglomerated and formed clusters with sizes larger than 500 nm, as demonstrated by the white agglomeration in Figure 4.3 d).

Transmission Electron Microscopy (TEM) images of rGO and rGO/Bi are shown in Figure 4.4 a) and b) respectively. Agglomeration is observed to occur in isolated regions of the sample, forming bismuth aggregates with sizes larger than 200 nm, as seen in Figure 4.4 c). A selected area electron diffraction (SAED) pattern (Figure 4.4 d)) of one such particle in Figure 4.4 c) confirms the crystal structure of metallic bismuth. Three rings are observed in this diffraction pattern, which correspond to reflections from the (012), (110), and (300) planes of bismuth metal (Natl.Bur.Stand.(U.S.)). The SAED pattern agrees well with the strong peaks associated with metallic bismuth observed in XRD (Figure 4.1).

An additional crystalline structure, Figure 4.4 e), was observed in some locations in the sam-

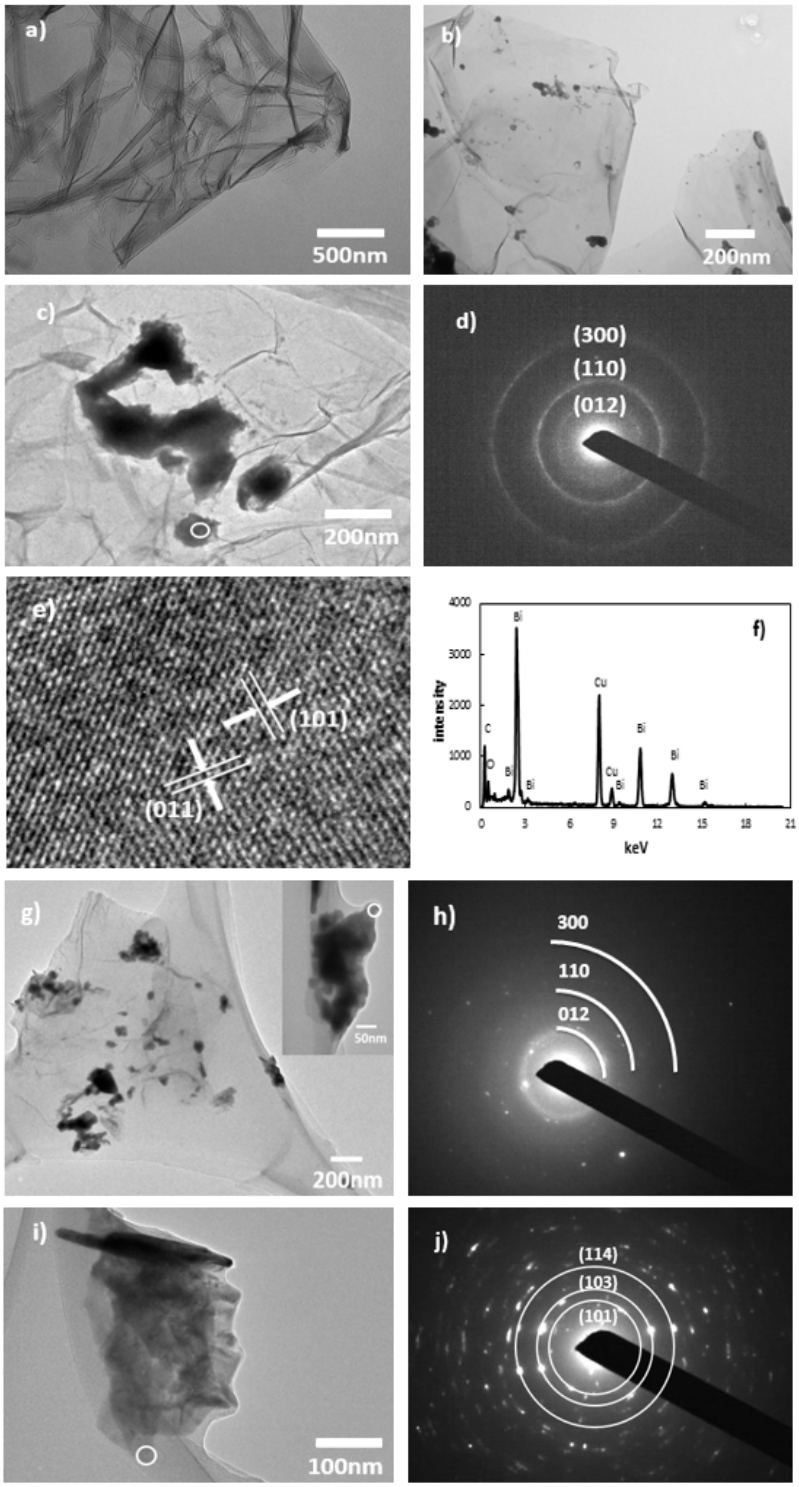

Figure 4.4: a) TEM image of rGO; b) TEM image of as-prepared rGO/Bi; c) TEM image of rGO/Bi showing a region containing Bi agglomerates; d) selected area electron diffraction (SAED) measured on rGO/Bi; e) crystalline structure observed by HRTEM in as-prepared rGO/Bi; f) EDS from as-prepared rGO/Bi; g) TEM image of rGO/Bi after electrochemical cycling; h) selected area electron diffraction (SAED) after electrochemical cycling showing the presence of metallic Bi; i) TEM images of rGO/Bi after electrochemical cycling; j) selected area electron diffraction (SAED) after electrochemical cycling, showing the presence of bismuth subcarbonate.

ple. The atomic structure shown in the TEM image could be indexed with the (101) and (011) crystal lattice planes of bismuth subcarbonate. This result confirms the existence of small quantities of bismuth subcarbonate as impurities, again in agreement with the XRD results presented in Figure 4.1. Energy dispersive X-ray spectroscopy (EDS) from the rGO/Bi composite (Figure 4.4 f)) displays strong Bi, C, and Cu peaks. Bi peaks originate from bismuth particles and bismuth subcarbonate and the C peak could contain contributions from both rGO and $Bi_2O_2CO_3$. The Cu peaks are a result from the Cu TEM support grid. The low C peak intensity compared with the high Bi peak intensity suggests that the amount of bismuth subcarbonate is not great. Figure 4.4 g) and i) show TEM images of the rGO/Bi composite after cycling. Agglomeration is observed to occur, forming particles with sizes from 100 to 200 nm. Both bismuth, Figure 4.4 h), and bismuth subcarbonate, Figure 4.4 j), were observed in the SAED patterns obtained after electrochemical cycling.

4.3.4 BET of rGO/Bi and rGO

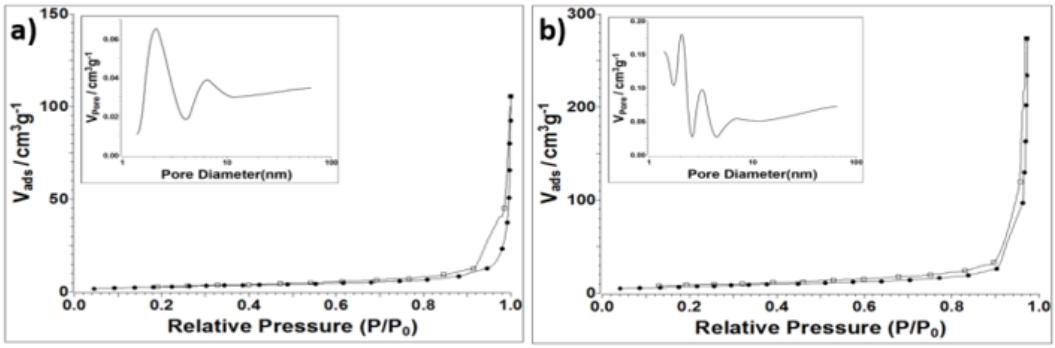

Figure 4.5: Nitrogen adsorption-desorption isotherms of a) rGO/Bi b) rGO.

The microstructure and pore size distribution of rGO and rGO/Bi were determined from N_2 adsorption-desorption isotherms, Figure 4.5 a) and b), respectively. Both isotherms can be classified as type I isotherms for microporous solids [50]. The as-synthesized rGO/Bi is found to have a specific surface area of 10.55 m^2 g^{-1} with pore size diameters in the range from 2-8 nm while the rGO has a specific surface area of 23 m^2 g^{-1} with pore size diameters of 1$\sim$3 nm. Compared with rGO, the rGO/Bi composite has a larger pore size, which may originate from the insertion of Bi nanoparticles into the material and can facilitate more ready penetration of ions into the composite electrode, increasing surface accessibility. Given that approximately half the weight of the rGO/Bi composite consists of rGO the reduction in specific surface area by a factor of $\sim$2 suggests that the incorporation of bismuth has not significantly changed the total surface area offered by the rGO component.

4.3.5 XPS of rGO/Bi

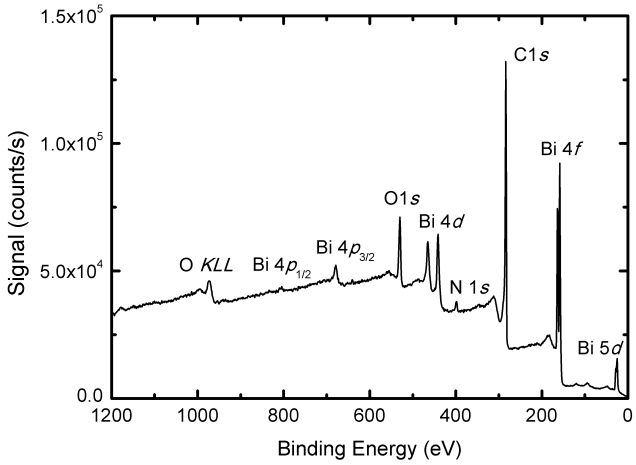

Figure 4.6: XP survey spectrum obtained from 27 month-old rGO/Bi composite.

X-ray photoelectron spectroscopy (XPS) was performed on rGO/Bi composites 27 months after fabrication. Figure 4.6 shows a survey spectrum obtained from the rGO/Bi composite. There are strong peaks associated with bismuth, oxygen and carbon. A small signal from nitrogen is also present corresponding to a concentration of <2 at.% which, in the absence of any signal from $Bi(NO_3)_3$ (see Figure 4.7), is likely to originate from nitrogen inclusion in the rGO resulting from hydrazine treatment, as previously observed by Park et al. [51]. No other elements can be detected.

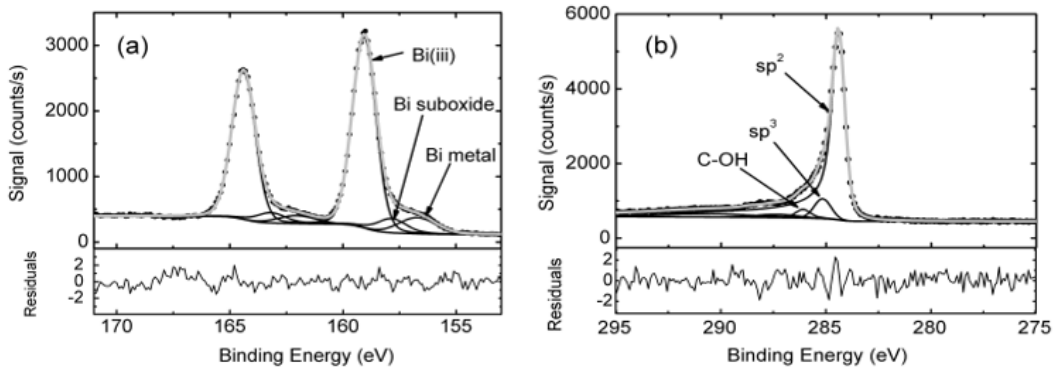

Figure 4.7: a) Top panel: Bi4f XP spectrum of the rGO/Bi composite and associated fit. The Bi 4f7/2 components are associated with metallic Bi, Bi suboxide and Bi in the +3 oxidation state (Bi(III)). Bottom panel: Fit residuals in units of standard deviation of the data. b) Top panel: C1s XP spectrum of the rGO/Bi composite and associated fit. The three largest fit components, associated with sp^2, sp^3 carbon and C-OH are labelled. Bottom panel: Fit residuals in units of standard deviation of the data. In both spectra black dots represent the experimental data, the grey line the fit to the spectrum and the black lines the individual fit components and Shirley background.

A high resolution XP spectrum of the Bi 4f lines is presented in Figure 4.7 a) along with the

associated fit. Three components are necessary to fit the spectrum, the strongest a doublet with the 4f7/2 component at 159.05±0.04 eV and a 4f5/2 component 164.38±0.04 eV which corresponds to bismuth in the +3 oxidation state in $Bi_2O_2CO_3$ [52] and Bi_2O_3 [53]. The doublet located at 156.70±0.04 eV (4f7/2) and 162.03±0.04 eV (4f5/2) is due to metallic bismuth [54], whilst the third doublet, located at 157.8±0.1 eV (4f7/2) and 163.1±0.1 eV (4f5/2), which must be included to ensure an appropriate fit, can be attributed to bismuth suboxides, such as BiO [55]. There is no evidence for Bi4f components associated with residual $Bi(NO_3)_3$ [54] or Bi in the +5 oxidation state in the XP spectrum. The relative strength of the Bi(III)-related doublet in comparison with that of the metal is explained by the surface sensitivity of XPS: using the approach of Tanuma, Powell and Penn [56] we determine the electron inelastic mean free path for the Bi 4f lines to be ∼3 nm. Hence, a thin oxide layer present on Bi particles at the surface of the composite would be expected to dominate the XPS signal. Indeed, the presence of a 4f component associated with metallic bismuth demonstrates that the surface oxide layer is no more than a few nanometres in thickness.

A high resolution XP spectrum of the C1s region is shown in Figure 4.7 b). The signal is dominated by an asymmetric graphitic line (Doniach-*Šunjić* lineshape, α= 0.14) with a binding energy of 284.40±0.05 eV, consistent with graphitic materials. Small peaks (<5% of total C1s intensity) associated with C-OH, C=O and O=C OH are located at 286.1±0.5, 287.3±0.5 and 288.7±0.5 eV binding energy, respectively, reflecting residual oxygen containing groups on the rGO surface [57]. The fit component associated with C-OH is the largest of these, consistent with previous observations that residual –OH groups are the most prevalent oxygen containing groups in rGO after hydrazine treatment [57] (although there may also be a contribution to this component from carbon bound to nitrogen [23]). In order to obtain a good fit it was also necessary to include a minor peak (<10% of total C1s intensity) at 285.2±0.2 eV, which has previously been associated with sp^3 hybridised defects within nanostructured carbons [33, 34] suggesting that residual disorder remains in the rGO when oxygen-containing groups are removed.

The composition of the rGO/Bi composite was determined from the XP spectra by standard approaches [58] using photoelectron cross-sections calculated by Yeh and Lindau [59] and inelastic mean free paths determined as above [56]. The composite was found to contain C, O and Bi in the (atomic) ratio 0.78:0.18:0.03 (with an estimated error of ±0.02 for each species).

4.3.6 DTA and TGA of rGO/Bi and rGO

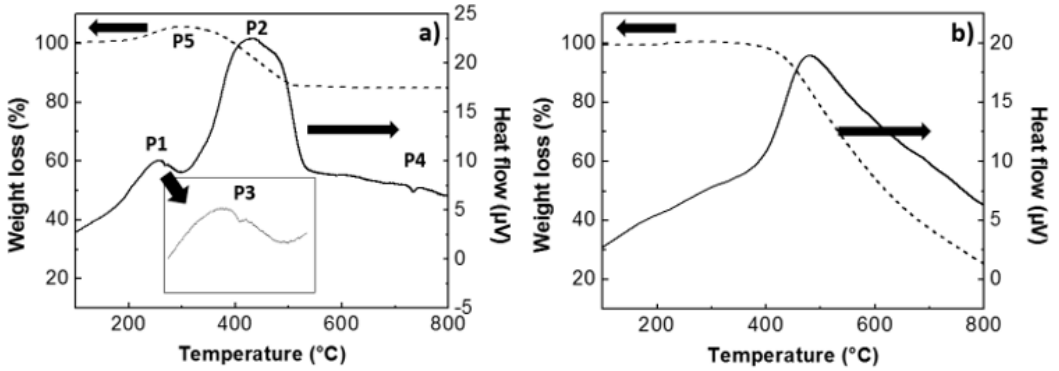

Figure 4.8: DTA and TGA curves of a) rGO/Bi b) rGO.

Differential thermal analysis (DTA) and thermo-gravimetric analysis (TGA) curves of rGO/Bi and rGO are presented in Figure 4.8. The DTA data from the rGO/Bi composite, Figure 4.8 a), show two broad exothermic peaks, P1 and P2, and two very small endothermic peaks, P3 and P4. P1 can be attributed to the adsorption of oxygen at the surface of rGO in the presence of Bi at low temperatures (175-250°C). The small endothermic peak P3, at about 275°C, is associated with the melting of metallic bismuth. The exothermic peak P2 is very broad and represents an overlap of different exothermic processes: oxidation of bismuth between 325-375°C which involves a mass increase of 2-3 wt% and carbon combustion between 355-525°C, accompanied by a mass loss of 18-20 wt%. The small endothermic peak, P4, at 730°C has no mass variation associated with it and probably corresponds to melting of bismuth oxide, with the melting peak shifted to low temperatures due to the nanometer-scale dimensions of the particles. The broad peak labelled P5 in the TGA data from rGO/Bi, showing a mass increase of around 5 wt%, probably corresponds to the combined effects of the processes described by the exothermic peak P1 and part of P2 in the DTA curve, attributed to bismuth oxidation.

The DTA curve of rGO powder, Figure 4.8 b), exhibits only one broad exothermic peak with an onset temperature of about 400°C. This exothermic behaviour is attributed to carbon combustion in air and takes place with a mass loss of 74 wt%. In the absence of Bi the rGO combustion peak is shifted to higher temperatures. Over the temperature 450°C to 800°C rGO/Bi has a smaller weight loss compared with rGO. This might be because by adding the Bi nanoparticles, the rGO/Bi has better graphitization and de-oxygenation with enhanced van der Waals interactions between layers [60].

Based on the 5.13% weight gain (peak P5), bismuth and rGO have a weight ratio of 0.44:0.56. This is in good agreement with the atomic ratio given by XPS (bismuth and carbon were found

by XPS to have an atomic ratio of 0.03:0.78, as discussed above, which corresponds to a weight ratio of 0.4:0.6).

4.3.7 Electrochemical properties of rGO/Bi and rGO

Electrochemical properties of the as-prepared rGO/Bi, rGO and Ni foam were analysed by cyclic voltammetry under different scanning rates, as shown in Figure 4.9. Electrochemical

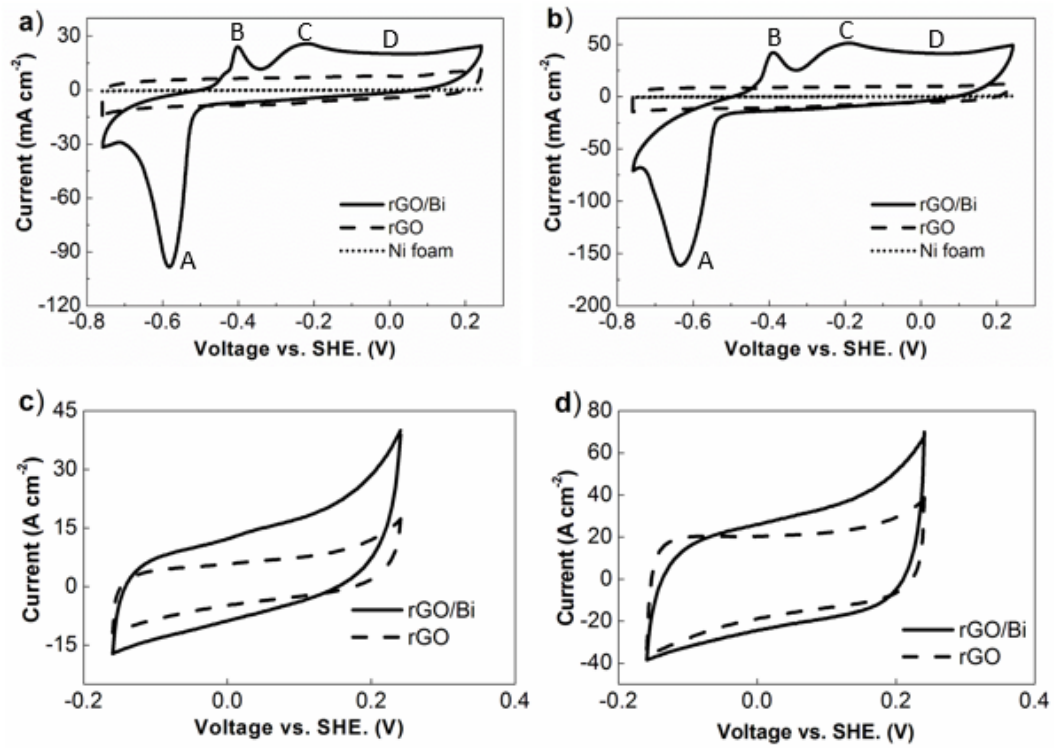

Figure 4.9: Typical CV results of rGO/Bi, rGO and Ni foam within different voltage range at scan rates of a) 20mV s^{-1} b) 50mV s^{-1} c) 20mV s^{-1} d) 50mV s^{-1}.

properties of the as-prepared rGO/Bi, rGO and Ni foam were analysed by cyclic voltammetry under different scanning rates, as shown in Figure 4.9. Cyclic voltammetry measured at different scanning rates, 20 mV s^{-1} and 50 mV s^{-1}, presented similar shaped curves. Voltages from 0.2 to 0.8 V vs. standard hydrogen electrode (SHE) were applied. Three clear peaks (A, B and C) and a small plateau (D) were observed in the cyclic voltammetry experiments. Peak A, which appears at around -0.6 V, is associated with the reduction of Bi from the +3 oxidation state to the metallic state (0 oxidation state) [61]. Peaks B and C, which appear at -0.45 V and -0.25 V, represent the formation of BiO_2^- and $Bi(OH)_3$ during the oxidation of Bi from metal to the +3 oxidation state [61]. The surface layer of Bi was partially dissolved in the KOH electrolyte and forms BiO_2^- in the first reduction reaction [62]. The plateau D may be due to the oxidation of un-transformed Bi [61]. A previous study has shown that this plateau becomes

dominant in bismuth films as the film thickness is reduced [61]. This plateau has only been observed in thin Bi (metal) films with highly rough surface [61]. In ref [61] it is suggested that very high Bi oxidation states of +4 or +5 might occur due to the hypothetical formation of gel like electrolyte (when Bi metal is rough) and these oxidation states are responsible for the observed plateau through Faradaic processes. However, CV curves of rGO/Bi in the range from -0.2 to 0.24 V (Figure 4.9c) and d)) display a rectangular shape almost identical to that of rGO when scaled for the rGO mass content. It is therefore more likely the constant capacitance value in this potential window indicates that, over this range of potential, the rGO/Bi displays an electric double layer (EDL) capacitance originating primarily from the rGO component in the composite and that the composite electrode therefore demonstrates both supercapactive and battery characteristics.

During the oxidation and reduction processes intermediate products, which include $Bi(OH)_3$, BiOOH, and BiO_2^-, could be formed as following equations [61, 63]:

Peak A

$$BiO_2^- + e^- \rightarrow BiO_2^{2-} \tag{4.1}$$

$$BiO_2^{2-} + 3H_2O \rightarrow 2BiO_2^- + 4OH^- + Bi^{(0)} \tag{4.2}$$

$$Bi^{(0)} \rightarrow Bi_{(metal)} \tag{4.3}$$

Peaks B and C

$$Bi^{(0)} + OH^- \rightarrow BiO_2^- + Bi(OH)_3 + H_2O \tag{4.4}$$

$$Bi(OH)_3 \rightarrow BiOOH + H_2O \tag{4.5}$$

$$BiOOH + OH^- \rightarrow BiO_2^- + H_2 \tag{4.6}$$

Cyclic voltammagrams of pure Ni foam and rGO were also measured and are presented in Figure 4.9 b) for comparison. The CV of rGO measured at both 20 mV s^{-1} and 50 mV s^{-1} show rectangular shapes without any noticeable peaks, which indicates that the capacitance of rGO only arises from electric double layer capacitance [64].

Chronopotentiometry was used to study the charge/discharge behaviours of the as-prepared rGO/Bi and rGO materials. The charge/discharge curves were measured at different current densities, ranging from 0.2 A g^{-1} to 1.2 A g^{-1} (Figure 4.10). The charge/discharge curves of rGO/Bi show similar behaviour at different current densities. In the enlarged discharge curve of rGO/Bi, as in Figure 4.10 c), both slope and plateau were observed.

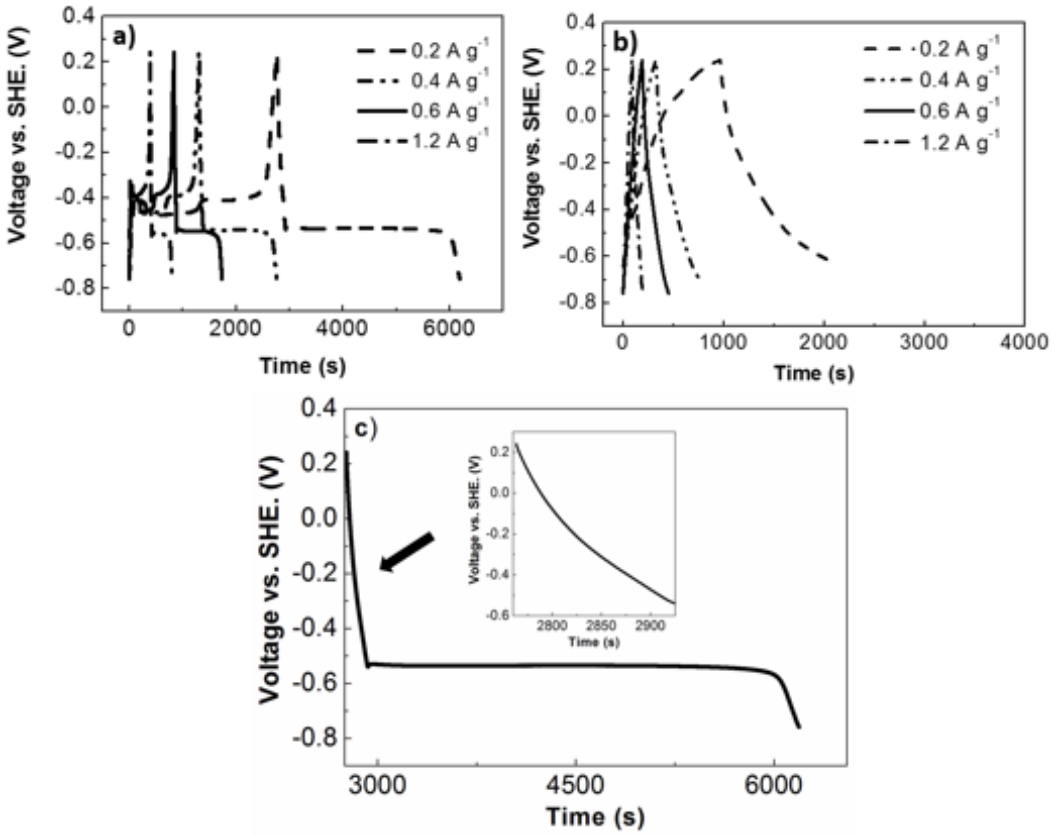

Figure 4.10: Typical charge/discharge behaviours of a) rGO/Bi at different current densities b) rGO at different current densities c) enlarged discharge curve of rGO/Bi at 0.2 A g^{-1}.

The quasi-linear behaviour at the beginning of the discharge curve indicates a contribution from capacitor-like behaviour. This originates from charge stored electrostatically [29] on the surface of rGO, as described above. The plateau indicates material undergoing a phase transformation during the redox reaction [10], as described by peak A in Figure 4.9 a). The charge/discharge curves of rGO/Bi show similar behaviour at different current densities. In the enlarged discharge curve of rGO/Bi, as in Figure 4.10 c), both slope and plateau were observed. Since the energy storage mechanism of rGO/Bi includes a significant non-capacitive Faradaic or battery-like contribution, the appropriate way to measure the amount of charge stored in the electrode is the specific capacity C_s using [6, 65]

$$C_s = \frac{i \times \Delta t}{m} \tag{4.7}$$

where C_s is the specific capacity (C g^{-1}), i/m is the current density employed in the measurement (A g^{-1}), Δt is the discharging time in seconds [65].

Figure 4.11 shows the specific capacity of the rGO/Bi composites calculated from the charge/discharge curves. Composite samples achieved a specific capacity value as high as 773 C g^{-1} at a current

density of 0.2 A g^{-1}. The specific capacity is seen to decrease as the current density increases, which can be attributed to incomplete utilization of the active material at high current densities [18]. When a high current density is used, the redox reaction only occurs at the surface of active materials [17]. However, the rate at which the specific capacity drops decreases with increasing current density, indicating that the electrode material can still show good capacity even at high current density. When the current density reaches the range of 0.4 A g^{-1} to 1.2 A g^{-1}, the specific capacity maintains almost a constant value, in the range of 587 C g^{-1} to 494 C g^{-1}. The specific capacitance of the pure rGO was found to be 283 F g^{-1} at a current density of 0.2 A g^{-1}, which is comparable to the value of 205 F g^{-1} found for gas-phase reduced rGO [66]. At a current density of 1.2 A g^{-1}, the specific capacitance of rGO was found to decrease to 125 F g^{-1}, which, at a potential of 1 V, stores approximately a quarter of the capacity value found for the rGO/Bi material.

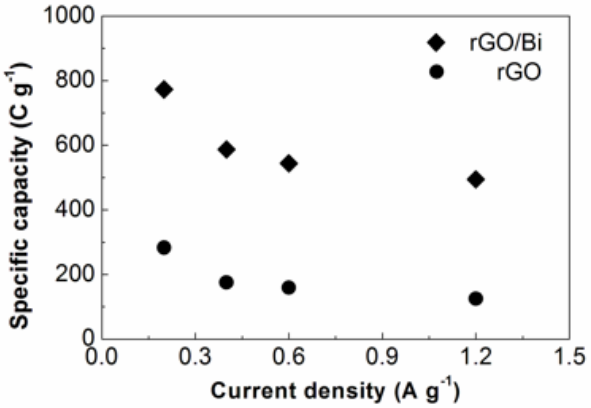

Figure 4.11: Specific capacity of rGO/Bi and rGO calculated from charge/discharge curves.

From the Bi content of the rGO/Bi composite it is possible to calculate the maximum theoretical contribution to the total specific capacity of the electrode from this component of the material. The theoretical specific capacity value of bismuth can be estimated from the following equation

$$C = \frac{aF}{M} = \frac{3 \times 96487 Cmol^{-1}}{209 gmol^{-1}} = 1385 Cg^{-1} \tag{4.8}$$

where C is the theoretical capacity, a is the oxidation state changes during the faradaic reaction, F is the Faraday constant and M is the molecular weight. The specific capacity associated with oxidation of bismuth is 1375 C g^{-1} resulting in a contribution to the electrode material of 600±20 C g^{-1} (170±6 mAh g^{-1}). If the specific capacitance of the rGO in the composite is unaltered we would therefore expect a contribution to the specific capacity of the electrode of 160±3 C g^{-1} when the voltage range of the galvanic discharge curve is 1 V (as used in our experiments). Hence, we would expect a theoretical specific capacity of 760±20 C

g^{-1} for the composite over a potential of 1 V if all the bismuth present participates in electrochemical storage, which is remarkably close to the 773 C g^{-1} measured at a discharge current of 0.2 A g^{-1}. This result suggests high accessibility of the bismuth within the rGO/Bi composite, reflecting the larger pore size of the composite material, compared with rGO, as described above.

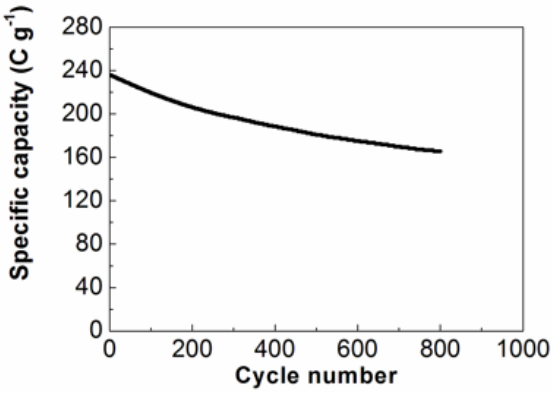

Figure 4.12: Life-cycle test of rGO/Bi composite under 5 A g^{-1} current density.

Cycling performance was determined by repeating the charge/discharge test 800 times at a current density of 5 A g^{-1}. This sample achieves a specific capacity of 235 C g^{-1} at the start of cycling, which gradually decreases to 175 C g^{-1} after 800 cycles. Hence, 74.5% of the specific capacity was maintained after 800 cycles. The gradual decrease of capacity during cycling may be due to degradation of the active material, Bi [24]. In addition, the relatively faster decrease in the capacity of rGO/Bi composite during the first 200 cycles and slower decrease over the following cycles indicates that structural changes may also have taken place during the charge/discharge cycles, such as the agglomeration observed in the TEM images shown in Figure 4.4 g) and i). After the structure has changed, this sample has a more stable cycling performance, demonstrating a moderate long term electrochemical stability.

4.4 Conclusion

A reduced graphene oxide (rGO)/Bismuth composite, in which the reduced graphene oxide inhibits atmospheric bismuth oxidation, has been synthesized the first time through a polyol process in which ethylene glycol was used as both the solvent and reducing agent. The low reaction temperature, short reaction time and low cost of starting materials make this synthesis procedure appropriate for large scale application. The composite material is found to consist of bismuth nanoparticles with lateral sizes between 20 and 50 nm supported by rGO. The

as-prepared rGO/Bi composites displayed specific capacity values as high as 773 C g^{-1} at a current density of 0.2 A g^{-1}. The capacity of the rGO/Bi composite described in this work can be attributed to the excellent accessibility of the bismuth and the efficiency of electrochemical reaction resulting from high electrode conductivity and good contact between the bismuth nanoparticles and rGO. Since the electrochemical behaviour of the composite shows contributions from the electric double layer capacitance of the rGO and Faradaic charge storage associated with bismuth, it is reasonable to describe rGO/Bi as a "supercapattery" material. This material has a moderate stability in cycling tests even at current densities as high as 5 A g^{-1}. The excellent electrochemical properties of the rGO/Bi composite, simplicity of production and low cost indicate that this material is a promising candidate as an electrode material in electrochemical energy storage devices.

References

[1] P. Simon and Y. Gogotsi, "Materials for electrochemical capacitors," *Nature Materials*, vol. 7, pp. 845–845, 2008.

[2] B. E. Conway, "Transition from supercapacitor to battery behavior in electrochemical energy storage," *Journal of Electrochemical Society*, vol. 138, pp. 1539–1548, 1991.

[3] P. Simon, Y. Gogotsi, and B. Dumn, "Where do batteries end and supercapacitors begin? ," *Science*, vol. 343, pp. 1210–1211, 2014.

[4] F. Yao, D. T. Pham, and Y. H. Lee, "Carbon-based materials for lithium-ion betteries, electrochemical capacitors, and their hybrid devices," *ChemSusChem*, vol. 8, pp. 2284–2311, 2015.

[5] E. Frackowiak and F. Beguin, "Carbon materials for the electrochemical storage of energy in capacitors," *Carbon*, vol. 39, pp. 937–950, 2001.

[6] N. Padmanathan, H. Shao, D. McNulty, C. O'Dwyer, and K. M. Razeeb, "Hierarchical NiO–In_2O_3microflower (3D)/ nanorod (1D) hetero-architecture as a supercapattery electrode with excellent cyclic stability," *Journal of Materials Chemistry A*, vol. 4, pp. 4820–4830, 2016.

[7] L. Yu and G. Z. Chen, "High energy supercapattery with an ionic liquid solution of $LiClO_4$," *Faraday Discussion*, vol. 190, pp. 231–240, 2016.

[8] J. H. Chae, X. Zhou and G. Z. Chen, "From electrochemical capacitors to supercapatteries," *Green*, vol. 2, pp. 41–54, 2012.

[9] A. Ghosh and Y. H. Lee, "Carbon-based electrochemical capacitors," *ChemSusChem*, vol. 5, pp. 480–499, 2012.

[10] A. Veronica, S. Patrice, and D. Bruce, "Pseudocapacitive oxide materials for high-rate electrochemical energy storage," *Energy & Environmental Science*, vol. 7, pp. 1597–1614, 2014.

[11] B. S. Lou, P. Veerakumar, S. S. M. Chen, V. Veeramani, R. Madhu, and S. B. Liu, "Ruthenium nanoparticles decorated curl-like porous carbons for high performance supercapacitors," *Scientific Reports*, vol. 6, p. 19949, 2016.

[12] X. He, K. Xie, R. Li, and M. Wu, "Microwave-assisted synthesis of Ru/mesoporous carbon composites for supercapacitors," *Materials Letters*, vol. 115, pp. 96–99, 2014.

[13] G. Yu, W. Chen, Y. Zheng, J. Zhao, X. Li, and Z. Xu, "Synthesis of Ru/carbon nanocomposites by polyol process for electrochemical supercapacitor electrodes," *Materials Letters*, vol. 60, pp. 2453–2456, 2006.

[14] H. Nakanishi and B. A. Grzybowski, "Supercapacitors based on metal electrodes prepared from nanoparticle mixtures at room temperature," *The Journal of Physical Chemistry Letters*, vol. 1, pp. 1428–1431, 2010.

[15] L. Fu, K. Tang, C. C. Chen, L. Liu, X. Guo, Y. Yu, and J. Maier, "Free-standing Ag/C coaxial hybrid electrodes as anodes for Li-ion batteries," *Nanoscale*, vol. 5, pp. 11 568–11 571, 2013.

[16] T. Romann and E. Lust, "Electrochemical properties of porous bismuth electrodes," *Electrochimica Acta*, vol. 55, pp. 5746–5752, 2010.

[17] T. P. Gujar, V. R. Shinde, C. D. Lokhande, and S. H. Han, "Electrosynthesis of Bi_2O_3 thin films and their use in electrochemical supercapacitors," *Journal of Power Sources*, vol. 161, pp. 1479–1485, 2006.

[18] K. Gopalsamy, Z. Xu, B. Zheng, T. Huang, L. Kou, X. Zhao, and C. Gao, "Bismuth oxide nanotubes-graphene fiber-based flexible supercapacitors," *Nanoscale*, vol. 6, pp. 8595–8600, 2014.

[19] H. Wang, Z. Hu, Y. Chang, Y. Chen, Z. Lei, Z. Zhang, and Y. Yang, "Facile solvothermal synthesis of a graphene nanosheet–bismuth oxide composite and its electrochemical

characteristics," *Electrochimica Acta*, vol. 55, pp. 8974–8980, 2010.

[20] J. T. Sun, H. Huang, S. L. Wong, H. J. Gao, Y. P. Feng, and A. T. Wee, "Energy-gap opening in a Bi(110) nanoribbon induced by edge reconstruction," *Physical Review Letters*, vol. 109, pp. 246 804(1–5), 2012.

[21] T. Hirahara, T. Shirai, T. Hajiri, M. Matsunami, K. Tanaka, S. Kimura, S. Hasegawa, and K. Kobayashi, "Role of quantum and surface-state effects in the bulk Fermi level position of ultrathin Bi films," *Physical Review Letters*, vol. 115, pp. 106 803(1–3), 2015.

[22] N. M. Leonard, L. C. Wieland, and R. S. Mohan, "Applications of bismuth(III) compounds in organic synthesis," *Tetrahedron*, vol. 58, pp. 8373–8397, 2002.

[23] S. Stankovich, D. A. Dikin, R. D. Piner, K. A. Kohlhaas, A. Kleinhammes, Y. Jia, Y. Wu, S. T. Nguyen, and R. S. Ruoff, "Synthesis of graphene-based nanosheets via chemical reduction of exfoliated graphite oxide," *Carbon*, vol. 45, pp. 1558–1565, 2007.

[24] M.Kerlau, M.Marcinek, V.Srinivasan, and R.M.Kostecki, "Studies of local degradation phenomena in composite cathodes for lithium-ion batteries," *Electrochimica Acta*, vol. 52, pp. 5422–5429, 2007.

[25] K. J. Carroll, J. U. Reveles, M. D. Shultz, S. N. Khanna, and E. E. Carpenter, "Preparation of elemental Cu and Ni nanoparticles by the polyol method: an experimental and theoretical approach," *The Journal of Physical Chemistry C*, vol. 115, pp. 2656–2664, 2011.

[26] M. F. El-Kady, Y. Shao and R. B. Kaner, "Graphene for batteries, supercapacitors and beyond," *Nature Reviews Materials*, vol. 1, pp. 1–14, 2016.

[27] S. Wang, C. Jin, and W. Qian, "Bi_2O_3 with activated carbon composite as a supercapacitor electrode," *Journal of Alloys and Compounds*, vol. 615, pp. 12–17, 2014.

[28] L. Guan, L. Yu and G. Z. Chen, "Capacitive and non-capacitive faradaic charge storage," *Electrochemica Acta*, vol. 206, pp. 464–478, 2016.

[29] T. Brousse, D. Belanger, and J. W. Long, "To be or not to be pseudocapacitive?" *Journal of Electrochemistry Society*, vol. 162, pp. 5185–5189, 2015.

[30] W. S. Hummers and R. E. Offman, "Preparation of graphite oxide," *Journal of American Chemistry Society*, vol. 80, pp. 1339–1339, 1958.

[31] R. Hesse, T. Chasse, and R. Szargan, "Unifit 2002 universal analysis software for photo-

electron spectra," *Analytical and Bioanalytical Chemistry*, vol. 375, pp. 856–863, 2003.

[32] M. R. C. Hunt, "Surface and bulk components in angle resolved core level photoemissioin spectroscopy of graphite," *Physical Review B*, vol. 78, p. 153408, 2008.

[33] A. K. Chakraborty, R. A. J. Woolley, Yu. V. Butenko, V. R. Dhanak, L. Šiller, and M. R. C. Hunt, "A photoelectron spectroscopy study of ion irradiation induced defects in single wall carbon nanotubes," *Carbon*, vol. 45, pp. 2744–2750, 2007.

[34] Yu. V. Butenko, S. Krishnamurthy, A. K. Chakraborty, V. L. Kuznetsov, V. R. Dhanak, M. R. C. Hunt, and L. Šiller, "Photoemission study of onion like carbons produced by annealing nanodiamonds," *Physical Review B*, vol. 71, p. 075420, 2005.

[35] K. Zhang, Y. Zhang, and S. Wang, "Enhancing thermoelectric properties of organic composites through hierarchical nanostructures," *Scientific Reports*, vol. 3, pp. 3448(1–7), 2013.

[36] K. Zhu, H. Qiu, Y. Zhang, D. Zhang, G. Chen, and Y. Wei, "Synergetic effects of Al^{3+} doping and graphene modification on the electrochemical performance of V_2O_5 cathode materials," *ChemSusChem*, vol. 8, pp. 1017–1025, 2015.

[37] M. G. Hale, R. Little, M. A. Salem, J. H. Hedley, B. R. Horrocks, and L. Šiller, "Formation of bismuth oxide nanowires by simultaneous templating and electrochemical adhesion of DNA on Si/SiO_2," *Thin Solid Films*, vol. 520, pp. 7044–7048, 2012.

[38] Z. Zhang, D. Gekhtman, M. S. Dresselhaus, and J. Y. Ying, "Processing and characterization of single-crystalline ultrafine bismuth nanowires," *Chemistry of Materials*, vol. 11, pp. 1659–1665, 1999.

[39] S. B. Cronin, Y. Lin, P. L. Gai, O. Rabin, M. R. Black, G. Dresselhau, and M. S. Dresselhaus, "4-point resistance measurements of individual bi nanowires," *Materials Research Society Symposium C*, vol. 635, pp. 5–7, 2000.

[40] J. S. Bunch, S. S. Verbridge, J. S. Alden, A. M. Zande, J. M. Parpia, H. G. Craighead, and P. L. McEuen, "Impermeable atomic membranes from graphene sheets," *Nano Letters*, vol. 8, pp. 2458–2462, 2008.

[41] W. G. F. D. L. Vien, N. B. Colthup and J. G. Graselli, *The handbook of infrared and Raman characteristic frequencies of organic molecules*. San Diego: Academic Press, 1991.

[42] D. Li, M. B. Muller, S. Gilje, R. B. Kaner, and G. G. Wallace, "Processable aqueous dis-

persions of graphene nanosheets," *Nature Nanotechnology*, vol. 3, pp. 101–105, 2008.

[43] E. Y. Choi, T. H. Han, J. Hong, J. E. Kim, S. H. Lee, H. W. Kim, and S. O. Kim, "Noncovalent functionalization of graphene with end-functional polymers," *Journal of Materials Chemistry*, vol. 20, pp. 1907–1912, 2010.

[44] S. N. Narang, N. D. Patel, and V. B. Kartha, "Infrared and raman spectral studies and normal modes of a-Bi_2O_3," *Journal of Molecular Structure*, vol. 327, pp. 221–235, 1994.

[45] M. A. Girsova, G. F. Golovina, L. N. Kurilenko, and T. V. Antropova, "Synthesis and study of bismuth-containing high-silica glass by the IR spectroscopy method," *Glass Physics and Chemistry*, vol. 41, pp. 93–97, 2015.

[46] H. Huang, N. Tian, S. Jin, Y. Zhang, and S. Wang, "Syntheses, characterization and nonlinear optical properties of a bismuth subcarbonate $Bi_2O_2CO_3$," *Solid State Sciences*, vol. 30, pp. 1–5, 2014.

[47] K. N. Kudin, B. Ozbas, H. C. Schniepp, and R. K. Prud'homme, "Raman spectra of graphite oxide and functionalized graphene sheets," *Nano Letters*, vol. 8, pp. 36–41, 2008.

[48] K. Han, J. Shen, S. Hao, H. Ye, C. Wolverton, M. C. Kung, and H. H. Kung, "Free-standing nitrogen-doped graphene paper as electrodes for high-performance lithium/dissolved polysulfide batteries," *ChemSusChem*, vol. 7, pp. 2545–2553, 2014.

[49] J. C. Meyer, A. K. Geim, M. L. Katsnelson, K. S. Novoselov, T. J. Booth, and S. Roth, "The structure of suspended graphene sheets," *Nature*, vol. 446, pp. 60–63, 2007.

[50] K. S. W. Sing, "Reporting physisorption data for gas/solid systems with special reference to the determination of surface area and porosity," *Pure Applied Chemistry*, vol. 54, pp. 2201–2218, 1985.

[51] S. Park, Y. Hu, J. O. Hwang, E. S. Lee, L. B. Casabianca, W. Cai, J. R. Potts, H. -W. Ha, S. Chen, J. Oh, S. O. Kim, Y. -H. Kim, Y. Ishii, and R. S. Ruoff, "Chemical structures of hydrazine-treated graphene oxide and generation of aromatic nitrogen doping," *Nature Communications*, vol. 3, p. 638, 2012.

[52] F. Dong, Q. Li, Y. Sun, and W. -K. Ho, "Noble metal like behavior of plasmonic Bi particles as a cocatalyst deposited on $Bi_2O_2CO_3$ microspheres for efficient visible light photocatalysis," *ACS Catalysis*, vol. 4, pp. 4341–4350, 2014.

[53] C. Huang, J. Hu, W. Fan, X. Wu, and X. Qiu, "Porous cubic bismuth oxide nanospheres

a facile synthesis and their conversion to bismuth during the reduction of nitrobenzenes," *Chemical Engineering Science*, vol. 131, pp. 155–161, 2015.

[54] S. Suzer, N. Ertas, and O. Y. Ataman, " XPS characterization of Bi and Mn collected on atom-trapping silica for AAS," *Applied Spectroscopy*, vol. 53, pp. 479–482, 1999.

[55] A. Gulino, S. La Delfa, I. Fragala, and R. G. Egdell, "Low temperature stabilization of tetragonal zirconia by bismuth," *Chemistry of Materials*, vol. 8, pp. 1287–1291, 1996.

[56] S. Tanuma, C. J. Powell, and D. R. Penn, "Calculations of electron inelastic mean free paths. V. Data for 14 organic compounds over the 50-2000 eV range," *Surface and Interface Analysis*, vol. 21, pp. 165–176, 1993.

[57] D. Yang, A. Velamakanni, G. Bozoklu, S. Park, M. Stoller, R. D. Piner, S. Stankovich, I. Jung, D. A. Field, C. A. Ventrice, and R. S. Ruoff, "Chemical analysis of graphene oxide films after heat and chemical treatments by X-ray photoelectron and Micro-Raman spectroscopy," *Carbon*, vol. 47, pp. 145–152, 2009.

[58] M. P. Seah, "The quantitative analysis of surfaces by XPS: A review," *Surface and Interface Analysis*, vol. 2, pp. 222–239, 1980.

[59] J. J. Yeh and I. Lindau, "Atomic subshell photoionization cross sections and asymmetry parameters," *Atomic Data and Nuclear Data Tables*, vol. 32, pp. 1–55, 1985.

[60] Y. Yoon, K. Samanta, H. Lee, K. Lee, A. P. Tiwari, J. Lee, J. Yang, and H. Lee, "Highly stretchable and conductive silver nanoparticle embedded graphene flake electrode prepared by in situ dual reduction reaction," *Scientific Reprots*, vol. 5.

[61] J. Ismail, M. F. Ahmed, and P. V. Kamath, "Cyclic voltammetry studies of electrodeposited thin films of bismuth in 1M KOH," *Journal of Electroanalytical Chemistry*, vol. 354, pp. 51–58, 1993.

[62] V. Vivier, C. C. Vivier, S. Mezaille, B. L. Wu, C. S. Cha, J. Nedelec, M. Fedoroff, D. Michel, and L. T. Yu, "Electrochemical study of Bi_2O_3 and $Bi_2O_2CO_3$ by means of a cavity microelectrode I. Observed phenomena and direct analysis of results," *Journal of the Elecrochemical Society*, vol. 147, pp. 4252–4262, 2000.

[63] V. Vivier, A. Regis, G. Sagon, J. Y. Nedelec, L. T. Yu, and C. Cachet-Vivier, "Cyclic voltammetry study of bismuth oxide Bi_2O_3 powder by means of a cavity microelectrode coupled with Raman microspectrometry," *Electrochimica Acta*, vol. 46, pp. 907–914, 2001.

[64] P. Yadav, A. Banerjee, S. Unni, J. Jog, S. Kurungot, and S. Ogale, "A 3D hexaporous carbon assembled from single-layer graphene as high performance supercapacitor," *ChemSusChem*, vol. 5, pp. 2159–2164, 2012.

[65] H. Chen, S. Chen, Y. Zhu, C. Li, M. Fan, D. Chen, G. Tian, and K. Shu, "Synergistic effect of Ni and Co ions on molybdates for superior electrochemical performance," *Electrochimica Acta*, vol. 190, pp. 57–63, 2016.

[66] Y. Wang, Z. Shi, Y. Huang, Y. Ma, C. Wang, M. Chen and Y. Chen, "Supercapacitor devices based on graphene materials," *Journal of Physical Chemistry C*, vol. 113, pp. 13 103–13 107, 2009.

Chapter 5

Low cost synthesis of Bi_2O_3-GO composite as electrodes used in electrochemical energy storage

5.1 Introduction

Bismuth is the heaviest stable element on the periodic table [1]. In spite of this, bismuth and most of its compounds are safe, non-toxic and non-carcinogenic materials [1]. A large amount of bismuth is produced as by-product of copper and tin refining [1]. This relatively low cost of initial material allows bismuth to be used in a large-scale application.

Bismuth oxide (Bi_2O_3) is known as a transition metal oxide, which could have high capacity value from the reversible redox reaction between 0 and +3 oxidation state [2]. Today, with the increasing concern of the environment and CO_2 emission, the study of using bismuth and bismuth compounds as electrodes in energy storage devices attracts tremendous interests. Some research have been done on study the electrochemical properties of bismuth oxide with different structures. Bi_2O_3 thin films with smooth surfaces prepared by the electrodeposition method have a thickness of 0.74 μm after 15 minutes of electrodeposition [2]. The highest specific capacitance achieved by this Bi_2O_3 is 98 F g^{-1} [2]. Besides the smooth surface of Bi_2O_3 films, hierarchical rippled Bi_2O_3 nanobelts have also been synthesized through the electrodeposition method [3]. The obtained nanobelts have a rippled structure with widths of 250-300 nm, thicknesses of 10-30 nm, and lengths of 1-5 μm [3]. Rippled Bi_2O_3 achieved specific capacitance of 250 F g^{-1} which is much higher than the value of Bi_2O_3 with the smooth sur-

face, 68 F g^{-1} [3].

rGO/Bi_2O_3 composite synthesized by thermal decomposition in a muffle stove reached a specific capacitance of 94 F g^{-1} at a current density of 0.2 A g^{-1} [4]. Bismuth oxide particles with size varying from a few to 150 μm were randomly distributed in corrugated graphene layers [4]. Gopalsamy et.al. synthesized graphene fibre/Bi_2O_3 nanotubes by hydrothermal method [5]. This composite has a specific capacitance of 69.3 mF cm^{-2} at a current density 0.1 mA cm-$^{-2}$ [5]. Bi_2O_3 deposited on highly ordered mesoporous carbon were prepared by chemical reduction followed by calcination [6]. With 62% of Bi_2O_3 loaded, this composite reached a specific capacitance of 232 F g^{-1} at the scanning rate of 5 mV s^{-1} [6]. The drawbacks of previous synthesis methods have been discussed in chapter 4.

Capacitance has been widely used to estimate the electrochemical properties of bismuth oxide. However, bismuth oxide has obvious redox peaks in CV curves and a flat discharge plateau in the charge-discharge curve within the potential range from -1 V to 0 V vs. SHE. All these behaviours of Bi_2O_3 are suited to the definition of Faradaic electrode rather than pseudocapacitor [7, 8]. Therefore, specific capacity (C g^{-1}), instead of specific capacitance (F g^{-1}), is be used to estimate the electrochemical performance of this kind of electrode.

In this work, we synthesized flower like Bi_2O_3-GO by a simple non-toxic chemical reduction method which involves low reaction temperature (60°C) and short reaction time (3h). No toxic chemicals, such as hydrazine, were used during the reaction [9]. This simple preparation procedure allows this material to be synthesized in large scale with low cost. The synthesized Bi_2O_3-GO composite has good electrochemical properties and can be used as electrodes in electrochemical energy storage devices.

5.2 Experimental

5.2.1 Chemicals

Natural graphite flakes (99.8%) and concentrated sulphuric acid (98%) were purchased from VWR International. Reagent grade phosphoric acid (85%), potassium permanganate (99.0%), dihydrogen dioxide (50%), hydrogen chloride ($\geqslant$37%), bismuth (III) nitrate pentahydrate ($\geqslant$98%), sodium hydroxide ($\geqslant$98%), potassium hydroxide (90%) and nitric acid ($\geqslant$69%) used in this work were purchased from Sigma-Aldrich. All chemicals were used without further

purification.

5.2.2 Materials synthesis

Graphene oxide was produced by oxidation and exfoliation procedure following the Hummers method [10]. 3 g of graphite and 8 g of $KMnO_4$ were added into a mixture of 100 mL of H_2SO_4 (98%) and 20 mL H_3PO_3 (85%) solution. This dispersion was left at room temperature with slow stirring to achieve a complete reaction. H_2O_2 was added into this suspension until its colour is turned bright yellow. This suspension was first washed and filtered by 5% HCl and then washed by DI water for several times. Graphene oxide was obtained by drying the prepared slurry in an oven at 60°C for 24 hours.

Bi_2O_3-GO composite was prepared by a modified reduction method following previous work [11]. 0.03 g of prepared graphene oxide was first dispersed into 15 mL of DI water (18 MΩ cm^{-1} resistivity). Then 2.5 mmol $Bi(NO_3)_3$ was dissolved in a mixture solution of 22.5 mL DI water and 2 mL of HNO_3 (67%). 12.5 mL of NaOH (3 M) solution was also prepared. These solutions were mixed together and transferred into a round bottom flask after being pre-heated to 60°C. The reaction was held at 60°C for 3 hours without stirring. The synthesized sample was collected after filtration and washed by DI water for several times. Flower-like Bi_2O_3-GO was obtained after kept the sample in oven at 60°C for 6 hours.

GO without added bismuth nitrate was also synthesized with the same method in order to study the effect of NaOH on GO. 0.03 g GO was dispersed into 15 mL DI water. 35 mL of NaOH (3 M) was added into the GO dispersion. The reaction was hold at 60°C for 3 hours without stirring. NaOH washed GO was obtained after filtering this dispersion, which has been washed by DI water several times.

5.2.3 Sample characterization

The samples were characterized by X-ray diffraction (XRD, RINT Rigaku), Fourier transform infrared spectroscopy (FTIR, Varian 670-IR), Raman spectroscopy (HR800UV, Horiba, Jobin Yvon), scanning electron microscopy (SEM, XL30 ESEM-FEG, Philips), transmission electron microscopy (TEM, JEM-2100, JEOL) and X-ray photoelectron spectroscopy (XPS, Kratos Axis Ultra spectrometer). A potentiostat (Bio-logic Science instruments) was used to analyse the electrochemical behaviour of the composites, via cyclic voltammetry and mea-

surements of the charge/discharge behaviour. Cyclic voltammetry results are used to study the mechanism of the reaction that take during the Faradaic redox reaction of bismuth. A small amount (9 mg) of sample was dispersed in DI water. PTFE (10 mg mL^{-1}) was added as a binding agent with a sample to PTFE weight ratio of 9:1. After obtaining a homogeneous suspension by sonication, some drops were applied to a nickel foam substrate used as the current collector, the working electrode. A three-electrode system was used for the electrochemical properties test. 1.02 mg mixture of Bi_2O_3-GO and PTFE pressed on Ni foam was used as working electrode. A HgO|Hg (mercury-mercury oxide) electrode was used as the reference electrode. A Pt wire was used as the counter electrode and a 6M KOH solution was used as the electrolyte. Current densities are quoted in A g^{-1} here as the true surface area of the electrodes is difficult to determine. Instruments used to characterize the as-prepared Bi_2O_3-GO and GO were described in chapter 3.

5.3 Results and discussion

5.3.1 XRD of Bi_2O_3-GO and GO

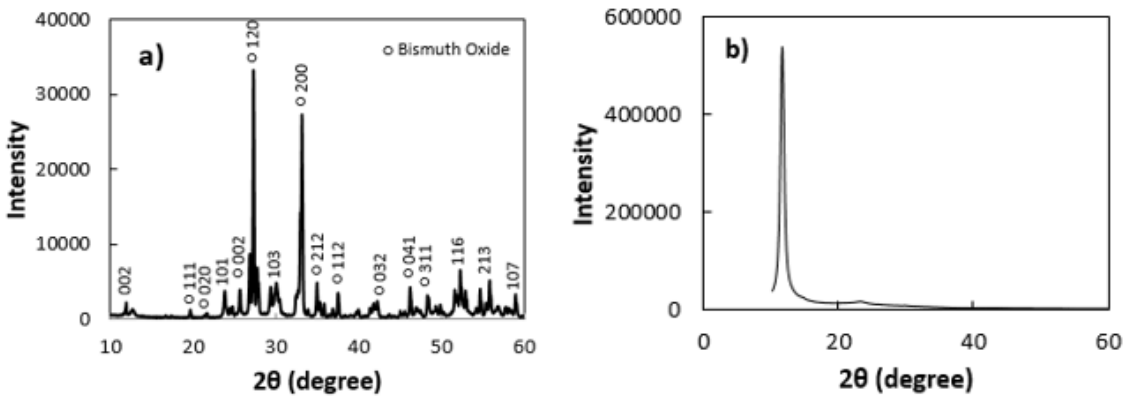

Figure 5.1: X-ray powder diffractogram of a) flower-like Bi_2O_3-GO b) graphene oxide.

Figure 5.1 a) shows the XRD pattern of synthesized flower-like Bi_2O_3 grown on GO. Most peaks, including all the strong peaks, indicate the existence of Bi_2O_3. Three strong peaks which appeared at 27.27°, 32.92°, and 33.12° correspond to the crystal planes of (120), (121), and (200) of Bi_2O_3, respectively. The peak position of all Bi_2O_3 peaks matched the standard value of monoclinic α-Bi_2O_3 phase (Natl. Bur. Stand. (U.S.)), which is normally formed at low temperature. Other relatively weak peaks (appear at 12.91°, 30.24°, 52.23°, 53.28°, 54.44°, 56.86°) indicate the existence of $Bi_2O_2CO_3$ as impurity (Natl. Bur. Stand. (U.S.)).

Since the only carbon source is graphene oxide, during the reduction procedure, small amounts of $Bi(NO_3)_3$ may have reacted with the functional groups attached on graphene oxide and formed $Bi_2O_2CO_3$. The relatively low intensity of $Bi_2O_2CO_3$ peaks indicates the small amount of $Bi_2O_2CO_3$ present. In addition, the small peak appeared at 11.88° corresponds to the NaOH washed graphene oxide. By adding NaOH in the reaction, the epoxy groups in graphene oxide were destroyed and hydroxyl groups were generated [12]. These generated hydroxyl groups may further react with $Bi(NO_3)_3$ and form Bi_2O_3 and $Bi_2O_2CO_3$ on graphene sheets. Therefore graphene will be attached to as-prepared Bi_2O_3 and linked them together. Figure 5.1 b shows the XRD pattern of graphene oxide solely. A strong peak at 11.88°, proves the successful formation of graphene oxide. The distance between graphene oxide sheets was estimated at 0.744 nm based on the Bragg's law [13]. The small peak at around 26° indicates the existence of graphite, which failed to be oxidised to graphene oxide.

The formation of Bi_2O_3 and $Bi_2O_2CO_3$, which is based on some previous findings in literature [14, 15], is proposed as:

$$Bi(NO_3)_3 \cdot 5H_2O + HNO_3 + H_2O \rightarrow BiONO_3 \tag{5.1}$$

$$BiONO_3 + OH\text{-} \rightarrow Bi_2O_3 \cdot xH_2O + NO_3^- \tag{5.2}$$

$$Bi_2O_3 \cdot xH_2O \rightarrow Bi_2O_3 + xH_2O \tag{5.3}$$

$$BiONO_3 + GO \rightarrow Bi_2O_2CO_3 + NO_3^- \tag{5.4}$$

Bismuth nitrate was first dissolved in nitric acid. Bismuth oxynitrate was formed after adding sodium hydroxide to adjust the pH value of the solution to 12. Bismuth oxynitrate was further reacted with sodium hydroxide and formed bismuth oxide hydrate. During the drying process, bismuth oxide was formed after dehydration [14]. In this reaction, some of the bismuth ions may react with the functional groups attached on graphene oxide and form bismuth subcarbonate [15].

5.3.2 Raman and FTIR of GO and Bi_2O_3-GO

FTIR (as in Figure 5.2 a)) was used to identify the functional groups in as-prepared GO and Bi_2O_3-GO. In the FTIR spectra of GO, peaks appeared at 1060 cm^{-1}, 1245 cm^{-1}, 1361 cm^{-1}, 1720 cm^{-1} are assigned to the in phase C-C-O stretching, out of phase C-O-C stretching, C-

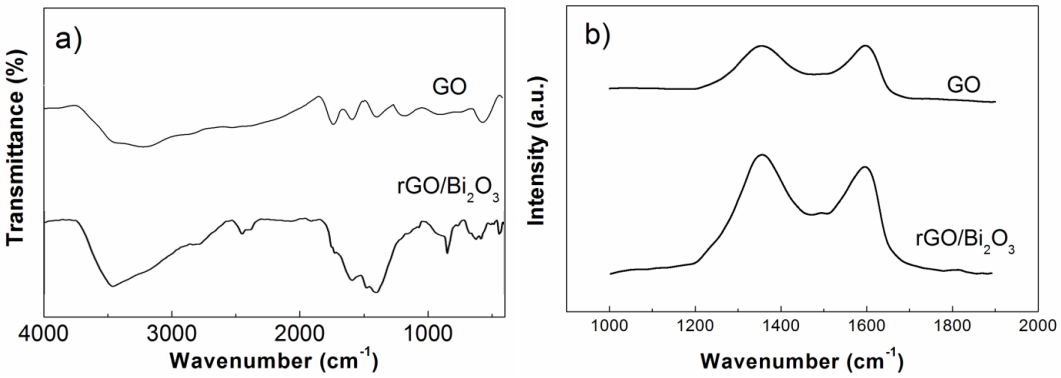

Figure 5.2: a) FTIR of GO and Bi_2O_3-GO b) Raman spectroscopy of GO and Bi_2O_3-GO.

OH bending, C=O stretching, respectively [16, 17]. The peak at 1600 cm^{-1} correspond to the skeletal vibrations of unoxidized graphitic domains [16]. The broad peak from 3000 to 3600 cm^{-1} is contributed by –OH stretching vibration [18]. In the FTIR spectra of Bi_2O_3-GO, the peak appeared at 420 cm^{-1} assigned to the Bi-O stretching mode [19]. The broad peak at around 600 to 620 cm^{-1} indicates the Bi-O stretching vibration in BiO_6 octahedral unit while the sharp peak at 860 cm^{-1} indicates the symmetrical stretching vibration of the Bi-O bond in BiO_3 pyramidal unit [20]. In addition, the peaks in the region of 1163-1832 cm^{-1} are related to the asymmetrical Bi-O bond in BiO_3 unit [21]. The peak at 3448 cm^{-1} is due to the OH^- in this Bi_2O_3-GO sample [22].

Raman spectroscopy (as in Figure 5.2 b)) was used to analyse the defects and disorder density in GO and Bi_2O_3-GO samples and study the structural changes from GO to GO in Bi_2O_3-GO. For both the GO and Bi_2O_3-GO samples, two peaks were observed in the energy range from 1000 cm^{-1} to 1900 cm^{-1}. One peak at 1580 cm^{-1} (G band) is due to the first order scattering of the E^2g mode, which is caused by the in phase vibration of graphite lattice [23, 24]. The peak at 1360 cm^{-1} is contributed by the presence of defects in carbon materials [25]. The peak intensity ratio I_D/I_G is changed from 0.87 in GO to 1.10 in Bi_2O_3-GO, which indicates decrease of the average size of sp^2 domains. This increased I_D/I_G ratio from GO to rGO has been reported previously in literature [26] and explained in terms of the creation of new graphitic domains in rGO that are smaller in size but larger in quantity compared with those in GO.

5.3.3 XPS study of GO and Bi_2O_3-GO

To further study chemical changes from GO to GO in Bi_2O_3-GO, XPS spectra of C1s was used to monitor the structural and chemical composition changes from GO to rGO. The peaks appeared at 284.5 eV in both the Figure 5.3 a) and b) are assigned to the C-C and C=C stretch-

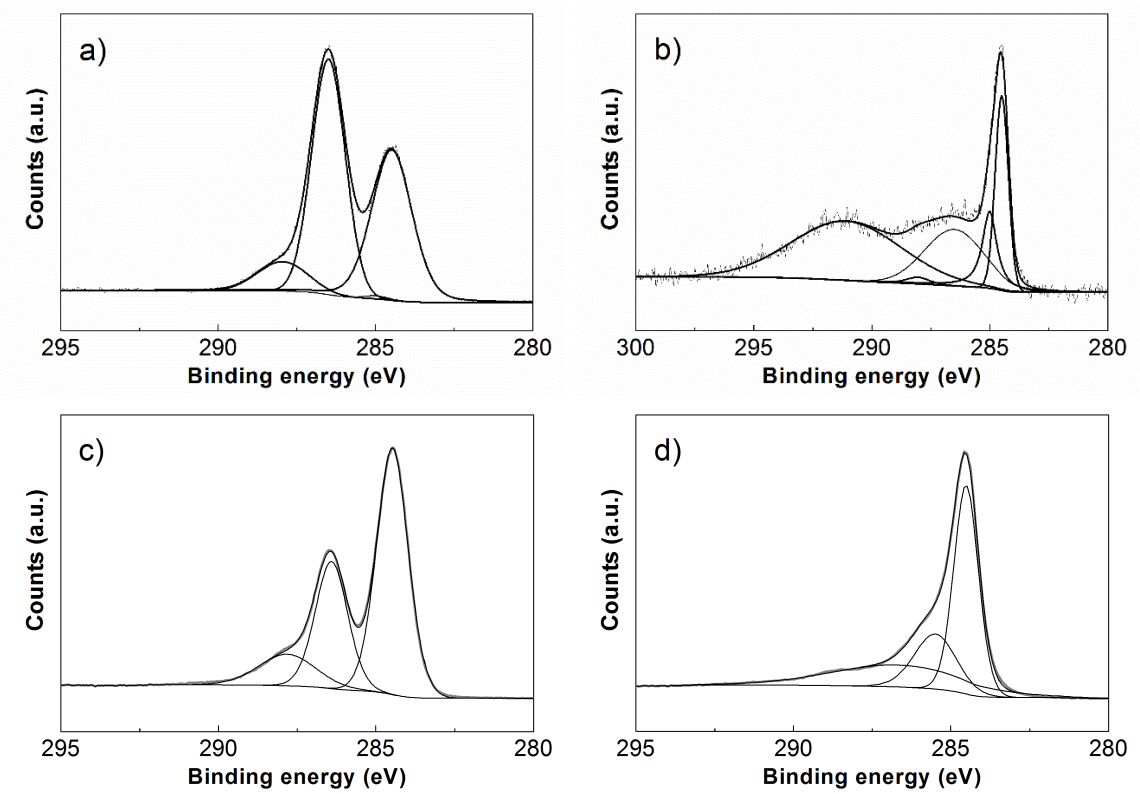

Figure 5.3: C1s XPS spectra of a) GO and b) Bi_2O_3-GO c) GO washed by NaOH d) GO washed by hydrazine.

ing, which indicates the existence of sp^2 graphite carbon [25, 27]. With the chemical shift of +0.5 eV, +2.0 eV and +3.5 eV, the peaks at 285.0 eV, 286.5 eV and 288.0 eV are assigned to C-H, C-O and C=O functional groups, respectively [28, 29]. The peak appeared at 291.1 eV in Figure 5.3 b) is caused by the plasmon/shake up satellite (π-π* transition) of graphitic carbon [30]. The graphite peak in Bi_2O_3-GO XPS spectra is more dominant compared to this peak in GO spectra. This might be because the NaOH destroys the epoxy groups in graphene oxide and forms hydroxyl groups. To further study the affect of NaOH on graphene oxide, XPS of GO washed by NaOH was also presented in Figure 5.3 c). Three main peaks are observed in the XPS spectra of GO washed by NaOH. The peaks appeared at 284.5 eV, 286.5 eV and 288.0 eV are corresponding to C-C and C=C stretching, C-O and C=O functional groups, respectively. These peaks have the same position as XPS spectra of graphene oxide. However, the C-O and C=O peaks are less dominant, which indicates that less epoxy groups are left in graphene oxide sheets after washing by NaOH. The XPS spectra of graphene oxide sheets washed by hydrazine are also studied, see Figure 5.3 d). A very strong graphite carbon appeared at 284.5 eV, is assigned to the C-C and C=C stretching [25, 27]. Compared to the NaOH washed sample, hydrazine washed graphene oxide has weak C-O and C=O peaks, which indicates a more complete reduction.

5.3.4 SEM images of Bi_2O_3-GO

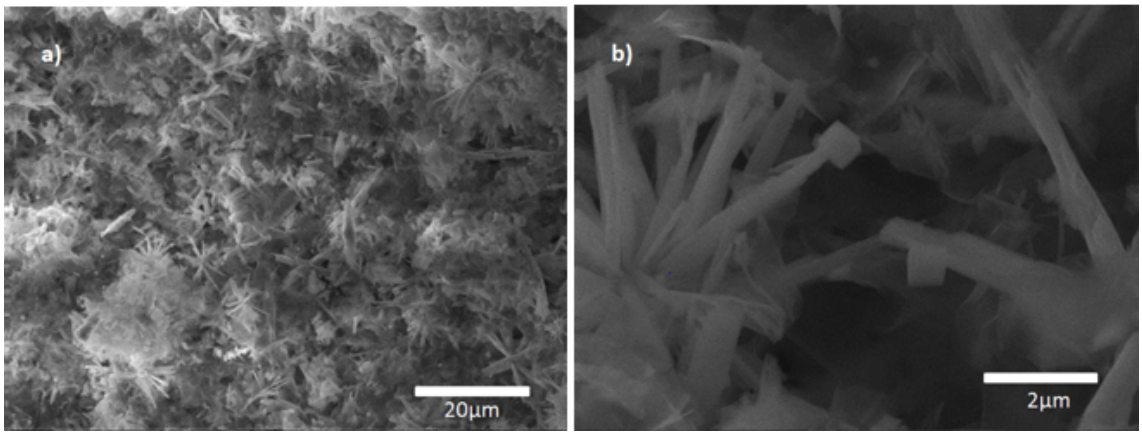

Figure 5.4: SEM figures of flower-like Bi_2O_3-GO a) X1200 b) X12000 magnification.

In figure 5.4, SEM images show that prepared Bi_2O_3-GO composites have a self-assembled flower-like structure. Each leaf of this flower-like Bi_2O_3 has a length $\sim 4\mu$m. Corrugated sheets attached to Bi_2O_3 are reduced graphene oxide sheets. Beside flower-like Bi_2O_3, there are also some Bi_2O_3 particles with cubic structure (Figure 5.4 b)). These Bi_2O_3 cubic particles are believed to be the initial nuclei of the self-assembled flower-like Bi_2O_3 leaf. Some of these cubic particles have stayed separated in the solution and failed to assemble into the flower-like structure.

5.3.5 TEM images of Bi_2O_3-GO

SAED (selected area electron diffraction) and EDS (energy dispersive X-ray spectroscopy) were used to further confirm the crystal planes and elemental composition of prepared Bi_2O_3-GO composites. Figure 5.5 a) shows an image of Bi_2O_3-GO. Graphene oxide sheets, with a transparent colour are wrapped on the bismuth oxide stick. A SAED of this sample is done on the specific area, which is labelled with a red cycle. The diffraction rings with increased

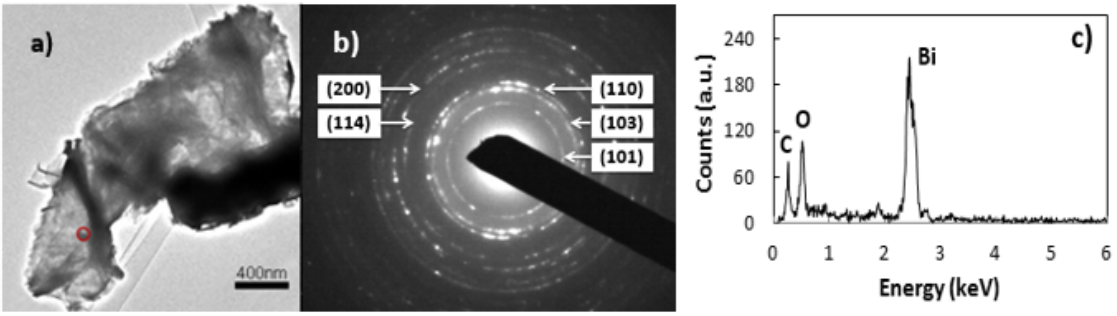

Figure 5.5: a) TEM image of Bi_2O_3-GO b) SAED of Bi_2O_3-GO c) EDS result of Bi_2O_3-GO.

diameters in Figure 5.5 b) correspond to the crystal planes of (101), (103), (110), (114) and (200) of Bi_2O_3 (Natl. Bur. Stand. (U.S.)). The ring-shaped diffraction pattern indicates that this material has a nano-crystallite structure. The EDS spectra (Figure 5.5 c)) show strong Bi, C and O peaks. Bi and O peaks are originated from Bi_2O_3, C peak is attribute to carbon film, reduced graphene oxide and $Bi_2O_3CO_3$. These data are in agreement with XRD results (Figure 5.1 a)).

5.3.6 Electrochemical behaviour of Bi_2O_3-GO composite

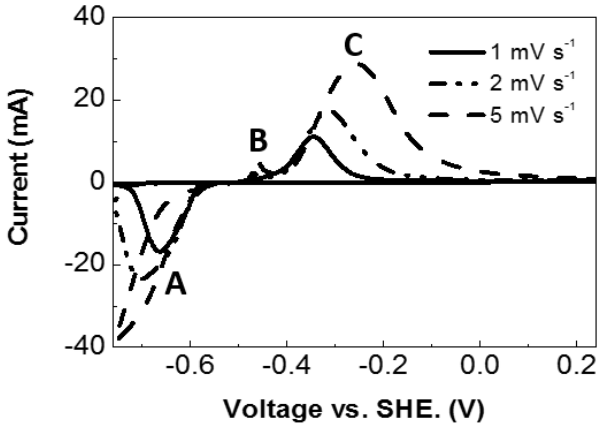

Figure 5.6: Cyclic voltammetry results of Bi_2O_3-GO composite.

Cyclic voltammetry was used to study the reaction of the Bi_2O_3-GO composite material in a voltage range of 0.24 V to -0.76 V vs. SHE (standard hydrogen electrode) as shown in Figure 5.6. Three peaks with similar shapes were observed in this voltage range with different scanning rates from 1 mV s^{-1} to 5 mV s^{-1}. These peaks are due to the redox reaction that happens during the electrochemical test, which involves the oxidation state changes of Bi between 0 and +3 [11, 31]. Peak A appeared at $\sim$ -0.65 V corresponding to the reduction reaction from bismuth with oxidation state of three to metallic bismuth. peak B and C appeared at -0.45 V and -0.3 V correspond to the oxidation reaction from metallic bismuth to bismuth with oxidation state of three. These redox peaks in the CV curves can be explained by the following equations [11]:

for peak A

$$Bi_2O_3 + 2OH^- \rightarrow 2BiO_2^- + H_2O \tag{5.5}$$

$$BiO_2^- + e^- \rightarrow BiO_2^{2-} \tag{5.6}$$

$$2H_2O + 3BiO_2^{2-} \iff 2BiO_2^- + 4OH^- + Bi^{(0)} \tag{5.7}$$

$$Bi^{(0)} \rightarrow Bi_{metal} \tag{5.8}$$

for peaks B and C

$$Bi_{metal} \rightarrow Bi^{+} + e^{-} \tag{5.9}$$

$$3Bi^{+} \Longleftrightarrow Bi^{3+} + 2Bi_{metal} \tag{5.10}$$

$$3OH^{-} + Bi^{3+} \rightarrow Bi(OH)_3 \tag{5.11}$$

$$Bi(OH)_3 \rightarrow BiOOH + H_2O \tag{5.12}$$

$$BiOOH + OH^{-} \rightarrow BiO_2^{-} + H_2O \tag{5.13}$$

Reduction reaction of Bi from +3 to 0 oxidation state happens in peak A. The first step in the reduction reaction consists of a partial dissolution of Bi_2O_3 into BiO_2^- [32]. Then this BiO_2^- is further reduced into Bi metal [11]. Peak B and C illustrate the oxidation reactions of Bi into BiO_2^- [31]. Small peaks (peak B) in Figure 5.6 could be due to the oxidation of some untransformed $Bi^{(0)}$ in the reduction process [10, 29]. From these equations, Bi_2O_3 undergoes phase transformations during these redox reactions [8]. In addition, the CV curves have redox wave shapes, instead of rectangular shapes, which suggest that this Bi_2O_3-GO composite is a non-capacitive faradaic electrode [7, 8].

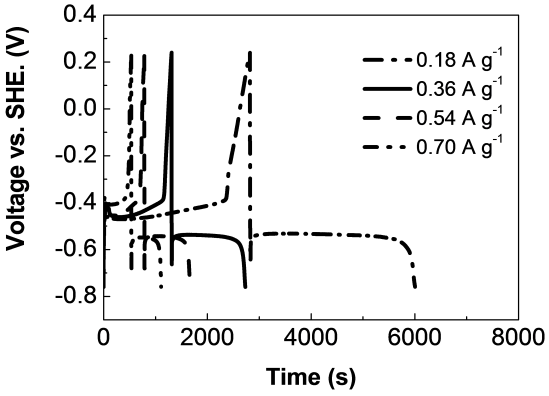

Figure 5.7: Charge/discharge behaviour of Bi_2O_3-GO composite.

To analyse the electrochemical properties of the prepared Bi_2O_3-GO, the charge/discharge behaviours were studied at constant currents (of 0.18 A g^{-1}, 0.36 A g^{-1}, 0.54 A g^{-1} and 0.7 A g^{-1}) within a voltage range from 0.24 V to -0.76 V vs. SHE, shown in Figure 5.7. The discharging process normally contains two steps. A sudden voltage drop due to the internal resistance and a flat platform due to the reversible faradaic reaction of Bi_2O_3 [2]. In the flat discharge

plateau, faradaic reaction takes place and leads to phase transformation of Bi_2O_3, which corresponds to the reactions that happened in peak C, shown in Figure 5.7. The reaction that takes place in the flat plateau of the charging process corresponds to peak A in Figure 5.6. The plateaus in these charge/discharge curves further confirm the battery-like behaviour of this material [7]. As the energy storage mechanism of this as-prepared Bi_2O_3-GO is a non-capacitive faradaic, specific capacity in C g^{-1}, rather than specific capacitance F g^{-1}, is believed to be the appropriate way to measure the charge stored in this electrode [33]. Specific capacity is calculated according to the following equation 5.14 [33]:

$$C_s = \frac{i \times \Delta t}{m} \tag{5.14}$$

where, C_s is the specific capacity (C g^{-1}), i is the current (mA), Δt is the discharging time (s) and m is the mass of active materials (mg). Different current density values, 0.18 A g^{-1}, 0.36 A

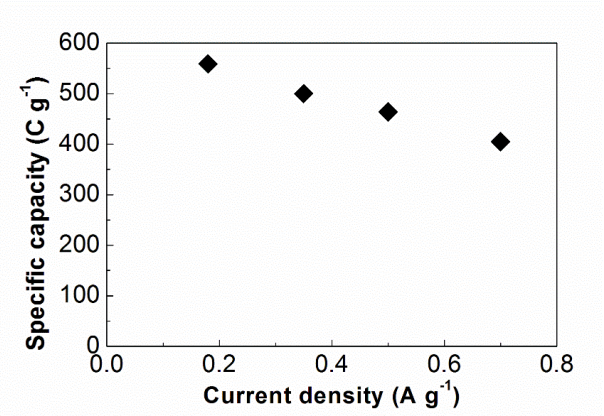

Figure 5.8: The calculated specific capacity of Bi_2O_3-GO for different current densities.

g^{-1}, 0.54 A g^{-1} and 0.70 A g^{-1}, were used to test the charge/discharge behaviours of this sample. The calculated specific capacity values for different current density are presented in Figure 5.8. Based on the calculation, Bi_2O_3-GO has a specific capacity value as high as 559 C g^{-1} at the current density of 0.18 A g^{-1}. With the increase of current density, the specific capacity values decreased from 559 C g^{-1} at 0.18 A $g^{-1}$to 405 C g^{-1} at 0.7 A g^{-1}. This is because of the increased current density, the intercalation of ions only happen at the surface of activated material [31]. The reduced rates of ion diffusion and charge transfer cause the decline of capacity [34, 35]. However, at the current density of 0.7 A g^{-1}, this Bi_2O_3-GO still has a very large specific capacity value of 405 C g^{-1}. Even with a 27% decrease of capacity from 0.18 A g^{-1} to 0.7 A g^{-1}, the achieved specific capacity is still much higher than any previously reported results [2, 3].

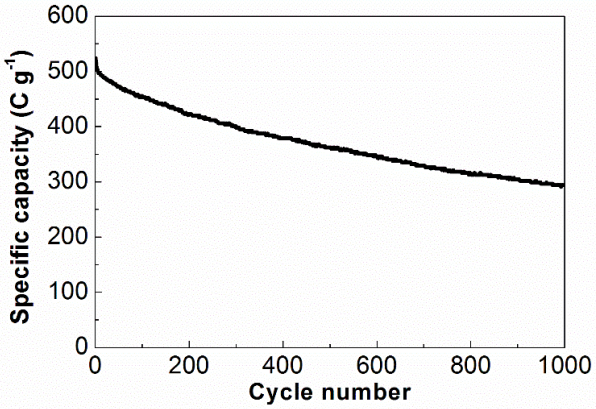

Figure 5.9: Cycling performances of Bi_2O_3-GO composite.

Cycling performances of Bi_2O_3-GO composite were tested by repeat of the charge/discharge tests 1000 times. Figure 5.9 shows the specific capacity changes with cycling numbers. After 1000 cycles, Bi_2O_3-GO has still kept a specific capacity value of 290 C g^{-1}, which is 57% of the initial capacity value. This capacity value after 1000 cycles is still much higher than previously reported value of rGO/Bi_2O_3 [4]. The continuous decreasing of specific capacitance could be caused by the loss of active materials due to some loss of adhesion to the current collector, Ni foam. In addition, degradation and dissolution of Bi_2O_3 into the electrolyte solution may also contribute to the continuous deterioration during the cycling tests [36].

5.4 Conclusion

In summary, Bi_2O_3-GO composites are synthesized through a low cost non toxic chemical reduction method with low reaction temperature (60°C) and short reaction time (3hrs). Our fast but low energy requirement synthesis method is promising for large-scale production of this material. This prepared Bi_2O_3-GO composite material achieved high specific capacity of 559 C g^{-1} at a current density of 0.18 A g^{-1}. Even with the current density increased to 0.7 A g^{-1}, the prepared sample still has a specific capacity of 405 C g^{-1}. With high specific capacity and non-toxic nature, this composite material shows huge potential to be used as the electrode in the next generation of electrochemical energy storage devices.

References

[1] N. M. Leonard, L. C. Wieland, and R. S. Mohan, “Applications of bismuth(III) com-

pounds in organic synthesis," *Tetrahedron*, vol. 58, pp. 8373–8397, 2002.

[2] T. P. Gujar, V. R. Shinde, C. D. Lokhande, and S. H. Han, "Electrosynthesis of Bi_2O_3 thin films and their use in electrochemical supercapacitors," *Journal of Power Sources*, vol. 161, pp. 1479–1485, 2006.

[3] F. Zheng, G. Li, Y. Ou, Z. Wang, C. Su, and Y. Tong, "Synthesis of hierarchical rippled Bi_2O_3 nanobelts for supercapacitor applications," *Chemical Communications*, vol. 46, pp. 5020–5023, 2010.

[4] M. Ciszewski, A. Mianowski, P. Szatkowski, G. Nawrat, and J. Adamek, "Reduced graphene oxide–bismuth oxide composite as electrode material for supercapacitors," *Ionics*, vol. 557-563, p. 21, 2015.

[5] K. Gopalsamy, Z. Xu, B. Zheng, T. Huang, L. Kou, X. Zhao, and C. Gao, "Bismuth oxide nanotubes-graphene fiber-based flexible supercapacitors," *Nanoscale*, vol. 6, pp. 8595–8600, 2014.

[6] D. Yuan, J. Zeng, N. Kristian, Y. Wang, and X. Wang, "Bi_2O_3 deposited on highly ordered mesoporous carbon for supercapacitors," *Electrochemistry Communications*, vol. 11, pp. 313–317, 2009.

[7] T. Brousse, D. Belanger, and J. W. Long, "To be or not to be pseudocapacitive?" *Journal of Electrochemistry Society*, vol. 162, pp. 5185–5189, 2015.

[8] A. Veronica, S. Patrice, and D. Bruce, "Pseudocapacitive oxide materials for high-rate electrochemical energy storage," *Energy & Environmental Science*, vol. 7, pp. 1597–1614, 2014.

[9] L-L. Dong, W-G. Chen, N. Deng, and C-H. Zheng, "A novel fabrication of graphene by chemical reaction with a green reductant," *Chemical Engineering Journal*, vol. 306, pp. 754–762, 2016.

[10] W. S. Hummers and R. E. Offman, "Preparation of graphite oxide," *Journal of American Chemistry Society*, vol. 80, pp. 1339–1339, 1958.

[11] V. Vivier, A. Regis, G. Sagon, J. Y. Nedelec, L. T. Yu, and C. Cachet-Vivier, "Cyclic voltammetry study of bismuth oxide Bi_2O_3 powder by means of a cavity microelectrode coupled with Raman microspectrometry," *Electrochimica Acta*, vol. 46, pp. 907–914, 2001.

[12] D. Lee and J. Seo, "Three-dimensionally networked graphene hydroxide with giant pores

and its application in supercapacitors," *Scientific Reports*, vol. 4, pp. 7419(1–6), 2014.

[13] Y. Waseda, E. Matsubara, and K. Shinoda, *X-ray diffraction crystallography*. Heidelberg: Springer, 2011.

[14] X. Luan, J. Jiang, Q. Yang, M. Chen, M. Zhang, and L. Li, "Facile synthesis of bismuth oxide nanoparticles by a hydrolysis solvothermal route and their visible light photocatalytic activity," *Environmental Engineering and Management Journal*, vol. 14, pp. 703–707, 2015.

[15] Y. Liu, Z. Wang, B. Huang, K. Yang, X. Zhang, X. Qin, and Y. Dai, " Preparation, electronic structure, and photocatalytic properties of $Bi_2O_2CO_3$ nanosheet," *Applied Surface Science*, vol. 257, pp. 172–175, 2010.

[16] Y. Si and E. T. Samulski, "Synthesis of water soluble graphene," *Nano Letters*, vol. 8, pp. 1679–1682, 2008.

[17] W. G. F. D. L. Vien, N. B. Colthup and J. G. Graselli, *The handbook of infrared and Raman characteristic frequencies of organic molecules*. San Diego: Academic Press, 1991.

[18] E. Y. Choi, T. H. Han, J. Hong, J. E. Kim, S. H. Lee, H. W. Kim, and S. O. Kim, "Noncovalent functionalization of graphene with end-functional polymers," *Journal of Materials Chemistry*, vol. 20, pp. 1907–1912, 2010.

[19] R. Irmawati, M. N. Noorfarizan Nasriah, Y. H. Taufiq-Yap, and S. B. Abdul Hamid, "Characterization of bismuth oxide catalysts prepared from bismuth trinitrate pentahydrate: influence of bismuth concentration," *Catalysis Today*, vol. 93-95, pp. 701–709, 2004.

[20] R. Punia, R. S. Kundu, J. Hooda, S. Dhankhar, S. Dahiya, and N. Kishore, "Effect of Bi_2O_3 on structural, optical, and other physical properties of semiconducting zinc vanadate glasses," *Journal of Applied Physics*, vol. 110, pp. 033 527(1–6), 2011.

[21] Y. B. Saddeek, G. Y. Mohamed, H. S. Shokry Hassan, A. M. A. Mostafa, and G. Abd elfadeel, "Effect of gamma irradiation on the FTIR of cement kiln dust–bismuth borate glasses," *Non-Crystalline Solids*, vol. 419, pp. 110–117, 2015.

[22] W. Li, "Facile synthesis of monodisperse Bi_2O_3 nanoparticles," *Materials Chemistry and Physics*, vol. 99, pp. 174–180, 2006.

[23] L. G. Cancado, A. Jorio, E. H. Ferreira, F. Stavale, C. A. Achete, R. B. Capaz, M. V.

Moutinho, A. Lombardo, T. S. Kulmala, and A. C. Ferrari, "Quantifying defects in graphene via Raman spectroscopy at different excitation energies," *Nano Letters*, vol. 11, pp. 3190–3196, 2011.

[24] K. N. Kudin, B. Ozbas, H. C. Schniepp, and R. K. Prud'homme, "Raman spectra of graphite oxide and functionalized graphene sheets," *Nano Letters*, vol. 8, pp. 36–41, 2008.

[25] K. Krishnamoorthy, M. Veerapandian, K. Yun, and S. J. Kim, "The chemical and structural analysis of graphene oxide with different degrees of oxidation," *Carbon*, vol. 53, pp. 38–49, 2013.

[26] S. Stankovich, D. A. Dikin, R. D. Piner, K. A. Kohlhaas, A. Kleinhammes, Y. Jia, Y. Wu, S. T. Nguyen, and R. S. Ruoff, "Synthesis of graphene-based nanosheets via chemical reduction of exfoliated graphite oxide," *Carbon*, vol. 45, pp. 1558–1565, 2007.

[27] C. Chua and M. Pumera, "Renewal of sp^2 bonds in graphene oxides via dehydrobromination," *Journal of Materials Chemistry*, vol. 22, pp. 23 227–23 231, 2012.

[28] S. Yumitori, "Correlation of C1s chemical state intensities with the O1s intensity in the XPS analysis of anodically oxidized glass like carbon samples," *Journal of Materials Science*, vol. 35, pp. 139–146, 2000.

[29] A. Kolmakov, D. A. Dikin, L. J. Cote, J. Huang, M. K. Abyaneh, M. Amati, L. Gregoratti, S. Gunther, and M. Kiskinova, "Graphene oxide windows for in situ environmental cell photoelectron spectroscopy," *Nature Nanotechnology*, vol. 6, pp. 651–657, 2011.

[30] F. Barroso-Bujans, F. Fernandez-Alonso, J. A. Pomposo, E. Enciso, J. L. G. Fierro, and J. Colmenero, "Tunable uptake of poly(ethylene oxide) by graphite-oxide-based materials," *Carbon*, vol. 50, pp. 5232–5241, 2012.

[31] S. Wang, C. Jin, and W. Qian, "Bi_2O_3 with activated carbon composite as a supercapacitor electrode," *Journal of Alloys and Compounds*, vol. 615, pp. 12–17, 2014.

[32] V. Vivier, C. C. Vivier, S. Mezaille, B. L. Wu, C. S. Cha, J. Nedelec, M. Fedoroff, D. Michel, and L. T. Yu, "Electrochemical study of Bi_2O_3 and $Bi_2O_2CO_3$ by means of a cavity microelectrode I. Observed phenomena and direct analysis of results," *Journal of the Elecrochemical Society*, vol. 147, pp. 4252–4262, 2000.

[33] M. Liu, Y. Fu, H. Ma, T. Wang, C. Guan, and K. Hu, "Flower-like manganese-cobalt oxysulfide supported on Ni foam as a novel faradaic electrode with commendable per-

formance," *Electrochimica Acta*, vol. 191, pp. 916–922, 2016.

[34] D. Qu, L. Wang, D. Zheng, L. Xiao, B. Deng, and D. Qu, "An asymmetric supercapacitor with highly dispersed nano-Bi_2O_3 and active carbon electrodes," *Journal of Power Sources*, vol. 269, pp. 129–135, 2014.

[35] D. N. Futaba, K. Hata, T. Yamada, T. Hiraoka, Y. Hayamizu, Y. Kakudate, O. Tanaike, H. Hatori, M. Yumura, and S. Iijima, "Shape-engineerable and highly densely packed single-walled carbon nanotubes and their application as super-capacitor electrodes," *Nature Materials*, vol. 5, pp. 987–994, 2006.

[36] M. Kerlau, M. Marcinek, V. Srinivasan, and R. M. Kostecki, "Studies of local degradation phenomena in composite cathodes for lithium-ion batteries," *Electrochimica Acta*, vol. 52, pp. 5422–5429, 2007.

Chapter 6

Nanosized $Bi_2O_2CO_3$ particles decorated on graphene for electrode used in the energy storage devices

6.1 Introduction

Carbon materials, such as active carbon, carbon fibre, carbon nanotube and graphene, are considered as good electrode materials for electrochemical double layer capacitor (EDLC) due to their large surface area, high electrical conductivity and good chemical stability [1–4]. However, EDLC suffers from the low energy density compared to batteries [5]. To increase the energy density of electrode materials, transition oxides, in which fast and reversible faradic processes take place, have been considered to be incorporated with carbon materials, especially graphene [6, 7]. Among them, transition metal oxides with nanosized structure have attract tremendous attention [7–10].

By merging reduced graphene oxide (rGO) with nanosized transition metal oxide particles, high surface area and readily accessible mesoporous electrode materials can be obtained [11, 12]. Hydrothermal synthesis, which requires autoclave and high reaction temperature, is generally used to prepare nanosized composite materials [13, 14]. The drawbacks of previous synthesis methods have been discussed in chapter 4.

In this work, we proposed a novel one step method to prepare rGO/$Bi_2O_2CO_3$ nanocomposite material. $Bi_2O_2CO_3$, as one of the bismuth components, shares the non-toxic and environmental friendly properties of bismuth [15]. In this work, we successfully synthesized nanosized

$Bi_2O_2CO_3$ particles at room temperature within 3 hours. $Bi_2O_2CO_3$ particles uniformly decorated on the reduced graphene oxide surface. The presence of nanosized $Bi_2O_2CO_3$ (5-10 nm) particles help this composite material to achieve a high electrical conductivity and electrochemical storage capacity.

6.2 Experimental

6.2.1 Chemicals

Natural graphite flakes (325 mesh, 99.8%) and analytical reagent grade sulphuric acid (98%) were purchased from VWR International. Reagent grade phosphoric acid (85%), potassium permanganate (99.0%), dihydrogen dioxide (30 wt%), hydrogen chloride (>37%), nitric acid (>69%), bismuth (III) nitrate pentahydrate (>98%) and anhydrous dimethyl sulfoxide (>99.9%) were purchased from Sigma-Aldrich. All chemicals were used without further purification.

6.2.2 Material synthesis

Graphene oxide was prepared by oxidation and exfoliation graphite following a modified Hummer's method [16]. 3 g of graphite flake and 8 g of $KMnO_4$ were added into a mixture of 100 mL of H_2SO_4 (98%) and 20 mL of H_3PO_3 (85%). This reaction was kept at room temperature for 3 days with slow stirring. H_2O_2 was added into this dispersion until it became a bright yellow colour. Graphene oxide was obtained after this mixture was filtered by 5% of HCl and then DI water for several times. 0.06 g of prepared graphene oxide was dispersed in a 10 mL of DMSO (>99.9%) solution. 0.3 mmol of bismuth nitrate (>98%) was dispersed in another sample vail with 10 mL of DMSO solution. Sonication was used for both solutions to obtain a homogeneous suspension. 4 mL hydrazine was added after these two solution were mixed together spontaneously. This reaction was held at room temperature with a stirring rate of 500 rpm for 3 hours.

6.2.3 Sample characterization

The samples are characterized by X-ray diffraction (XRD, RINT Rigaku), Fourier transform infrared spectroscopy (FTIR, Varian 670-IR), Raman spectroscopy (HR800UV, Horiba, Jobin

Yvon) and scanning electron microscopy (SEM, XL30 ESEM-FEG, Philips), transmission electron microscopy (TEM, JEM-2100, JEOL). A potentiostat (Bio-logic Science instruments) is used to analyse the electrochemical behaviour of the composites, via cyclic voltammetry and measurement of the charge/discharge behaviours. Cyclic voltammetry results are used to study mechanism of the reaction taking place during the Faradaic redox reaction of bismuth. A small amount (9 mg) of sample was dispersed in DI water. PTFE (10 mg mL^{-1}) was added as a binding agent with a sample to PTFE weight ratio of 9:1. After obtaining a homogeneous suspension by sonication, some drops were applied to a nickel foam substrate used as the current collector, working electrode. A three-electrode system was used for the electrochemical properties test. Mixture of rGO/Bi and PTFE pressed on Ni foam was used as working electrode. A HgO|Hg (mercury-mercury oxide) electrode was used as the reference electrode. A Pt wire was used as the counter electrode and a 6M KOH solution was used as the electrolyte. Current densities are quoted in A g^{-1} here as the true surface area of the electrodes is difficult to determine.

Instruments used to characterize the rGO/$Bi_2O_2CO_3$ and GO were described in chapter 3.

6.3 Results and discussion

6.3.1 XRD of rGO/$Bi_2O_2CO_3$ composite material

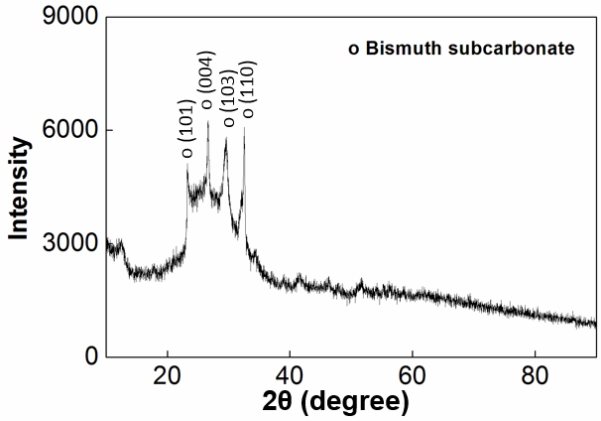

Figure 6.1: X-ray powder diffractogram of rGO/$Bi_2O_2CO_3$.

The XRD study was carried out to analyse the crystalline structure of as-prepared rGO/$Bi_2O_2CO_3$ composite. Four strong peaks were observed in this XRD pattern. Peaks appeared at 23.90°, 26.03°, 30.24° and 32.69° are correspond to the (101), (004), (103) and (110) diffraction plane of bismuth subcarbonate, respectively (Natl. Bur. Stand. (U.S.)). A broad peak at around 24°

to 30° is due to reduced graphene sheets, which was exfoliated into individual layers and then agglomerated into a powder form [17]. A small peak that appeared at 12.02° indicates the existence of graphene oxide. This shows that GO material was reduced by hydrazine, but there are still some oxygen functional groups attached on the graphene sheets.

6.3.2 FTIR and Raman spectroscopy of GO and rGO/$Bi_2O_2CO_3$

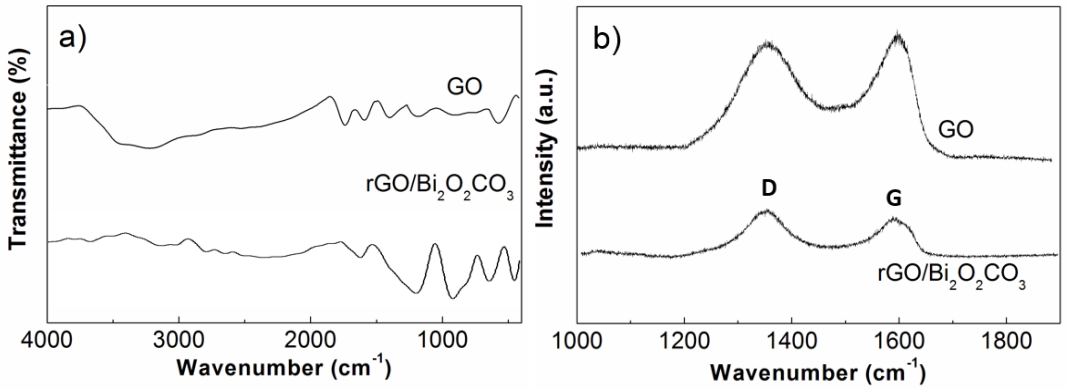

Figure 6.2: a) FTIR of GO and rGO/$Bi_2O_2CO_3$ b) Raman spectroscopy of GO and rGO/$Bi_2O_2CO_3$

FTIR spectra of GO and rGO/$Bi_2O_2CO_3$ are presented in Figure 6.2 a). The transmittance is recorded in the wavenumber range from 400 cm^{-1} to 1000 cm^{-1}. In FTIR spectra of GO (Figure 6.2 a)), peaks at 1060 cm^{-1}, 1245 cm^{-1}, 1361 cm^{-1} and 1720 cm^{-1} are assigned to the presence of C-O stretching, out of phase C-O-C, C-OH bending and C=O in carboxylic acid and carbonyl moieties, respectively [18]. The peak at 1600 cm^{-1} is due to the skeletal vibrations of unoxidized graphitic domains [18]. The broad peak at 3000 cm^{-1} to 3600 cm^{-1} is due to the existence of O-H stretching by intercalated water [19, 20]. More peaks at low frequencies were observed for rGO/$Bi_2O_2CO_3$. These peaks appeared at 436 cm^{-1} and 629 cm^{-1} are assigned to the Bi-O bending and stretching vibrations in the BiO_6 octahedral structure [21–23]. The peaks at 848 cm^{-1} and 906 cm^{-1} are due to the bending modes of triangular CO_3 group [24]. A broad peak at 1188 cm^{-1} is related to the Bi-C vibration [25]. The peak appeared at 1612 cm^{-1} is due to the asymmetrical Bi-O bond in the BiO_3 unit [26]. No obvious peaks, which are assigned to the C-O, C-OH and C=O, were found in the 1000 cm^{-1} to 1720 cm^{-1}. In addition, the O-H stretching peak at around 3000 cm^{-1} to 3600 cm^{-1} for rGO/$Bi_2O_2CO_3$ composite is less obvious compared to that peak in the FTIR curve of GO. This suggests that by using hydrazine as the reducing agent, the functional groups attached to the graphene oxide sheets were reduced. To study the carbon structure changes, Raman spectroscopy was also used to further

confirm the reduction from GO to rGO. The Raman spectra of GO and rGO/$Bi_2O_2CO_3$ within the wavenumber range from 1000 cm^{-1} to 1900 cm^{-1} is presented in Figure 6.2 b). For both GO and rGO/$Bi_2O_2CO_3$, two obvious peaks were observed in this wavenumber range. The peak that appeared at 1580 cm^{-1} (G band) corresponds to the first order scattering of the E2g mode from pristine graphite [27]. The peak at 1360 cm^{-1} (D band) resulted from the defects in carbon materials [28], which corresponds to the breathing modes of sp^2 atoms in rings [29]. The ratio of D and G peak intensity can be used to represent the oxidation level of the carbon materials [28]. The decrease in the I_D/I_G ratio indicates an increase in oxidation level of the material [28]. However, the I_D/I_G ratio was increased from 0.92 in GO to 1.27 in rGO, as seen in Figure 6.2 b). This increased I_D/I_G ratio is explained as that the new graphitic domains are created in rGO with smaller size but in larger number compared to the one present in GO [27].

6.3.3 SEM images of rGO/$Bi_2O_2CO_3$

Small amount of rGO/$Bi_2O_2CO_3$ was dispersed in the absolute ethanol. After sonication for 10 mins, one drop of this dispersion was dropped onto a SEM sample holder. SEM images of

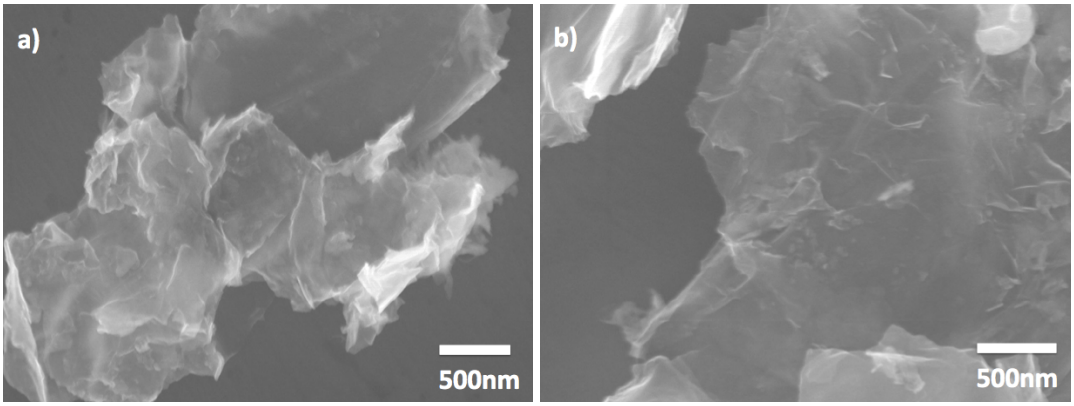

Figure 6.3: SEM images of rGO/$Bi_2O_2CO_3$ a) X30,000 b) X35,000 magnification

rGO/$Bi_2O_2CO_3$, with different magnifications of 30,000 and 35,000, were presented in Figure 6.3 a) and b). Flake materials with winkles, which could be referred to reduced graphene oxide, were observed in both images. These reduced graphene oxide sheets have size larger than 2 μm. Previous studies showed that $Bi_2O_2CO_3$ can exist as nanoparticles or nanosheets [30–32]. However, no $Bi_2O_2CO_3$ particles or flake were observed in Figure 6.3. To further determine the existence of bismuth component, EDS (energy dispersive X-ray spectroscopy) was used to test the chemical elemental composition of this composite material.

Figure 6.4 a) is a typical SEM image of rGO/$Bi_2O_2CO_3$. This composite material shows a lay-

Figure 6.4: EDS spectra of rGO/$Bi_2O_2CO_3$ composite material a) a typical SEM image b) carbon element in this area c) bismuth element in this area.

ered flake shape structure, as in Figure 6.4 a). Figure 6.4 b) and c) are the EDS results of carbon and bismuth element on this area. From these EDS results, both carbon and bismuth have strong signal in every place of this sample. Therefore, the existence of both reduced graphene oxide and bismuth composite can be proved.

6.3.4 TEM images of rGO/$Bi_2O_2CO_3$

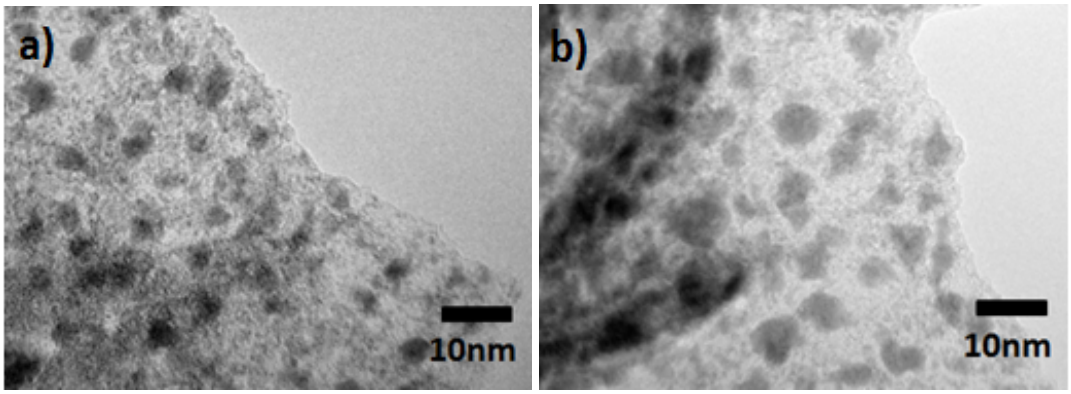

Figure 6.5: TEM images of a) rGO/$Bi_2O_2CO_3$ b) rGO/$Bi_2O_2CO_3$.

Figure 6.5 shows the detailed morphology of prepared rGO/$Bi_2O_2CO_3$ obtained by TEM. Bismuth subcarbonate particles, with size ∼5-10 nm, are dispersed on reduced graphene oxide sheets uniformly.

To further confirm the existence of $Bi_2O_2CO_3$ particles, selected area diffraction pattern (SAED) was used to analyse the selected area in Figure 6.6 a). The reflections shown in the SAED images, Figure 6.6 b), formed a ring shape which indicates that this material is a polycrystalline composite. The diffraction patterns correspond to the (002), (101), (103), (114) and (211) crystal planes of bismuth subcarbonate (Natl. Bur. Stand. (U.S.)). The lattice spacing in HRTEM images (Figure 6.6 c) and d)) were directly measured as 0.37 nm, which match the (101) crystal plane of tetragonal bismuth subcarbonate (Natl.Bur.Stand.(U.S.)).

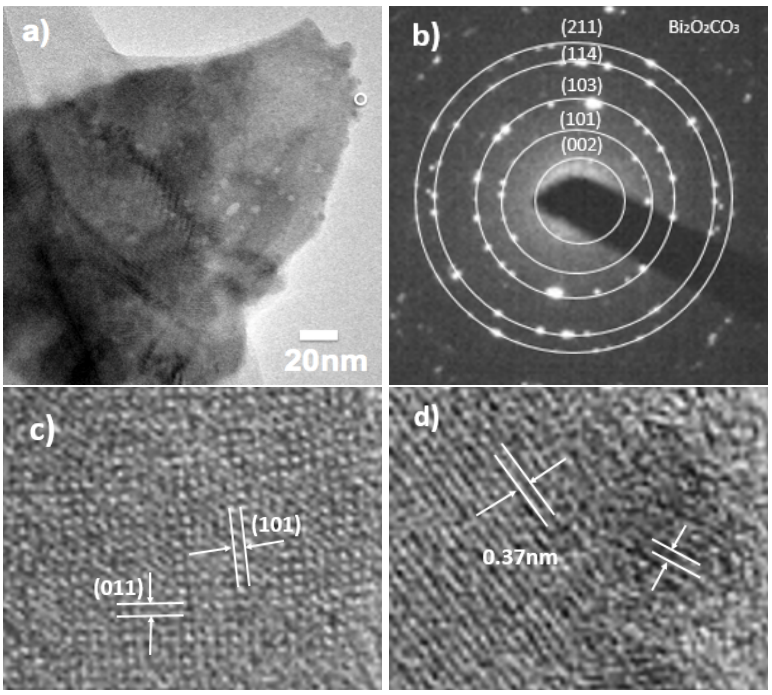

Figure 6.6: a) TEM image b) diffraction pattern c) HRTEM d) HRTEM of rGO/$Bi_2O_2CO_3$.

6.3.5 Electrochemical properties of rGO/$Bi_2O_2CO_3$ composite

Cyclic voltammetry is used to analyse the reactions that happen with rGO/$Bi_2O_2CO_3$ composite as electrode in the selected voltage range from -0.76 V to 0.24 V vs. SHE.

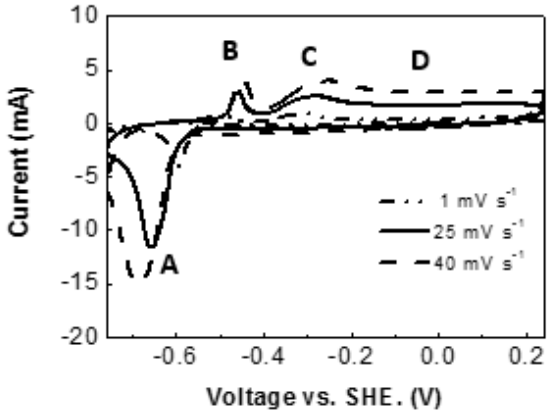

Figure 6.7: Cyclic voltammogram of rGO/$Bi_2O_2CO_3$ composite as electrode with different scanning rates.

Figure 6.7 shows that the cyclic voltammetry (CV) curves of rGO/ $Bi_2O_2CO_3$ composite with different scanning rate from 1 mV s^{-1} to 40 mV s^{-1} have similarshapes. A voltage range from -0.76 V to 0.24 V vs. SHE. is used. A reduction peak (A), appeared at -0.65 V, two oxidation peaks (B and C), appeared at -0.45 V and -0.3 V and a plateau (D) were observed in this cyclic voltammogram.

When the scanning rate is increased from 1 mV s^{-1} to 40 mV s^{-1}, the reduction peaks are shifted toward more negative values while the oxidation peaks shifted to a more positive values. This is due to the increase of the internal diffusion resistance as the scanning rate increases [33]. The reduction peak A that appeared at -0.6 to -0.7 V corresponds to the reduction reaction of bismuth ions from +3 oxidation state to 0 metal site [34]. The oxidation peak B and peak C are attributed to the formation of BiO_2^- and $Bi(OH)_3$ from $Bi^{(0)}$ [34]. The redox peaks caused by Faradaic reactions that appear in the cyclic voltammogram of rGO/$Bi_2O_2CO_3$ indicate that this composite exhibits a battery-like electrode performance [35] in the voltage range of -0.76 V to -0.2 V vs. SHE. This battery-like behaviour is contributed by the Faradaic reaction of $Bi_2O_2CO_3$. A plateau D appeared in the voltage range, -0.2 V to 0.24 V, vs. SHE has a rectangular shape which indicates the capacitor behaviour [35] of this composite. This plateau D is caused by the capacitive contribution of both rGO and the surface species of $Bi_2O_2CO_3$ [34]. Previous study proved that when the thickness of bismuth sample reduced, the plateau D shown a dominant feature in the CV results [34]. The reduction and oxidation reactions that happened during the cyclic voltammetry tests can be summarized as follow [34, 36]:

for peak A

$$Bi_2O_2CO_3 + 2OH^- \rightarrow 2BiO_2^- + H_2O \tag{6.1}$$

$$BiO_2^- + e^- \rightarrow BiO_2^{2-} \tag{6.2}$$

$$2H_2O + 3BiO_2^{2-} \leftrightarrow 2BiO_2^- + 4OH^- + Bi^{(0)} \tag{6.3}$$

$$Bi^{(0)} \rightarrow Bi_{(metal)} \tag{6.4}$$

for peaks B and C

$$Bi_{(metal)} \rightarrow Bi^+ + e^- \tag{6.5}$$

$$3Bi^+ \leftrightarrow Bi^{3+} + 2Bi_{(metal)} \tag{6.6}$$

$$3OH^- + Bi^{3+} \rightarrow Bi(OH)_3 \tag{6.7}$$

$$Bi(OH)_3 \rightarrow BiOOH + H_2O \tag{6.8}$$

$$BiOOH + OH^- \rightarrow BiO_2^- + H_2O \tag{6.9}$$

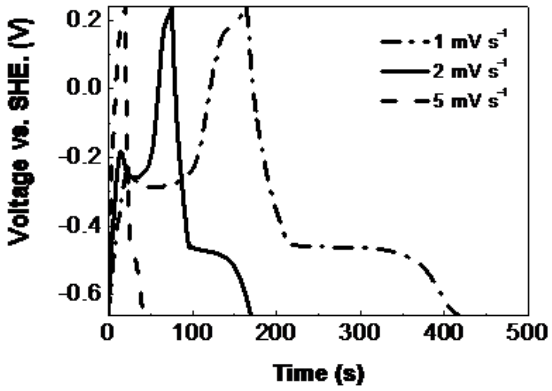

Figure 6.8: The charge/discharge behaviour of rGO/$Bi_2O_2CO_3$ composite under various current density.

The charge/discharge behaviours of rGO/$Bi_2O_2CO_3$ were studied under various current densities from 1 A g^{-1} to 5 A g^{-1}, as shown in Figure 6.8, in order to estimate the specific capacity of the rGO/$Bi_2O_2CO_3$ composite. In the charge/discharge curves, both the slope and plateau were observed. The plateau that appeared at the voltage of -0.5 V, -0.25 V and 0.2 V are contributed to the oxidation and reduction Faradaic reactions, in which $Bi_2O_2CO_3$ undergoes a phase transformation. The slope is resulted from the electric double layer capacitive of rGO. This charge/discharge curves show that rGO/$Bi_2O_2CO_3$ composite has a mix of both battery-like and capacitor-like electrochemical performance, which have good agreement with the CV results (Figure 6.7). Since the energy storage mechanism of rGO/$Bi_2O_2CO_3$ is non-capacitive or battery-like, specific capacity, as in the following equation, is suggested to be the appropriate way to estimate the electrochemical performance of this material [35, 37, 38]:

$$C_s = \frac{i \times \Delta t}{m} \tag{6.10}$$

where, C_s is the specific capacity (C g^{-1}), i is the current (mA), Δt is the discharging time (s) and m is the mass of active materials (mg).

The specific capacity value of of rGO/$Bi_2O_2CO_3$ at different current densities were calculated and listed in Figure 6.9. The specific capacity of rGO/$Bi_2O_2CO_3$ achieved 254 C g^{-1} at the current density of 1 A g^{-1}. When the current density has increased to 2 A g^{-1} and 5 A g^{-1}, the specific capacity has reduced to 170 C g^{-1} and 75 C g^{-1}, respectively.

Cycling performance of rGO/$Bi_2O_2CO_3$ was obtained by repeating the charge/discharge test for more than 4500 cycles. This nanocomposite material has excellent cycling performance under high current density of 3 A g^{-1}. Specific capacity has a sharp decreases from 128 C

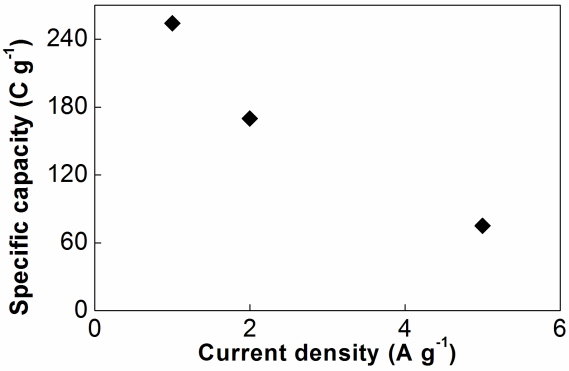

Figure 6.9: Specific capacity of rGO/$Bi_2O_2CO_3$ changes with current density increase.

g^{-1} to 85 C g^{-1} in the first 50 cycles and then the capacity value was kept at a stable value at $\sim$85 C g^{-1} for more than 4500 cycles (Figure 6.10 a)). To further study the changes of capacity at the first hundred cycles, specific capacity under the low current density of 1 A g^{-1} was also tested, as in Figure 6.10 b). With the low current density applied, this composite material has a more complete transition Faradaic reaction which provides high and accurate capacity value [39]. With current density of 1 A g^{-1} is used, the cycling performance has an obvious fluctuation in the first 20 cycles which might be due to the lose of adhesion between active material and Ni foam.

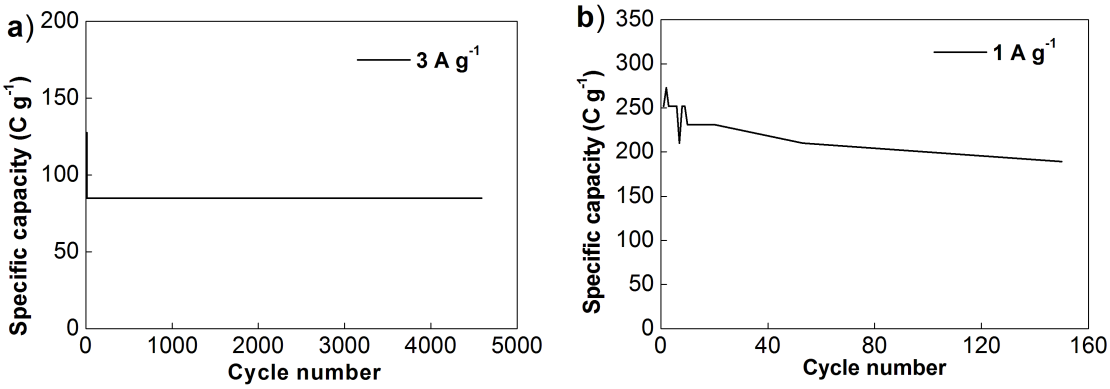

Figure 6.10: The cycling performance of rGO/$Bi_2O_2CO_3$ under the current density of a) 3 A g^{-1} and b) 1 A g^{-1}.

6.4 Conclusion

Nanocomposite material, rGO/$Bi_2O_2CO_3$, was synthesis through a novel one step method. This reaction only takes 3 hours at room temperature. In this synthesized composite material, $Bi_2O_2CO_3$ nanoparticles with size 5-10 nm have uniformly coated the surface of graphene

sheets. Due to the stability of nanostructure of composite material and special quantum size effect of bismuth, with only 6% of $Bi_2O_2CO_3$ loaded on graphene sheets, this nanocomposite material achieves 254 C g^{-1} at the current density of 1 A g^{-1} and outstanding cycling performance till more than 4500 cycles.

References

[1] P. Simon and Y. Gogotsi, "Materials for electrochemical capacitors," *Nature Materials*, vol. 7, pp. 845–845, 2008.

[2] A. K. Geim and K. S. Novoselov, "The rise of graphene," *Nature Materials*, vol. 6, pp. 183–191, 2007.

[3] K. S. Novoselov, A. K. Geim, S. V. Morozov, D. Jiang, Y. Zhang, S. V. Dubonos, I. V. Grigorieva, and A. A. Firsov, "Electric field effect in automically thin carbon films," *Science*, vol. 306, pp. 666–669, 2004.

[4] J. C. Meyer, A. K. Geim, M. L. Katsnelson, K. S. Novoselov, T. J. Booth, and S. Roth, "The structure of suspended graphene sheets," *Nature*, vol. 446, pp. 60–63, 2007.

[5] B. Fang and L. Binder, "A novel carbon electrode material for highly improved edlc performance," *The Journal of Physical Chemistry B*, vol. 110, p. 7877–7882, 2006.

[6] B. E. Conway, *Electrochemical supercapacitors: Scientific fundamentals and technological applications*. New York: Kluwer Academic/Plenum Publisher, 1999.

[7] Z. Wu, D. Wang, W. Ren, J. Zhao, G. Zhou, F. Li, and H. Cheng, "Anchoring hydrous RuO_2 on graphene sheets for high-performance electrochemical capacitors," *Advanced Functional Materials*, vol. 20, pp. 3595–3602, 2010.

[8] Z. Yu, B. Duong, D. Abbitt, and J. Thomas, "Highly ordered MnO_2 nanopillars for enhanced supercapacitor performance," *Advanced Materials*, vol. 25, pp. 3302–3306, 2013.

[9] Q. Cheng, J. Tang, J. Ma, H. Zhang, N. Shinya, and L. Qin, "Graphene and nanostructured MnO_2 composite electrodes for supercapacitors," *Carbon*, vol. 49, pp. 2917–2925, 2011.

[10] C. Chen, C. Chen, P. Huang, F. Duan, S. Zhao, P. Li, J. Fan, W. Song, and Y. Qin, "Nio/nanoporous graphene composites with excellent supercapacitive performance produced by atomic layer deposition," *Nanotechnology*, vol. 25, p. 504001, 2014.

[11] Y. Qiao, Q. Sun, H. Cui, D. Wang, F. Yang, and X. Wang, " Synthesis of micro/nano-structured Mn_3O_4 for supercapacitor electrode with excellent rate performance," *RSC Advances*, vol. 5, pp. 31 942–31 946, 2015.

[12] Y. Lee, S. Park, J. Seo, J. Yoon, J. Yi, and I. Song, "Nano-sized metal-doped carbon aerogel for pseudo-capacitive supercapacitor," *Current Applied Physics*, vol. 11, pp. 631–635, 2011.

[13] H. Jiang, T. Zhao, C. Yan, J. Ma, and C. Li, "Hydrothermal synthesis of novel Mn_3O_4 nano-octahedrons with enhanced supercapacitors performances," *Nanoscale*, vol. 2, pp. 2195–2198, 2010.

[14] H. Wang, Z. Hu, Y. Chang, Y. Chen, Z. Lei, Z. Zhang, and Y. Yang, "Facile solvothermal synthesis of a graphene nanosheet–bismuth oxide composite and its electrochemical characteristics," *Electrochimica Acta*, vol. 55, pp. 8974–8980, 2010.

[15] N. M. Leonard, L. C. Wieland, and R. S. Mohan, "Applications of bismuth(III) compounds in organic synthesis," *Tetrahedron*, vol. 58, pp. 8373–8397, 2002.

[16] W. S. Hummers and R. E. Offman, "Preparation of graphite oxide," *Journal of American Chemistry Society*, vol. 80, pp. 1339–1339, 1958.

[17] S. Park, J. An, J. R. Potts, A. Velamakanni, S. Murali, and R. S. Ruoff, "Hydrazine-reduction of graphite- and graphene oxide," *Carbon*, vol. 49, pp. 3019–3023, 2011.

[18] Y. Si and E. T. Samulski, "Synthesis of water soluble graphene," *Nano Letters*, vol. 8, pp. 1679–1682, 2008.

[19] E. Y. Choi, T. H. Han, J. Hong, J. E. Kim, S. H. Lee, H. W. Kim, and S. O. Kim, "Non-covalent functionalization of graphene with end-functional polymers," *Journal of Materials Chemistry*, vol. 20, pp. 1907–1912, 2010.

[20] H. Guo, X-F. Wang, Q-Y. Qian, F-B. Wang, and X-H. Xia, "A green approach to the synthesis of graphene nanosheets," *ACS Nano*, vol. 9, pp. 2653–2659, 2009.

[21] H. Doweidar and Y. B. Saddeek, "FTIR and ultrasonic investigations on modified bismuth borate glasses," *Journal of Non-Crystalline Solids*, vol. 355, pp. 348–354, 2009.

[22] I. Ardelean, S. Cora, R. Ciceo Lucacel, and O. Hulpus, "EPR and FT-IR spectroscopic studies of $B_2O_3Bi_2O_3MnO$ glasses," *Solid State Sciences*, vol. 7, pp. 1438–1442, 2005.

[23] R. Punia, R. S. Kundu, J. Hooda, S. Dhankhar, S. Dahiya, and N. Kishore, "Effect of

Bi_2O_3 on structural, optical, and other physical properties of semiconducting zinc vanadate glasses," *Journal of Applied Physics*, vol. 110, pp. 033 527(1–6), 2011.

[24] H. Huang, N. Tian, S. Jin, Y. Zhang, and S. Wang, "Syntheses, characterization and nonlinear optical properties of a bismuth subcarbonate $Bi_2O_2CO_3$," *Solid State Sciences*, vol. 30, pp. 1–5, 2014.

[25] X. Tu, S. Luo, G. Chen, and J. Li, "One-pot synthesis, characterization, and enhanced photocatalytic activity of a biobr-graphene composite," *Chemistry,*, vol. 18, pp. 14 359–14 366, 2012.

[26] Y. B. Saddeek, G. Y. Mohamed, H. S. Shokry Hassan, A. M. A. Mostafa, and G. Abdelfadeel, "Effect of gamma irradiation on the ftir of cement kiln dust–bismuth borate glasses," *Journal of Non-Crystalline Solids*, vol. 419, pp. 110–117, 2015.

[27] S. Stankovich, D. A. Dikin, R. D. Piner, K. A. Kohlhaas, A. Kleinhammes, Y. Jia, Y. Wu, S. T. Nguyen, and R. S. Ruoff, "Synthesis of graphene-based nanosheets via chemical reduction of exfoliated graphite oxide," *Carbon*, vol. 45, pp. 1558–1565, 2007.

[28] K. Krishnamoorthy, M. Veerapandian, K. Yun, and S. J. Kim, "The chemical and structural analysis of graphene oxide with different degrees of oxidation," *Carbon*, vol. 53, pp. 38–49, 2013.

[29] A. C. Ferrari, " Raman spectroscopy of graphene and graphite: Disorder, electron–phonon coupling, doping and nonadiabatic effects," *Solid State Communications*, vol. 143, pp. 47–57, 2007.

[30] N. Tian, H. Huang, Y. Zhang, and Y. He, " Enhanced photocatalytic activities on $Bi_2O_2CO_3/ZnWO_4$ nanocomposites," *Journal of Materials Research*, vol. 29, pp. 641–648, 2014.

[31] P. Madhusudan, J. Yu, W. Wang, B. Cheng, and G. Liu, "Facile synthesis of novel hierarchical graphene-$Bi_2O_2CO_3$ composites with enhanced photocatalytic performance under visible light," *Dalton Trans*, vol. 41, pp. 14 345–14 353, 2012.

[32] W. Wang, H. Cheng, B. Huang, X. Lin, X. Qin, X. Zhang, and Y. Dai, "Synthesis of $Bi_2O_2CO_3/Bi_2S_3$ hierarchical microspheres with heterojunctions and their enhanced visible light-driven photocatalytic degradation of dye pollutants," *Journal of Colloid and Interface Science*, vol. 402, pp. 34–39, 2013.

[33] J. Ji, L. Zhang, H. Ji, Y. Li, X. Zhao, X. Bai, X. Fan, F. Zhang, and R. S. Ruoff,

"Nanoporous $Ni(OH)_2$ thin film on 3D ultrathin graphite foam for asymmetric supercapacitor," *ACS Nano*, vol. 7, pp. 6237–6243, 2013.

[34] J. Ismail, M. F. Ahmed, and P. V. Kamath, "Cyclic voltammetry studies of electrodeposited thin films of bismuth in 1M KOH," *Journal of Electroanalytical Chemistry*, vol. 354, pp. 51–58, 1993.

[35] T. Brousse, D. Belanger, and J. W. Long, "To be or not to be pseudocapacitive?" *Journal of Electrochemistry Society*, vol. 162, pp. 5185–5189, 2015.

[36] V. Vivier, A. Regis, G. Sagon, J. Y. Nedelec, L. T. Yu, and C. Cachet-Vivier, "Cyclic voltammetry study of bismuth oxide Bi_2O_3 powder by means of a cavity microelectrode coupled with Raman microspectrometry," *Electrochimica Acta*, vol. 46, pp. 907–914, 2001.

[37] N. Padmanathan, H. Shao, D. McNulty, C. O'Dwyer, and K. M. Razeeb, "Hierarchical NiO–In_2O_3microflower (3D)/ nanorod (1D) hetero-architecture as a supercapattery electrode with excellent cyclic stability," *Journal of Materials Chemistry A*, vol. 4, pp. 4820–4830, 2016.

[38] H. Chen, S. Chen, Y. Zhu, C. Li, M. Fan, D. Chen, G. Tian, and K. Shu, "Synergistic effect of Ni and Co ions on molybdates for superior electrochemical performance," *Electrochimica Acta*, vol. 190, pp. 57–63, 2016.

[39] T. P. Gujar, V. R. Shinde, C. D. Lokhande, and S. H. Han, "Electrosynthesis of Bi_2O_3 thin films and their use in electrochemical supercapacitors," *Journal of Power Sources*, vol. 161, pp. 1479–1485, 2006.

Chapter 7

Enhanced removal of Nickel (II) ions from aqueous solutions by SDS-functionalized graphene oxide

7.1 Introduction

Heavy metal pollution in the aquatic environment is a serious environmental problem. In recent years, several methods for the treatment of waste water contaminated with heavy metals have been extensively studied and adsorption is now recognized as an effective and economic approach. The adsorption process offers flexibility in design and operation of treatment processes as well as producing high-quality treated effluent in many cases [1–4]. Adsorbents which have large surface area, pore volume and proper functionalities can be expected to perform most effectively and, for this reason, graphene oxide (GO) and graphene nanosheets have attracted tremendous interest. GO is functionalized graphene with various chemically bound oxygen-containing groups and is a potential adsorbent for metal (especially cationic metal) ion complexion through both electrostatic and coordination approaches, due to reactive functional groups on GO surface [5].

In the literature there are a number of examples of the modification of GO with organics or metal oxides for the removal of metal ions from water [5–10]. Madadrang et al. studied the modification of GO with EDTA (ethylenediamine triacetic acid) the resulting material displaying increased adsorption capacity for Pb (II) in comparison to GO [11]. Ren et al. used a graphene/δ-MnO_2 composite for the removal of Ni (II) ions from wastewater and obtained

higher adsorption capacity with respect to graphene or MnO_2 itself [12]. Graphene/δ-MnO_2 was prepared under 80-90°C which is energy and equipment demanding method. Zawisza et al. used GO as a solid sorbent for the preconcentration of cobalt, nickel, copper, zinc and lead [13]. The procedure in that study was based on dispersive micro-solid phase extraction and showed the great potential of GO as an excellent sorbent for preconcentration [13]. Gaboardi et al. synthesized Ni decorated graphene which showed increased hydrogen adsorption capacity compared to other common carbon based materials [14]. Ding et al. synthesized a reduced graphene oxide (rGO) supported chiral-modified Ni catalyst which they successfully employed for asymmetric hydrogenation [15].

Nickel (Ni) is the 24th most abundant element in the Earth's crust and is used in many industrial and commercial applications including electroplating, battery manufacture, forging, metal finishing and mining; all of which lead to environmental pollution by Ni. Exposure to highly Ni polluted environments has the potential to produce various pathological effects in humans, such as contact dermatitis, lung fibrosis, cardiovascular and kidney diseases and cancer [16–19]. Nickel is also an excellent catalyst for carbon dioxide reforming of methane and methane autothermal reforming with CO_2+O_2 in a fluidized-bed reactor [20,21] for production of synthesis gas (CO and H_2), which is the key step in the conversion of natural gas to liquid fuels and chemicals. Ferdowsi et al. reported Ni nanoparticle modified graphite electrode for the electro-catalytic oxidation of methanol [22].

The catalytic activity of nickel in the form of nickel nanoparticles (NiNPs) for the reversible hydration of carbon dioxide at room temperature and atmospheric pressure has been recently reported. This behaviour is potentially important for CO_2 capture technologies and for mineralisation processes [23, 24] and it has been confirmed that NiNPs are capable of accelerating mineral carbonation processes [23, 25]. Based on these results, technology to capture and mineralize CO_2 in the presence of nickel nanoparticles has been proposed. In order for this technology to become widely acceptable, it is very important to develop robust nickel adsorbers as precaution against environmental accidents (for example, after spillage dissolution of NiNPs into Ni (II) ions could occur under prolonged exposure to rainfall).

Therefore there is an urgent need to develop simple synthetic route and safe adsorber for removal of Ni(II) ions from water. Here we report an investigation into the use of GO for the removal of Ni (II) ions from aqueous solutions as a function of time, solute concentration, pH and adsorbent concentration. In addition a one pot and easy-to-handle method at room temperature without additional chemicals for the modification of graphene oxide surface using SDS

(sodium dodecyl sulphate) was developed, as it is expected to enhance Ni (II) ions removal based on previous study on the removal of drugs using bentonite in the presence of surface active agents by Çalışkan and Mahramanlıoğlu [26].

7.2 Experimental

Natural graphite flake (99.8%) and sulphuric acid (98%) were purchased from VWR. Analytical reagent grade phosphoric acid (85%), potassium permanganate (99.0%), hydrogen peroxide (35%), nickel (II) chloride (98%) and sodium dodecyl sulphate (SDS, 98.5%) were purchased from Sigma-Aldrich. All chemicals were used without further purification.

Graphene oxide (GO) was prepared by a modified Hummers method [27]. 3 g of graphite and 8 g of $KMnO_4$ were weighed and added into a mixture of 100 mL H_2SO_4 and 20 mL H_3PO_3. This suspension was kept at room temperature for three days with continuous stirring. H_2O_2 was added into this mixture until it turned a bright yellow colour. This mixture was washed and filtered using 5% HCl and followed by DI water (18 MΩ cm^{-1} resistivity) for several times until a pH of 7 was achieved. Graphene oxide was obtained after drying the deposit in an oven at 70°C overnight. Modified GO was prepared by stirring GO in a 1.2 g L^{-1} SDS dispersion for 24 hours at room temperature. This dispersion was then filtered and washed by DI water for several times to remove excess SDS. Modified GO (GO-SDS) was obtained after dried in oven at 70°C.

The adsorption experiments were carried out by stirring certain amount of GO or GO-SDS in a 25 mL Ni (II) ions solution for predetermined time at room temperature. After the materials were filtered, the concentration of Ni (II) ions in the solution were measured spectrophotometrically. The influence of pH on the Ni (II) ions adsorption was also studied by adding concentrated HCl or NaOH to adjust the pH value of the Ni (II) ions prepared solution. The Ni (II) ions concentration retained in the adsorbent phase was calculated by the following equation 7.1 [28]:

$$q = \frac{(C_0 - C)V}{W} \tag{7.1}$$

where, q is the adsorption capacity (mg g^{-1}), C_0 is the initial heavy metal ions concentration in solution (mg L^{-1}), C is the equilibrium concentration (mg L^{-1}), V is the volume of the solution used (L) and W is the mass of adsorbent used (g).

The kinetic parameters, such as the adsroption rate constant and the amount of Ni (II) ions

adsorbed at the equilibrium, of the adsorption were determined by fitting the adsorption data by the Lagergrene first order model and pseudo-second order model [29]. The rate limiting step in this adsorption procedure was determined from the intraparticle diffusion plots [30].

The Giles isotherms plots were obtained from the equilibrium absorption Ni (II) ions data. There equilibrium data were further analysed by Langmuir and the Freundlich isotherm models [31, 32]. The maximum Ni (II) ions adsorption at monolayer coverage in this experiment were then calculated from these isotherm models.

In this project, the controlled groups, with no adsorbent added, were measured for each set of the experiments. All the experiments were repeated three times under identical conditions and the results were found reproducible with an experimental error lower than 3%.

The concentrations of Ni (II) ions in solution were measured by Inductively coupled plasma optical emission spectroscopy (ICP-OES, UNICAM 701 series emission spectrometer) and UV-Visible spectrophotometer (Cary 100 UV-Vis) by applying the Dimethylglyoxime method [33]. The functional groups attached on the synthesised materials were tested by Fourier transform infrared (FTIR, Varian 800) spectroscopy. The zeta potential of both GO and GO-SDS were measured by zetasizer (Malvern, Nano ZS). The morphology of prepared materials were tested by scanning electron microscopy (SEM, XL30 ESEM-FEG) and transmission electron microscopy (TEM, Philips CM-100).

7.3 Results and discussion

7.3.1 Adsorption kinetics

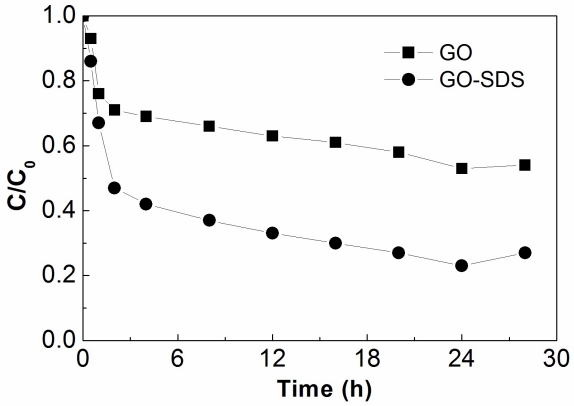

Figure 7.1: Effect of contact time of Ni (II) ions on GO and GO-SDS.

Figure 7.1 shows the effect of contact time of the Ni (II) ions adsorption on GO and GO-SDS. An initial Ni (II) ions concentration (C_0) of 40 mg L^{-1} was used. 25 mg of GO was used as the adsorbent. The Ni (II) ions concentrations (C) in the solution were tested after every few hours. For both GO and GO-SDS, the Ni (II) ions concentration in the solution has a fast decrease in the first few hours and then followed by a slowly but continually decrease. After 24 hours, the Ni (II) ions concentration in solution reached equilibrium for both GO and GO-SDS. At the equilibrium point, the Ni (II) ions concentration reduced to 53% of the initial value by using GO as adsorbate materials while by using GO-SDS the Ni (II) ions concentration reduced to 23% of the initial value which indicates that GO-SDS has stronger adsorption ability of Ni (II) ions.

Based on the Ni (II) ions concentration changed with the contact time, the adsorption rate constants of GO and GO-SDS on Ni (II) ions were calculated following the Lagergren first order equation 7.2 and pseudo-second order rate equation 7.3 [29]

$$ln(q_e - q) = lnq_e - k_1 t \tag{7.2}$$

$$\frac{t}{q} = \frac{1}{k_2 q^2} + \frac{1}{q_e} t \tag{7.3}$$

where, q is the amount of Ni (II) ions absorbed at the time t (mg g^{-1}), q_e is the amount of Ni (II) ions absorbed at the equilibrium (mg g^{-1}), k_1 is the adsorption rate constant of the Lagergren first order model and k_2 is the adsorption rate constant of the pseudo-second order model.

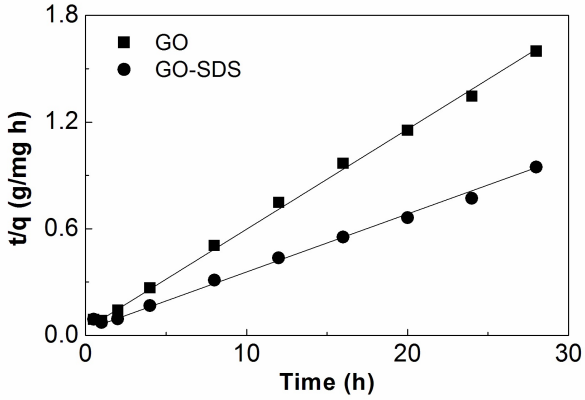

Figure 7.2: Ni ions adsorption by GO and GO-SDS fitted to the pseudo-second order model.

Adsorption of Ni (II) ions was fitted to the pseudo-second order model (Figure 7.2), which shows better agreement with experimental data than the Lagergren first order model (plot not shown), decided on the basis of the (R^2) correlation coefficient values, listed in Table 7.1.

It is important to determine the rate-limiting step of the adsorption mechanism, in which has

total three steps. The rate controlling mechanism can be one or any combination of the following:

(1) Mass transfer across the external boundary layer film of the liquid surrounding the outside of the adsorbant.

(2) Diffusion of the adsorbate molecules to an adsorption site either by a pore diffusion process through liquid filled pores or by a solid surface diffusion mechanism.

(3) Adsorption at a site on the surface (internal or external), the energy of which will depend on the binding process (physical or chemical); this step is assumed to be extremely rapid [30].

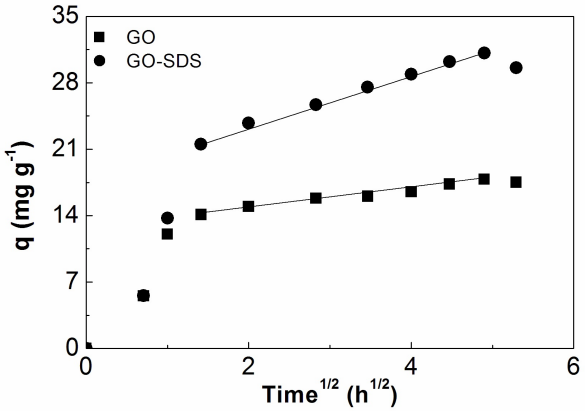

Figure 7.3: Intraparticle diffusion plots of GO and GO-SDS at different times.

Intraparticle diffusion plots (Figure 7.3) were used to analyse the mechanism of the adsorption in order to determine the rate-limiting step. To show the effect of intraparticle diffusion in the adsorption process, the amount of Ni (II) ions adsorbed (q) at any time was plotted against the square root of time ($t^{1/2}$) [34, 35]. There is an initial steep curve followed by a straight line, which indicates that two mechanisms are operating in the removal of Ni (II) ions with a plateau that indicates the equilibrium region. The initial curve can be explained by the boundary layer effect while the linear part corresponds to intraparticle diffusion. The linear portions of the curves do not pass through the origin, denoting that intraparticle diffusion is not the only rate controlling step for the adsorption of Ni (II) ions in this system [36]. The rate constants of intraparticle diffusion were obtained from the slopes of the straight lines of the second parts of the plots and are presented in Table 7.1.

The calculated adsorption rate constant and the amount of Ni (II) ions adsorbed in the equilibrium, based on both the Lagergren first order model and the pseudo-second order model, were listed in this table 7.1. Based on the correlation coefficient values R^2 in these two fits, pseudo-second order model shows better agreement with the experiment data in both the Ni

Table 7.1: Kinetic parameters of the Ni (II) ions adsorption on GO and GO-SDS.

	Lagergren 1 order model			Pseudo 2 order model			Intraparticle diffusion	
	k_1 (h^{-1})	q_1 (mg g^{-1})	R^2	k_2 (g mg^{-1} h^{-1})	q_2 (mg g^{-1})	R^2	k_d (mg $g^{-1/2}$ $h^{-1/2}$)	R^2
GO	0.1214	6.71	0.862	0.0597	18.08	0.998	0.99	0.977
GO-SDS	0.1425	18.00	0.942	0.0192	32.05	0.977	2.60	0.999

(II) ions adsorption on GO and GO-SDS. Based on this pseudo-second order model fitting, the adsorption of Ni (II) ions achieved an equilibrium value of 18.08 mg g^{-1} and 32.05 mg g^{-1} with GO and GO-SDS as the absorbant, respectively. In the intraparticle diffusion plot, both the curve and the linear parts were observed. The linear part of this plot was further fitted to a linear model, in which the rate constant (the slope of the line) was calculated and listed in the table 7.1. The correlation coefficient values R^2 in the linear parts of the intraparticle diffusion fitting indicates reliable rate constant results.

7.3.2 Equilibrium isotherm models

Giles developed the adsorption isotherm classification for solutes in dilute solution, which relates the shape of the plots to the parameters of the solvent adsorption [37]. According to the Giles isotherm classification, the shapes of the Giles isotherms for GO and GO-SDS (Figure 7.4) shows “L-type (Sub-group 2)” and “H-type (Sub-group 2)” behaviour respectively. L type behaviour is characteristic of systems where the adsorbate presents high affinity towards the adsorbent, and therefore indicates that no strong competition of the solvent with adsorbate takes place for the active sites of adsorption. H type is a special case of the L curve, in which the adsorbate has such high affinity to the adsorbent [38, 39].

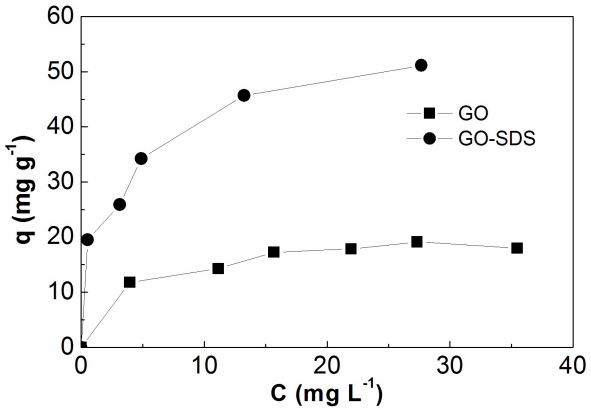

Figure 7.4: Giles isotherms of the adsorption of Ni (II) ions on GO and GO-SDS.

Equilibrium data were analysed by using the Langmuir [31] and the Freundlich [32] isotherm

models. Linear forms of the Langmuir and the Freundlich isotherm equations are presented in equation 7.4 and equation 7.5, respectively:

$$\frac{C_e}{q_e} = \frac{1}{Qb} + \frac{C_e}{Q} \tag{7.4}$$

$$lnq_e = lnk + nlnC_e \tag{7.5}$$

where, C_e is the finial concentration at equilibrium (mg L^{-1}), q_e is the amount of adsorbate adsrobed per unit mass of adsorbent at equilibrium (mg g^{-1}), Q is the maximum adsorption at monolayer coverage (mg L^{-1}), b is the adsorption equilibrium constant related to the energy of adsorption in (L mg^{-1}), k and n are the Freundlich constants representing the adsorption capacity and the intensity, respectively. The constants associated with the equations were determined and shown in Table 7.2.

Table 7.2: Adsorption isotherm parameters for the adsorption of Ni (II) ions on GO and GO-SDS [31, 32].

	Langmuir model			Freundlich model		
	Q (mg g^{-1})	b (L g^{-1})	R^2	n	k	R^2
GO	20.19	0.32	0.990	0.22	8.76	0.911
GO-SDS	55.16	0.40	0.992	0.26	22.03	0.960

The Langmuir model (as in Figure 7.5) gave a better fit than the Freundlich model for this process on the basis of the correlation coefficient (R^2) value, as in Table 7.2. From the Langmuir model, the maximum Ni (II) ions adsorption at the GO monolayer coverage achieved 20.19 mg g^{-1}. After decorated GO with SDS, this number reached 55.16 mg g^{-1}.

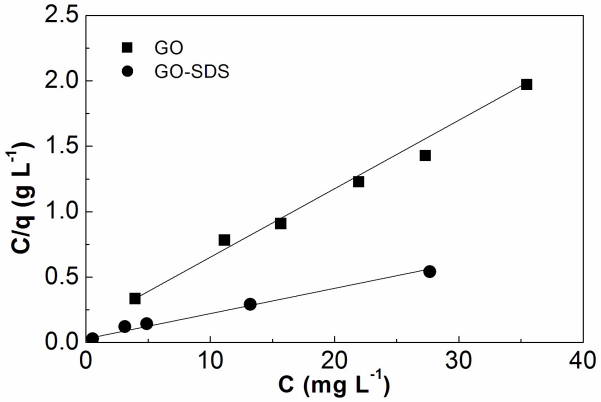

Figure 7.5: The Langmuir model fitted of Ni (II) ions adsorption on GO and GO-SDS.

7.3.3 Study the effect of pH on Ni(II) ions removal

The pH of the solution is one of the most important factors affecting the adsorption of metal ions. This is partly because hydrogen ions themselves are strongly competing with metal ions. In all solutions, there have been competitive adsorption among hydronium ions (H_3O^+) and metal ions. At low pH values, hydronium ions are adsorbed more than other ions, since hydronium ions have high concentration and more tendencies to be adsorbed. With an increasing pH value, hydronium ions concentration is reduced and results in other ions being better and more adsorbed [40, 41].

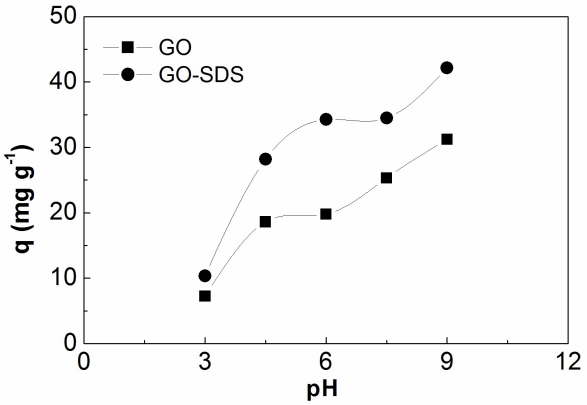

Figure 7.6: The adsorption capacities of GO and GO-SDS on Ni(II) ions changes with pH value of the solution.

Ni can be presented in the forms of Ni (II) ions (i.e., Ni^{2+}, $Ni(OH)^+$, $Ni(OH)_2^0$, $Ni(OH)_3^-$) and $Ni(OH)_4^2$ in the medium depends on the pH of the solution [42]. The effect of solution pH on the adsorption was studied at several pH values between 3 and 9, where the dominant specie for nickel is the Ni^{2+} cation. Adsorption capacities of both the GO and GO-SDS at different pH value Ni (II) ions solution were shown in Figure 7.6. With the pH value of Ni (II) ions solution increased from 3 to 9, the adsorption capacities of GO and GO-SDS were increased significantly from 7.23 mg g^{-1} to 31.24 mg g^{-1} and from 10.36 mg g^{-1} to 42.14 mg g^{-1}, respectively.

7.3.4 Study of the mechanism of Ni (II) ions adsorption

Ni (II) ions adsorption on a carbon adsorent may occur due to several mechanisms such as physical adsorption, chemical adsorption, ion exchange or a combination of these. In order to further understand the adsorption mechanism of Ni (II) ions, zeta potentials of the adsorbents at several pH value (between 3 and 9) were measured and are shown in Figure 7.7. Zeta po-

tentials of GO and GO-SDS have negative values at all pH value studied, which confirms that the surface charge is negative [43]; and mainly decreases from pH 3 to 9. The negative zeta potential even in acidic conditions indicates that GO and GO-SDS forms stable colloids due to electrostatic repulsion of the ionized functional groups [44].

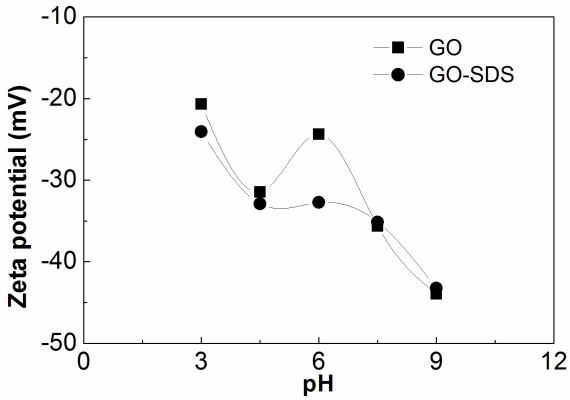

Figure 7.7: Zeta potential of GO and GO-SDS changes at different pH value.

Zeta potential is a physical parameter, used to quantify the adsorbent surface charge. By measuring the zeta potential as a function of pH, the acidity or basicity of the adsorbent surfaces can be determined. The zeta potentials of GO-SDS were more negative compared to those of GO and were all the negative values within the pH range tested herein. This is probably due to the presence of negative functional groups introduced by the SDS modifications. Numerous investigations have also demonstrated that the zeta potentials of modified adsorbents are more negative values than those of as produced ones and it also depends on the type of treatment for modification [45–48].

The tendency of the zeta potential is in accord with the increase in adsorption capacities at higher pH values. The effect of pH on adsorption and on zeta potentials of the adsrobents show that the driving force of the Ni (II) ions adsorption on GO and GO-SDS surface is electrostatic attraction between a negatively charged adsorbent surface and positively charged Ni (II) ions. The more negative zeta potential values of GO-SDS than that of GO also explains the better adsorption capacities found for GO-SDS.

Figure 7.8 show FTIR spectra obtained form GO and GO-SDS before and after the uptake of Ni (II) ions. The broad adsorption band in between 3000-3500 cm^{-1} can be attributed to OH groups. Absorption bands at around 1650 cm^{-1} are due to carbonyl and carboxyl groups. Bands at around 950-1400 cm^{-1} are due to the C-O bonds from the hydroxyl or epoxy groups [49–51]. Sharp peaks at around 2800 cm^{-1} appeared in the spectra of GO-SDS (after the treatment of GO with SDS) which are associated with C-H stretching. A sharp peak at around

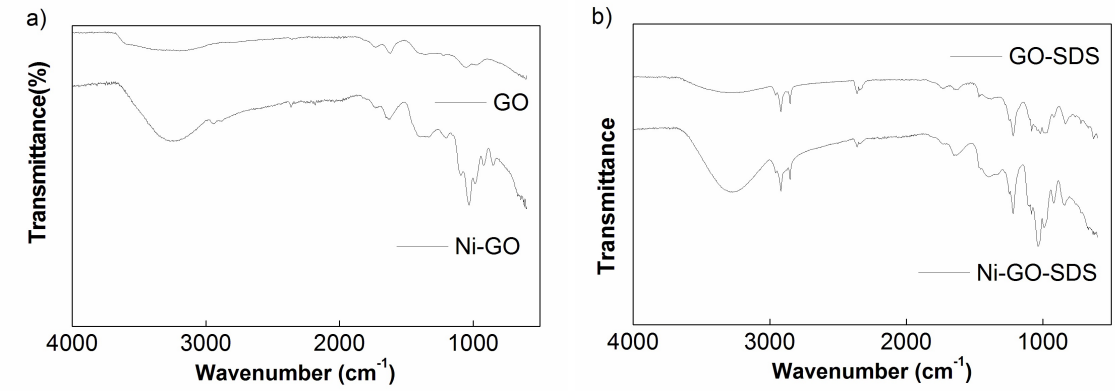

Figure 7.8: FTIR of a) GO and b) GO-SDS before and after Ni absorption.

1200 cm^{-1} also appeared in the spectra of GO-SDS which is due to the sulphate groups of SDS attached on GO. The peaks at around 950 cm^{-1} became sharp and changed shape in the spectra of GO-SDS, which could be attributed to the sulphate and hydroxyl groups from SDS [52]. After contacting with Ni, a new sharp peak at 1020 cm^{-1} was observed for both of the adsorbents GO and GO-SDS due to Ni (II) ions adsorption [53]. According to these FTIR spectra, SDS does not interact with the GO surface in a covalent manner when GO-SDS is formed.

Physicochemical modification methods had been most widely adopted, namely, covalent surface modification and non-covalent surface modification, depending on whether or not covalent bonding between the carbon structure and the functional groups and/or modifier molecules is involved in the surface modification process. The advantage of non-covalent functionalization is that it does not destroy the conjugation in the carbon structure. Non-covalent functionalization strategies do not have any effect on the physical properties of the adsorbent because they keep the structure of intrinsic sp^2 hybridized orbital unchanged. This can be done by taking advantage of the p–p interaction between conjugated molecules and the graphitic structure [54–56].

7.3.5 Morphology of the GO and GO-SDS

SEM images of GO and GO-SDS before and after Ni (II) ions adsorption are shown in Figure 7.9. The surfactant layer on GO which forms GO-SDS can be seen in Figure 9 d) and e) (as globules and strands, respectively). Chemisorption can occur by means of surface complexation of Ni (II) ions with carbonyl and/or carboxyl groups of the adsorbent surface. After GO and GO-SDS were used in Ni (II) ions solution, the Ni (II) ions concentration reduced and formed NiO with flower-like shape on the surface of GO and GO-SDS (Figure 7.9 c) and 7.9

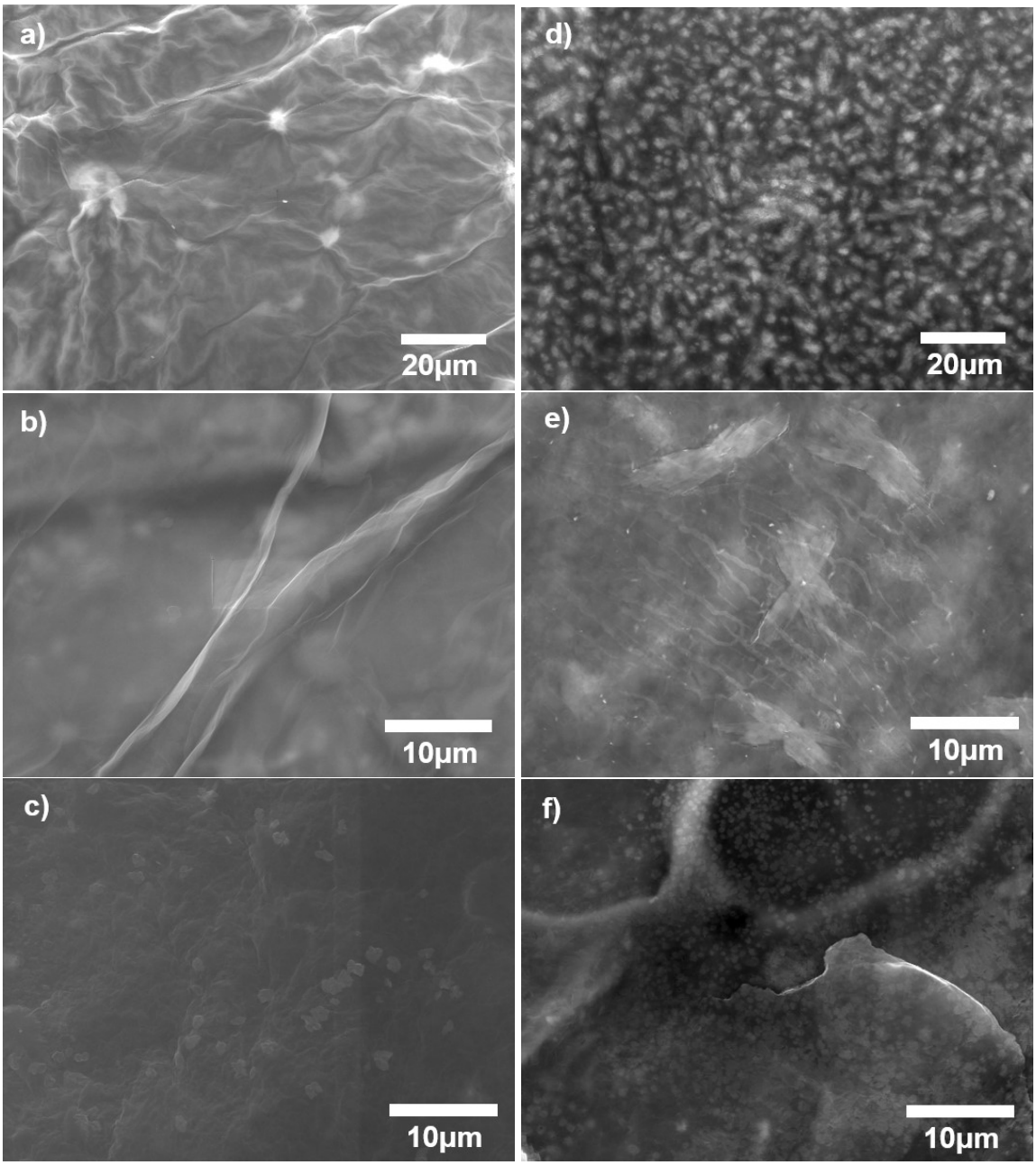

Figure 7.9: SEM images of a) GO X1,000 b) GO X2,500 c) GO-Ni X2,500 d) GO-SDS X1,000 e) GO-SDS X2,500 f) GO-SDS-Ni X2,500.

f)). Another possible mechanism for Ni (II) ions uptake is ion exchange (cation exchange), in which Ni (II) cations exchange with hydrogens of hydroxyl and/or carboxyl groups of the adsorbent surface.

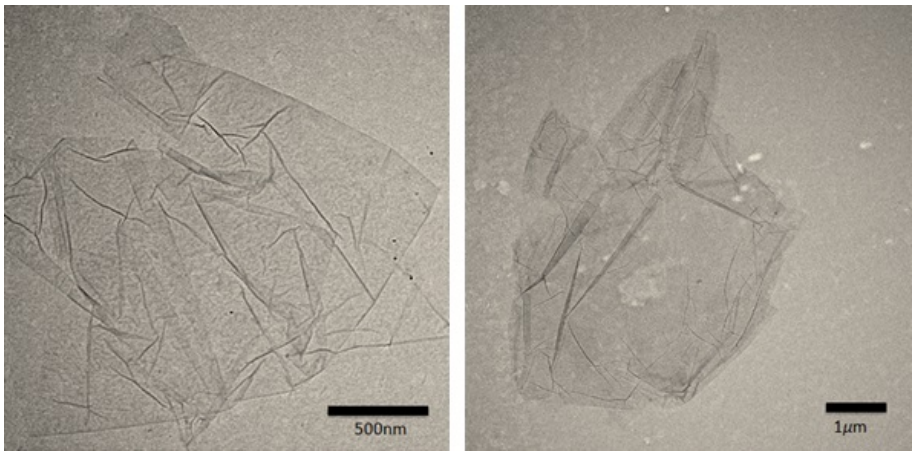

Figure 7.10: TEM images of GO.

GO has a thin layer structure, Dynamic light scanning (DLS), which does not give accurate results for non-spherical particles, is not suitable for GO size measurement. TEM images, as in Figure 7.10, were used to estimate the size of GO. From these images, GO have a size larger than 2 μm. SDS works as functional groups on GO, so it can be assumed that GO-SDS have similar size as GO.

7.3.6 Comparison of Ni adsorption

Figure 7.11 shows a brief comparison of the removal of Ni (II) ions by GO and GO-SDS at different loadings. By modified GO with SDS, the adsorption capacities of Ni (II) ions dramatically increased, although it does not change the time (24 hours) to reach equilibrium. In these comparison experiments, 40 mg L^{-1} of Ni (II) ions were used as the initial solution. The absroption experiment were carried out by using different amount of GO and GO-SDS as absorbant. With the amount of GO increased from 5 mg to 50 mg, the percentage of Ni(II) ions removal is increased from 10.5% to 71.9%. This increase in the percentage of Ni(II) ions removal with the increasing of absorbant was also observed with GO-SDS. With the same amount of absrobant used, GO-SDS shows better performance of Ni(II) ions removal than GO. When 50 mg of GO-SDS was used as the absorbant, the percentage of Ni(II) ions removal achieved 98.7%.

Beside the removal of heavy metal ions, adsorption technology is currently being applied extensively to the removal of organic and inorganic micro-pollutants from aqueous solutions and

carbon nanostructures with different morphologies are assumed to be one of the major elements in nanotechnology [57, 58]. GO is an effective adsorbent for the removal of Ni (II) ions from aqueous solutions and has the potential to be used for the treatment of waste or drinking water.

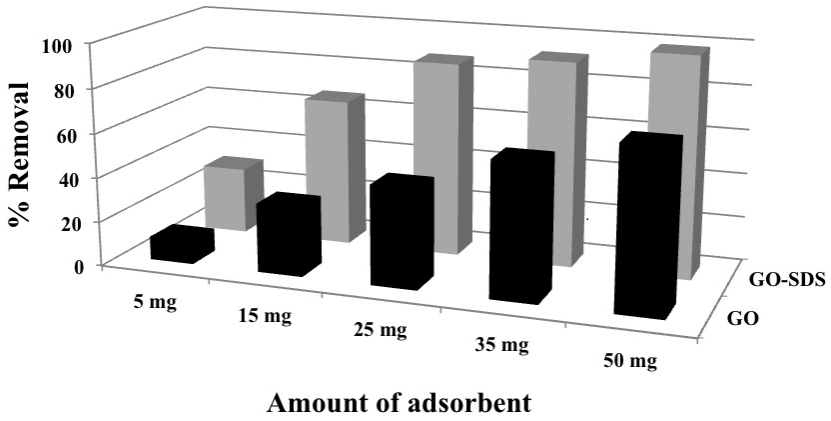

Figure 7.11: Comparison of % Ni (II) ions removal with different amounts of GO and GO-SDS.

Table 7.3: Comparison of various adsorbents for the removal of Ni (II) ions.

Adsorbent	Adsorate	mg g^{-1} (25°C)	Reference
Na-montmorillonite	Ni	3.63	[59]
multiwalled carbon nanotubes	Ni	6.89	[60]
γ-Fe_2O_3	Ni	23.60	[61]
DTPA-chitosan	Ni	24.16	[62]
EDTA-chitosan	Ni	24.35	[62]
vermiculite	Ni	25.33	[59]
nano-alumina	Ni	30.82	[63]
activated carbon	Ni	34.72	[64]
GO-G	Ni	36.63	[65]
graphene/δ-MnO_2	Ni	46.55	[12]
GO-SDS	Ni	55.16	this study

In the literature there are examples of the modification of graphene oxide with organics or metal oxides [9, 11–15] for the removal of metal ions from water. Results from experiments carried out at room temperature were listed in the table 7.3. Ren et al. have used Graphene/ δ-MnO_2 for the removal of Ni (II) ions from aqueous solutions and found the adsorption capacity as 46.55 mg g^{-1} [12] which is lower than we found in our study (55.16 mg g^{-1}). This graphene/δ-MnO_2 was prepared under 80-90°C which is an energy and equipment intensive method. Zhang and Wang [66] have studied the adsorption of Ni (II) ions between the tem-

peratures of 40°C and 75°C. The adsorption capacity at 25°C was not reported. Additionally, we can understand from Zhang and Wang's study that adsorption capacity of Ni (II) ions on lignocellulose/montmorillonite nanocomposite tends to increase with temperature. They have found the adsorption capacity around 67 mg g^{-1} at 40°C and around 95 mg g^{-1} at 70°C. Table 7.3 shows a comparison of various adsorbents from literature data for the adsorption of Ni (II) ions that are comparable to our study.

7.4 Conclusion

In this work an one pot and easy-to-handle method at room temperature without additional chemicals used for the modification of graphene oxide with surfactant is developed. Removal of Nickel (II) ions from aqueous solutions by GO and GO-SDS was studied spectrophotometrically at room temperature as a function of time, initial concentration and pH value. Adsorption capacity of the adsorbent was increased dramatically (from 20.19 mg g^{-1} to 55.16 mg g^{-1} found by Langmuir model) due to the functionalization of the surface by SDS. In this work we show that the removal of Ni (II) ions from aqueous solutions onto GO and GO-SDS are highly sensitive to pH changes. The driving force of the adsorption of Ni (II) ions is electrostatic attraction, Ni (II) ions adsorbed on the GO surface chemically and ion exchange.

References

[1] P. C. Nagajyoti, K. D. Lee, and T. V. M. Sreekanth, "Heavy metal, occurrence and toxicity for plants: a review," *Environmental Chemistry Letters*, vol. 8, pp. 199–216, 2010.

[2] A. Demirbas, "Heavy metal adsorption onto agro-based waste materials: a review," *Journal of Hazardous Materials*, vol. 157, pp. 220–229, 2008.

[3] F. Fu and Q. Wang, "Removal of heavy metal ions from wastewaters: a review," *Journal of Environmental Management*, vol. 92, pp. 407–418, 2011.

[4] M. Hua, S. Zhang, B. Pan, W. Zhang, L. Lv, Q. Zhang, "Heavy metal removal from water/wastewater by nanosized metal oxides: a review," *Journal of Hazardous Materials*, vol. 211-212, pp. 317–331, 2012.

[5] S. Wang, H. Sun, H. M. Ang, and M. O. Tade, "Adsorptive remediation of environmental pollutants using novel graphene-based nanomaterials," *Chemical Engineering Journal*,

vol. 226, pp. 336–347, 2013.

[6] S. Chowdhury and R. Balasubramanian, "Recent advances in the use of graphene-family nanoadsorbents for removal of toxic pollutants from wastewater," *Advanced in Colloid and Interface Science*, vol. 204, pp. 35–36, 2014.

[7] Y.-C. Lee and J.-W. Yang, "Self-assembled flower-like tio$_2$ on exfoliated graphite oxide for heavy metal removal," *Journal of Industrial and Engineering Chemistry*, vol. 18, pp. 1178–1185, 2012.

[8] M. Liu, C. Chen, J. Hu, X. Wu and X. Wang, "Synthesis of magnetite/graphene oxide composite and application for cobalt(II) removal," *The Journal of Physical Chemistry C*, vol. 115, pp. 25 234–25 234, 2011.

[9] N. Zhang, H. Qiu, Y. Si, W. Wang, and J. Gao, "Fabrication of highly porous biodegradable monoliths strengthened by graphene oxide and their adsorption of metal ions," *Carbon*, vol. 49, pp. 827–837, 2011.

[10] Y. He, N. Zhang, and X. Wang, "Adsorption of graphene oxide/chitosan porous materials for metal ions," *Chinese Chemical Letters*, vol. 22, pp. 859–862, 2011.

[11] C. J. Madadrang, H. Y. Kim, G. Gao, N. Wang, J. J. Zhu, H. Feng, M. Gorring, M. L. Kasner, and S. Hou, "Adsorption behavior of EDTA-graphene oxide for Pb(II) removal," *ACS Applied Materials & Interfaces*, vol. 4, pp. 1186–1193, 2012.

[12] Y. Ren, N. Yan, Q. Wen, Z. Fan, T. Wei, M. Zhang, and J. Ma, "Graphene/δ-MnO_2 composite as adsorbent for the removal of nickel ions from wastewater," *Chemical Engineering Journal*, vol. 175, pp. 1–7, 2011.

[13] B. Zawisza, R. Sitko, E. Malicka, and E. Talik, "Graphene oxide as a solid sorbent for the preconcentration of cobalt, nickel, copper, zinc and lead prior to determination by energy-dispersive X-ray fluorescence spectrometry," *Analytical Methods*, vol. 5, pp. 6425–6430, 2013.

[14] M. Gaboardi, A. Bliersbach, G. Bertoni, M. Aramini, G. Vlahopoulou, D. Pontiroli, P. Mauron, G. Magnani, G. Salviati, A. Züttel, and M. Riccò, "Decoration of graphene with nickel nanoparticles: study of the interaction with hydrogen," *Journal of Materials Chemistry A*, vol. 2, pp. 1039–1046, 2014.

[15] C. Ding, W. Wei, H. Sun, J. Ding, J. Ren, and X. Qu, "Reduced graphene oxide supported chiral ni particles as magnetically reusable and enantioselective catalyst for asym-

metric hydrogenation," *Carbon*, vol. 79, pp. 615–622, 2014.

[16] V. Coman, B. Robotin, and P. Ilea,, "Nickel recovery/removal from industrial wastes: A review," *Resources, Conservation and Recycling*, vol. 73, pp. 229–238, 2013.

[17] L. Huang, Y. Sun, T. Yang, and L. Li, "Adsorption behavior of Ni (II) on lotus stalks derived active carbon by phosphoric acid activation," *Desalination*, vol. 268, pp. 12–19, 2011.

[18] V. K. Gupta, C. K. Jain, L. Ali, M. Shama, and V. K. Sain, "Removal of cadmium and nickel from wastewater using bagsse fly ash——a sugar industry waste," *Water Research*, vol. 37, pp. 4038–4044, 2003.

[19] I. Villaescusa, N. Fiol, M. Martinez, N. Miralles, J. Poch, and J. Serarols, "Removal of copper and nickel ions from aqueous solutions by grape stalks wastes," *Water Research*, vol. 38, pp. 992–1002, 2004.

[20] S. He, Q. Jing, W. Yu, L. Mo, H. Lou, and X. Zheng, "Combination of CO_2 reforming and partial oxidation of methane to produce syngas over Ni/SiO_2 prepared with nickel citrate precursor," *Catalysis Today*, vol. 148, pp. 130–133, 2009.

[21] J. Guo, J. Gao, B. Chen, Z. Hou, J. Fei, H. Lou, and X. Zheng, "Catalytic conversion of CH_4 and CO_2 to synthesis gas on Ni/SiO_2 catalysts containing Gd_2O_3 promoter," *International Journal of Hydrogen Energy*, vol. 2009, pp. 8905–8911, 34.

[22] Gh. S. Ferdowsi, S. A. Seyedsadjadi, and A. Ghaffarinejad, "Ni nanoparticle modified graphite electrode for methanol electrocatalytic oxidation in alkaline media," *Journal of Nanostructure in Chemistry*, vol. 5, pp. 17–23, 2015.

[23] G. A. Bhaduri and L. Šiller, "Nickel nanoparticles catalyse reversible hydration of carbon dioxide for mineralization carbon capture and storage," *Catalysis Science & Technology*, vol. 3, pp. 1234–1239, 2013.

[24] G. A. Bhaduri, R. A. Henderson, and L. Šiller, "Reply to the 'Comment on "Nickel nanoparticles catalyse reversible hydration of carbon dioxide for mineralization carbon capture and storage" by D. Britt," *Catalysis Science & Technology*, vol. 3, pp. 2197–2198, 2013.

[25] M. Bodor, R. M. Santos, Y. W. Chiang, M. Vlad, and T. Van Gerven, "Impacts of nickel nanoparticles on mineral carbonation," *Scientific World Journal*, vol. 2014, pp. 1–10, 2014.

[26] E. S. Caliskan and M. Mahramanlioglu, "Equilibrium and kinetic adsorption of drugs on bentonite: presence of surface active agents effect," *Applied Clay Science*, vol. 101, pp. 381–389, 2014.

[27] W. S. Hummers and R. E. Offman, "Preparation of graphite oxide," *Journal of American Chemistry Society*, vol. 80, pp. 1339–1339, 1958.

[28] X. Guo, B. Du, Q. Wei, J. Yang, L. Hu, L. Yan, and W. Xu, "Synthesis of amino functionalized magnetic graphenes composite material and its application to remove Cr(VI), Pb(II), Hg(II), Cd(II) and Ni(II) from contaminated water," *Journal of Hazardous Materials*, vol. 278, pp. 211–220, 2014.

[29] D. Pletcher, R. Greff, R. Peat, L. M. Peter, and J. Robinson, *Instrumental Methods in Electrochemistry*. Woodhead Publishing, 2011.

[30] W. H. Cheung, Y. S. Szeto, and G. McKay, "Intraparticle diffusion processes during acid dye adsorption onto chitosan," *Bioresour Technology*, vol. 88, pp. 2897–2904, 2007.

[31] I. Langmuir, "The adsorption of gases on plane surfaces of glass, mica and platinum," *Journal of the American Chemical Society*, vol. 40, pp. 1361–1403, 1918.

[32] H. M. F. Freundlich, "Uber die adsorption in losungen," *Zeitschrift fur Physikalische Chemie*, vol. 57, pp. 385–470, 1906.

[33] N. Ortiz, M. A. F. Pires, and J. C. Bressiani, "Use of steel converter slag as nickel adsorber to wastewater treatment," *Waste Management*, vol. 21, pp. 631–635, 2001.

[34] M. Mahramanlioglu, I. Kizilcikli, and I. O. Bicer, "Adsorption of fluoride from aqueous solution by acid treated spent bleaching earth," *Journal of Fluorine Chemistry*, vol. 115, pp. 41–47, 2002.

[35] E. Çalışkan and S. Göktürk, "Adsorption characteristics of sulfamethoxazole and metronidazole on activated carbon," *Separation Science and Technology*, vol. 45, pp. 244–255, 2010.

[36] K. Rida, S. Bouraoui, and S. Hadnine, "Adsorption of methylene blue from aqueous solution by kaolin and zeolite," *Applied Clay Science*, vol. 83-84, pp. 99–105, 2013.

[37] C. H. Giles and D. Smith, "A general treatment and classificaton of the solute adsorption isotherm," *Journal of Colloid and Interface Science*, vol. 47, pp. 755–765, 1973.

[38] C. H. Giles, T. H. MacEwan, S. N. Nakhwa, and D. Smith, "Studies in adsorption. Part

XI. A system of classification of solution adsorption isotherms, and its use in diagnosis of adsorption mechanisms and in measurement of specific surface areas of solids," *Journal of Chemistry Society*, vol. 7896, pp. 3973–3993, 1960.

[39] A. S. Mestre, J. Pires, J. M. Nogueira, J. B. Parra, A. P. Carvalho, and C. O. Ania, "Waste-derived activated carbons for removal of ibuprofen from solution: role of surface chemistry and pore structure," *Bioresour Technology*, vol. 100, pp. 1720–1726, 2009.

[40] O. Moradi, M. Aghaie, K. Zare, M. Monajjemi, and H. Aghaie, "The study of adsorption characteristics Cu^{2+} and Pb^{2+} ions onto PHEMA and P(MMA-HEMA) surfaces from aqueous single solution," *Journal of Hazardous Materials*, vol. 170, pp. 673–679, 2009.

[41] O. Moradi, K. Zare, M. Monajjemi, M. Yari, and H. Aghaie, "The studies of equilibrium and thermodynamic adsorption of Pb (II), Cd(II) and Cu(II) ions from aqueous solution onto SWCNTs and SWCNT-COOH surfaces, fullerenes," *Nanotubes and Carbon Nanostructures*, vol. 18, p. 285, 2010.

[42] H. Liu, X. Wang, G. Zhai, J. Zhang, C. Zhang, N. Bao, and C. Cheng, "preparation of activated carbon from lotus stalks with the mixture of phosphoric acid and pentaerythritol impregnation and its application for Ni(II) sorption," *Chemical Engineering Journal*, vol. 209, pp. 155–162, 2012.

[43] W. Zhang, C. Zhou, W. Zhou, A. Lei, Q. Zhang, Q. Wan, and B. Zou, "Fast and considerable adsorption of methylene blue dye onto graphene oxide," *Bulletin of Environmental Contamination Toxicology*, vol. 87, pp. 86–90, 2011.

[44] G. K. Ramesha, A. V. Kumara, H. B. Muralidhara, and S. Sampath, "Graphene and graphene oxide as effective adsorbents toward anionic and cationic dyes," *Journal of Colloid Interface Science*, vol. 361, pp. 270–277, 2011.

[45] C.-H. Wu, "Studies of the equilibrium and thermodynamics of the adsorption of Cu^{2+} onto as produced and modified carbon nanotubes," *Journal of Colloid and Interface Science*, vol. 311, pp. 338–346, 2007.

[46] Y. Li, J. Ding, Z. Luan, Z. Di, Y. Zhu, C. Xu, D. Wu, and B. Wei,, "Competitive adsorption of Pb^{2+}, Cu^{2+} and Cd^{2+} ions from aqueous solutions by multiwalled carbon nanotubes," *Carbon*, vol. 41, pp. 2787–2792, 2003.

[47] Y. Li, S. Wang, Z. Luan, J. Ding, C. Xu, and D. Wu, "Adsorption of cadmium (II) from aqeous solution by surface oxidized carbon nanotubes," *Carbon*, vol. 41, pp. 1057–1062,

2003.

[48] C. Lu and H. Chiu, "Adsorption of zinc (II) from water with purified carbon nanotubes," *Chemical Engineering Science*, vol. 61, p. 1138, 2006.

[49] X. Sun, Z. Liu, K. Welsher, J. T. Robinson, A. Goodwin, S. Zaric, and H. Dai, "Nano graphene oxide for cellular imaging and drug delivery," *Nano research*, vol. 1, pp. 203–212, 2008.

[50] G. Wang, B. Wang, J. Park, J. Yang, X. Shen, and J. Yao, "Synthesis of enhanced hydrophilic and hydrophobic graphene oxide nanosheets by a solvothermal method," *Carbon*, vol. 47, pp. 68–72, 2009.

[51] H. Wang, Q. Hao, X. Yang, L. Lu, and X. Wang, "Graphene oxide doped polyaniline for supercapacitors," *Electrochemistry Communications*, vol. 11, pp. 1158–1161, 2009.

[52] C. M. Eggleston, S. Hug, W. Stumm, B. Sulzberger, and M. Dos Santos Afonso, "Surface complexation of surface by hematite surfaces: FTIR and STM observations," *Geochim Cosmochim. AC*, vol. 62, pp. 585–593, 1998.

[53] G. C. Panda, S. K. Das, T. S. Bandopadhyay, and A. K. Guha, "Adsorption of nickel on husk of Lathyrus sativus: behavior and binding mechanism," *Colloid Surface B*, vol. 57, pp. 135–142, 2007.

[54] O. Moradi, M. Yari, K. Zare, B. Mirza, and F. Najafi, "Carbon nanotubes: chemistry principles and reactions: review," *Nanotubes and Carbon Nanostructures*, vol. 20, p. 138, 2012.

[55] A. Ahmadpour, N. Eftekhari, and A. Ayati, "Performance of MWCNTs and a low cost adsorbent for chromiun (VI) ion removal," *Journal of Nanostructure in Chemistry*, vol. 4, pp. 171–178, 2014.

[56] K. Zare, V. K. Gupta, O. Moradi, A. S. H. Makhlou, M. Sillanpaa, M. N. Nadagouda, H. Sadegh, R. Shahryari-ghoshekandi, A. Pal, Z. Wang, I. Tyagi, and M. Kazemi, "A comparative study on the basis of adsorption capacity between CNTs and activated carbon as adsorbents for removal of noxious synthetic dyes: a review," *Journal of Nanostructure in Chemistry*, vol. 227-236, p. 5, 2015.

[57] S. Parlayici, V. Eskizeybek, A. Avci, and E. Pehlivan, "Removal of chromium (VI) using activated carbon supported functionalized carbon nanotubes," *Journal of Nanostructure in Chemistry*, vol. 5, pp. 225–263, 2015.

[58] M. Anbia and S. Khoshbooei, "Functionalized magnetic MCM-48 nanoporous silica by cyanuric chloride for removal of chlorophenol and bromophenol form aqueous media," *Journal of Nanostructure in Chemistry*, vol. 5, pp. 139–146, 2015.

[59] O. Abollino, A. Giacomino, M. Malandrino, and E. mentasti, "Interaction of metal ions with montmorillonite and vermiculite," *Applied Clay Science*, vol. 38, pp. 227–236, 2008.

[60] P. Liang, L. Yan, L. Guo, J. Zeng, and H. Lu, "Multiwalled carbon nanotubes as solid phase extraction adsorbent for the preconcentration of trace metal ions and their determination by inductively coupled plasma atomic emission spectrometry," *Journal of Analytical Atomic Spectrometry*, vol. 19, pp. 1489–1492, 2014.

[61] J. Hu, G. H. Chem, and L. M. C. Lo, "Selective removal of heavy metals from industrial waste water using maghemite nanoparticle: performance and mechanisms," *Journal of Environmental Engineering (ASCE)*, vol. 132, pp. 709–715, 2006.

[62] E. Repo, J. K. Warcholc, T. A. Kumiawana, and M. E. T. Sillanpaa, "Adsorption of Co (II) and Ni (II) by EDTA and /or DTPA modified chitosan: knietic and equilibrium modeling," *Chemical Engineering Journal*, vol. 161, pp. 73–82, 2010.

[63] V. Srivastava, C. H. Weng, V. K. Singh, and Y. C. Sharma, "Adsorption of nickel ions from aqueous soutions by nano alumina: kinetic, mass transfer, and equilibrium studies," *Journal of Chemical & Engineering Data*, vol. 56, pp. 1414–1422, 2011.

[64] Z. Gao, J. Fan, J. Zhang, Y. Kang, H. Liu, L. Jiang, and C. Zhang, "Sorption heavy metal ions by activated carbons with well developed microporosity and amino groups derived from phragmitesaustralis by ammoniumphosphates activation," *Journal of the Taiwan Institute of Chemcial Engineers*, vol. 58, pp. 290–296, 2016.

[65] F. Najafi, O. Moradi, M. Rajabi, M. Asif, I. Tyagi, S. Agarwal, and V. K. Gupta, "Thermodynamics of the adsorption of nickel ions from aqueous phase using graphene oxide and glycine functionalized graphene oxide," *Journal of Molecular Liquids*, vol. 208, pp. 106–113, 2015.

[66] X. Zhang and X. Wang, "Adsorption and desorption of nickel (II) ion sfrom aqueous solution by a lignocellulose/ montmorillonite nanocomposite," *PLoS ONE*, vol. 10, pp. 0 117 077(1–21), 2015.

Chapter 8

Conclusion and future work

8.1 Conclusion

In this work, reduced graphene oxide/bismuth (rGO/Bi), reduced graphene oxide/bismuth oxide (Bi_2O_3-rGO) and reduced graphene oxide/bismuth subcarbonate (rGO/$Bi_2O_2CO_3$) were synthesized at low temperature (60°C and room temperature) and short reaction time (3 hr). rGO/Bi was synthesized for the first time using a polyol process, in which hydrazine was used as the reducing agent while ethylene glycol was used as both the solvent and reducing agent. Metallic Bi particles with size of 20 to 50 nm were formed and attached to the reduced graphene oxide sheets. In this composite, rGO sheets act as impermeable atomic membranes to protect Bi particles from oxidation. This rGO/Bi composite reached a specific capacity of 773 C g^{-1} at the current density of 0.2 A g^{-1}. This material not only has good power density but also shows moderate stability in cycling tests with a current density as high as 5 A g^{-1}. A simple chemical reduction, without using any toxic chemicals, was used for Bi_2O_3-rGO synthesis. The fast, green but low energy requirement synthesis method is promising for large-scale production of this composite. This composite material exhibits a specific capacity as high as 559 C g^{-1} at the current density of 0.18 A g^{-1}. rGO/$Bi_2O_2CO_3$ was synthesized by using dimethyl sulfoxide as the solvent. $Bi_2O_2CO_3$ particles with size of 5 to 10 nm uniformly coated on the rGO surface. With only 6% of $Bi_2O_2CO_3$ used, this composite has a specific capacity value of 254 C g^{-1} and excellent cycling performance for more than 4000 cycles.

The following table summaries the synthesis and characterization of these three graphene bismuth composites in this thesis.

Table 8.1: Summaries of graphene bismuth composite materials.

	rGO/Bi	Bi_2O_3-GO	rGO/$Bi_2O_2CO_3$
initial materials	GO, $Bi(NO_3)_3$	GO, $Bi(NO_3)_3$	GO, $Bi(NO_3)_3$
rGO percentage (wt%)	56	10	94
solvent	NaOH, EG	NaOH	DMSO
reducing agents	N_2H_4, EG	none	N_2H_4
reaction temperature °C	60	60	25
reaction time h	3	3	3
stirring	yes	no	yes
structure	nanoparticles	flower like	nanoparticles
specific capacity C g^{-1}	773	559	254
cycling performance	800 cycles	1000 cycles	4500 cycles

These three composite materials were synthesised from the same initial materials, GO and $Bi(NO_3)_3$, by controlling the GO weight percentage and reducing agents. In the rGO/Bi composite, bismuth were successful reduced from the three oxidation state to metallic bismuth. This is because the using of N_2H_4 were added as the reducing agents. To reach the nano-sized bismuth particles, EG was added during the reaction to form an intermediate complex with the bismuth ions, which absorbs on the metallic bismuth surface and prevent them from aggregation. The EG was worked as both the solvent and reducing agent in the synthesis of rGO/Bi. In the synthesis of Bi_2O_3-GO, the oxidation state of bismuth did not change after the reaction because no reducing agents were involved in the synthesis procedure. In this sample, without using stirring in the reaction, Bi_2O_3 was grown and formed micro-sized flower like shape. In the rGO/$Bi_2O_2CO_3$ sample, DMSO was used as the solvent instead of NaOH while N_2H_4 was used as the reducing agent. During the reaction, only GO was reduced to rGO. DMSO worked as both the solvent and carbon sources for $Bi_2O_2CO_3$. The specific capacity and cycling performance of these three as-prepared samples were estimated from their charge/discharge behaviours. rGO/Bi has a specific value as high as 773 C g^{-1} at the current density of 0.2 A g^{-1}. After 800 cycles, 74.5% of its specific capacity was maintained. Bi_2O_3-GO achieves a specific capacity of 559 C g^{-1}. After 1000 cycles, Bi_2O_3-GO still keeps 57% of its initial specific capacity value. With only 6% of $Bi_2O_2CO_3$ added, rGO/$Bi_2O_2CO_3$ achieves a specific capacitance of 254 C g^{-1} at the current density of 0.18 A g^{-1}. This composite material has stable cycling performance till more than 4500 cycles.

The simple synthesis methods, low reaction temperature, short reaction times, relatively high abundance and low price of bismuth, good specific capacity value of these graphene bismuth composites make them as the promising candidates for the use as electrode materials in future electronic devices.

In addition, the Ni (II) ions adsorption capacity of graphene oxide (GO) was characterised. The driving force of the adsorption of Ni (II) ions are electrostatic attraction, Ni (II) ions adsrobed on the GO surface chemically and ion exchange. In this work, an one step easy-handle method at room temperature without any additional chemicals for the modification of graphene oxide with surfactant is developed. By modified GO with sodium dodecyl sulfate (SDS), the Ni (II) ions adsorption capacity was increased dramatically from 20.19 mg g^{-1} to 55.16 mg g^{-1}. Beside the analysis of Ni (II) ions adsorption mechanism, the pH values of the suspension was also been proved have large effect on their Ni (II) ions adsorption capacity.

8.2 Future work

For Bi_2O_3-rGO and rGO/$Bi_2O_2CO_3$, some more characterization can be done to further analyse these materials. TGA can be used to analyse the accurate graphene to bismuth compounds ratio for these two samples. To further explain the specific capacity decreases in cycling performance, SEM and TEM of the samples after the cycling test can be done to study the morphology changes. XPS, FTIR and Raman spectroscopy of the samples after cycling performance can be tested and used to analyse the chemical and functional groups change. In addition, reduced graphene oxide synthesized with the same method as for Bi_2O_3-rGO and rGO/$Bi_2O_2CO_3$ can be used as the controlled group to study how much the bismuth compounds contributed to the electrochemical properties of the composite materials. For all the graphene bismuth compounds (rGO/Bi, Bi_2O_3-rGO and rGO/$Bi_2O_2CO_3$), different graphene and bismuth compounds ratio can be used to synthesis the composite materials and study the optimum graphene bismuth compounds ratio for the electrochemical properties of these materials. The application of these graphene bismuth based composite materials in other fields can also been studied. Beside the energy storage devices, these composite materials could also been used as light emitters and gas sensors due to the good electronic properties. With the large surface area of graphene and good photo-catalyst properties of bismuth compounds, these nano-composite materials have the potential application in degradation of synthetic dyes in solutions.

In this project, only Ni(II) ions was studied in the wastewater treatment by GO-SDS. The absorption of other heavy metal ions by GO-SDS could also be analysed. In addition, the ability of removing organic pollution, such as pigments, dyes and lubricants, in solution should also be studied.

Publications

- **Jiabin Wang**, Han Zhang, Michael R. C. Hunt, Alasdair Charles, Jie Tang, Oana Bretcanu, David Walker, Khalil T. Hassan, Yige Sun and Lidija Šiller. Synthesis and characterisation of reduced graphene oxide/bismuth composite for electrodes in electrochemical energy storage devices, *ChemSusChem*, **10**, 2017, pp363-371

  http://dx.doi.org/10.1002/cssc.201601553

- **Jiabin Wang**, Elif Caliskan Salihi and Lidija Šiller. Green reduction of graphene oxide using alanine, *Materials Science and Engineering: C*, **72**, 2017, pp1-6

  http://dx.doi.org/10.1016/j.msec.2016.11.017

- Elif Caliskan Salihi, **Jiabin Wang**, Daniel J. L. Coleman and Lidija Šiller. Enhanced removal of nickel (II) ions from aqueous solutions by SDS-functionalized graphene oxide, *Separation Science and Technology*, **51**, 2016, pp1317-1327

  http://dx.doi.org/10.1080/01496395.2016.1162172

- Julia Maxi Kanold, **Jiabin Wang**, Franz Brummer and Lidija Šiller. Metallic nickel nanoparticles and their effect on the embryonic development of the sea urchin Paracentrotus lividus, *Environmental Pollution*, **212**, 2016, pp224-229

  http://dx.doi.org/10.1016/j.envpol.2016.01.050